# Resonant Drive Techniques for MEMS: A Comparative Study

by

Rana Abdelrahman

A thesis
presented to the University of Waterloo
in fulfillment of the
thesis requirement for the degree of
Master of Applied Science
in
Systems Design Engineering - Nanotechnology

Waterloo, Ontario, Canada, 2023

© Rana Abdelrahman 2023

## Author's Declaration

I hereby declare that I am the sole author of this thesis. This is a true copy of the thesis, inclding any required final revisions, as accepted by my examiners.

I understand that my thesis may be made electronically available to the public.

## Abstract

Electrostatic actuation is popular in microelectromechanical systems (MEMS) because of its many advantages. However, it requires high voltage, typically provided by a power supply and a high voltage amplifier, which is limited in gain particularly at high frequencies. As research interest has shifted to explore higher frequency MEMS, various methods have been proposed to amplify the voltage signal fed into the system by coupling it in series to an LC tank circuit constituted by introducing an external inductor $L$. These methods are based on utilizing the electrical quality factor $Q_e$ of an RLC circuit driven at its natural frequency $f_e$ to amplify the actuation voltage of the MEMS. In this thesis, we analyzed and compared among these three resonant drive techniques. We also compared their performance to a voltage amplifier.

The first resonant drive technique matches electrical and mechanical resonances and activates them simultaneously $f_e \approx f_m$ by tuning the external inductor $L$. The second technique drives the MEMS with a two-frequency signal. One frequency is set equal to the electric resonance $f_1 \approx f_e$ while the sum or difference of the two frequencies is set equal to the mechanical resonance $f_1 \pm f_2 \approx f_m$. In the third method, the microbeam is driven using an amplitude-modulated (AM) signal that contains an RF carrier frequency $f_c$ and a baseband frequency $f_b$. The LC circuit is tuned to match the carrier frequency to the electrical resonance $f_c \approx f_e$, and the baseband frequency is set equal to the mechanical resonance $f_b \approx f_m$.

We found that resonant circuits were more effective at amplifying the MEMS response than a voltage amplifier. This is due to amplifiers' limitations at high frequencies. Furthermore, we found that mixed frequency and amplitude modulation techniques are more flexible and easier to tune than resonance matching. However, resonance matching is more effective for unbiased (AC) excitation since it results in higher voltage amplification than the other two technique.

We also analyzed the circuit parasitics that undermine those actuation schemes. In particular,

parasitic capacitance is known to negatively impact the performance of MEMS devices by decreasing their signal-to-noise ratio and their cut-off frequency. While the former has long been a persistent challenge to MEMS sensors, the latter is becoming more of a challenge as interest has shifted to activation of higher mode and higher frequency MEMS. To improve the performance of MEMS, we have studied the origins of parasitic capacitance with a view to minimize them and found that leaving the substrate and surrounding devices floating can minimize the total parasitic capacitance.

**Acknowledgements**

All praise is due to Allah for granting me the opportunity and providing me with guidance and patience to undertake this research.

I would like to express my deepest gratitude to my supervisors, Prof. Eihab Abdel-Rahman and Prof. Mustafa Yavuz, for their invaluable guidance, support, and expertise.

Furthermore, I extend my heartfelt thanks to my family for their unwavering support and encouragement. I would also like to thank my colleagues and co-workers for their assistance, help, and support.

# Table of Contents

**List of Figures** ix

**List of Tables** xvi

**1 Introduction** 1

1.1 MEMS Sensors and Actuators . . . . . 1

1.2 Actuation Methods for MEMS . . . . . 2

1.2.1 Electrothermal Actuation . . . . . 3

1.2.2 Electromagnetic Actuation . . . . . 3

1.2.3 Piezoelectric Actuation . . . . . 4

1.2.4 Electrostatic Actuation . . . . . 4

1.3 Resonant Drive . . . . . 6

**2 Electrostatic MEMS Actuator** 8

2.1 Actuator Design . . . . . 8

2.2 Lumped-Element Model . . . . . 9

2.2.1 Mechanical Subsystem . . . . . 11
2.2.2 Electrical Subsystem . . . . . 14
2.2.3 Nondimensionalization . . . . . 15
2.2.4 Static Analysis . . . . . 17
2.2.5 Dynamic Analysis . . . . . 18

**3 Results** **21**

3.1 Characterization . . . . . 21
3.1.1 Experimental Setup . . . . . 22
3.1.2 Modal Analysis . . . . . 22
3.2 Conventional Excitation . . . . . 24
3.3 Resonant Drive . . . . . 28
3.3.1 Electrical Characterization . . . . . 28
3.3.2 Experimental Setup . . . . . 33
3.3.3 Resonance Matching . . . . . 33
3.3.4 Multi-Frequency Excitation . . . . . 41
3.3.5 Amplitude Modulation . . . . . 48
3.4 Model Validation . . . . . 54
3.5 Estimation of the Electrical Quality Factor . . . . . 61
3.5.1 Model Limitations . . . . . 74
3.6 Comparison Among the Actuation Techniques . . . . . 77

**4 Parasitics and Artifacts** **81**

4.1 Parastic Capacitance . . . . . 81

4.2 Other Parasitics . . . . . 87

4.3 Equipment Loading . . . . . 90

4.4 Transients . . . . . 92

**5 Conclusions and Future Work** **96**

5.1 Conclusions . . . . . 96

5.2 Future Work . . . . . 98

**Bibliography** **101**

# List of Figures


1.1 A typical electrostatic MEMS actuator. . . . . 5

1.2 A schematic showing the electrical resonance $f_e$ of an RLC circuit and the mechanical resonance $f_m$ of a MEMS actuator. . . . . 7

2.1 (a) A microscopic image, (b) a white light profilometer image, (c) an SEM image, and (d) a schematic of the actuator. . . . . 9

2.2 Out-of-plane bending mode. . . . . 10

2.3 Equivalent circuit of the electromechanical system. . . . . 11

2.4 Electrostatic field of the actuator at (a) equilibrium (b) out-of-plane motion. . . . 13

2.5 Constant amplification $V_{\mathrm{Cr}}$ vs. frequency dependent amplification $V_{\mathrm{C}}$. . . . . 20

3.1 The experimental setup for actuator characterization. . . . . 22

3.2 FFT of the measured tip displacement under a pulse excitation showing the first out-of-plane and in-plane bending modes of actuator I. . . . . 23

3.3 FFT of the measured tip displacement for actuator II under pulse excitation showing the response of (a) the first out-of-planeand (b) the first in-plane bending modes. 24

3.4 The frequency-response curves of actuator I beam tip displacement under four levels of the amplified voltage amplitude $V_{\mathrm{AC}}$. . . . . 25

3.5 The frequency-response curves of the beam tip displacement of actuator I′ under eleven levels of the amplified voltage amplitude $V_{\mathrm{AC}}$. . . . . 26

3.6 The frequency-response curves of actuator II beam tip displacement for eight levels of the amplified voltage amplitude $V_{\mathrm{AC}}$. . . . . 27

3.7 The frequency-response curves of actuator II beam tip displacement under two levels of the voltage amplitude $V_{\mathrm{AC}}$. . . . . 28

3.8 (a) The experimental setup for resonant drive circuit characterization. (b) The equivalent circuit. . . . . 29

3.9 The measured $S_{11}$ parameter of an RLC circuit composed of a typical MEMS actuator and an external inductor $L = 2.2$ mH. . . . . 30

3.10 The measured $S_{11}$ parameter of an RLC circuit composed of a typical MEMS actuator and an external inductor (a) $L = 60$ μH (b) $L = 10$ μH. . . . . 31

3.11 The measured $S_{11}$ parameter of an RLC circuit composed of a typical MEMS actuator and an external inductor (a) $L = 950$ μH (b) $L = 675$ μH. . . . . 32

3.12 (a) A schematic and (b) a picture of the experimental setups of unbiased and biased, respectively, resonant drive experiments. . . . . 34

3.13 The frequency-response curves of the beam tip (a) displacement and (b) velocity of actuator I connected in series with a 2.2 mH inductor under resonance matching excitation with three unbiased voltage amplitudes $V_{\mathrm{AC}}$. . . . . 36

3.14 The frequency-response curve of actuator I tip displacement under a mistuned resonance matching excitation with an oversized inductor ($L = 4$ mH). . . . . 37

3.15 The frequency-response curve of actuator I velocity under a mistuned resonance matching excitation with an undersized inductor ($L = 950$ µH). . . . . 38

3.16 The frequency-response curves of actuator I tip displacement. The actuator is connected in series to two inductors, $L_1 = 470$ µH and $L_2 = 27$ µH, under actuation with three bias levels and a voltage amplitude of $V_{\mathrm{AC}} = 10$ V. . . . . 39

3.17 The frequency-response curve of actuator I′ tip displacement under a mistuned resonance matching excitation with an oversized inductor ($L = 950$ µH). . . . . 40

3.18 The frequency-response ccurve of actuator I′ tip displacement under a mistuned resonance matching excitation with an undersized inductor ($L = 675$ µH). . . . . 41

3.19 Representations of the multi-frequency signal in (a) the time and (b) frequency domains. . . . . 42

3.20 The frequency response of actuator I′ tip displacement under multi-frequency excitation ($f_e = 6.27$ MHz). . . . . 43

3.21 The frequency response of actuator I′ tip displacement under multi-frequency excitation ($f_e = 13.25$ MHz). . . . . 44

3.22 The frequency response of actuator II tip displacement under multi-frequency excitation ($f_e = 6.21$ MHz). . . . . 45

3.23 The frequency response of actuator II tip displacement under multi-frequency excitation ($f_e = 13.5$ MHz). . . . . 46

3.24 The frequency response of actuator I′ tip displacement under multi-frequency excitation ($f_e = 528$ kHz). . . . . 47

3.25 Representations of the amplitude-modulated signal in (a) the time and (b) frequency domains . $f_e$ is the carrier frequency and $f_b$ is the baseband frequency. . . 49

3.26 The frequency response of actuator I′ tip displacement under excitation with an amplitude-modulated signal where the carrier frequency is set to $f_e = 6.27$ MHz. 50

3.27 The frequency response of actuator I′ tip displacement under excitation with an amplitude-modulated signal where the carrier frequency is set to $f_e = 9.11$ MHz. 51

3.28 The frequency response of actuator I′ tip displacement under excitation with an amplitude-modulated signal where the carrier frequency is set to $f_e = 13.25$ MHz. 52

3.29 The frequency response of actuator II tip displacement under excitation with an amplitude-modulated signal where the carrier frequency is set to $f_e = 6.21$ MHz. 52

3.30 The frequency response of actuator II tip displacement under excitation with an amplitude-modulated signal where the carrier frequency is set to $f_e = 13.1$ MHz. 53

3.31 Comparison between the experimental (solid lines) and simulated (dashed lines) frequency-response curves of actuator I under conventional excitation for four levels of the voltage amplitude $V_{\mathrm{AC}}$. . . . . 60

3.32 Comparison between the experimental (solid lines) and simulated (dashed lines) frequency-response curves of actuator II under conventional excitation for six levels of the voltage amplitude $V_{\mathrm{AC}}$. . . . . 61

3.33 Comparison between the experimental (solid lines) and simulated (dashed lines) frequency-response curves of actuator II under conventional excitation for two levels of the voltage amplitude $V_{\mathrm{AC}}$. . . . . 62

3.34 Comparison between the experimental (solid lines) and simulated (dashed lines) frequency-response curves of actuator I under resonance matching with unbiased signals for four levels of the voltage amplitude $V_{\mathrm{AC}}$. . . . . 63

3.35 Comparison between the experimental (solid lines) and simulated (dashed lines) frequency-response curves of actuator I under resonance matching with biased signals for three levels of bias and a voltage amplitude of $V_{\mathrm{AC}} = 10\,\mathrm{V}$. . . . . 64

3.36 Comparison between the experimental (solid lines) and simulated (dashed lines) frequency-response curves of actuator II under multi-frequency excitation with an electrical resonance of $f_e = 6.21\,\mathrm{MHz}$, an amplifier voltage amplitude of $V_{AC1} = 7.5\,\mathrm{V}$, and four levels of the actuation voltage amplitude $V_{\mathrm{AC2}}$. . . . . 65

3.37 Comparison between the experimental (solid lines) and simulated (dashed lines) frequency-response curves of actuator II under multi-frequency excitation with an electrical resonance of $f_e = 13.5\,\mathrm{MHz}$, an amplifier voltage amplitude of $V_{\mathrm{AC1}} = 7.5\,\mathrm{V}$, and five levels of the actuation voltage amplitude $V_{\mathrm{AC2}}$. . . . . 66

3.38 FFT representation of multi-frequency signals (a) $f_1 = 6.21$ MHz and $f_2 = 4.6694$ MHz (b) $f_1 = 13.5$ MHz and $f_2 = 11.9594$ MHz . . . . . 67

3.39 The measured (solid line) and simulated (dashed line) frequency-response curves of actuator II under multi-frequency excitation with an electrical resonance of $f_e = 6.21\,\mathrm{MHz}$, an amplifier voltage amplitude of $V_{\mathrm{AC1}} = 7.5\,\mathrm{V}$ , and an actuation voltage amplitude of $V_{\mathrm{AC2}} = 1\,\mathrm{V}$. . . . . 68

3.40 Multi-frequency signals measured by an oscilloscope with common first signal frequency of $f_1 = 13.5\,\mathrm{MHz}$, second signal frequency of $f_2 = 11.9594\,\mathrm{MHz}$, and first voltage amplitude of $V_{\mathrm{AC1}} = 7.5\,\mathrm{V}$ and six levels of the second voltage amplitude: (a) $V_{\mathrm{AC2}} = 7.5\,\mathrm{V}$ (b) $V_{\mathrm{AC2}} = 6\,\mathrm{V}$ (c) $V_{\mathrm{AC2}} = 5\,\mathrm{V}$ (d) $V_{\mathrm{AC2}} = 4\,\mathrm{V}$ (e) $V_{\mathrm{AC2}} = 3\,\mathrm{V}$ (d) $V_{\mathrm{AC2}} = 2\,\mathrm{V}$. . . . . 70

3.41 The FFT of a scaled simulation of the electrostatic force under amplitude-modulated excitation with frequencies of (a) $f_e = 6.21$ MHz and $f_b = 1.54$ MHz (b) $f_e = 13.1$ MHz and $f_b = 1.54$ MHz . . . . . 71

3.42 Comparison between the experimental (solid lines) and simulated (dashed lines) frequency-response curves of actuator II under amplitude-modulated signals with an electrical resonance of $f_e = 6.21$ MHz, an amplifier voltage amplitude of $V_{\mathrm{AC1}} = 7.5$ V, and six levels of the actuation voltage amplitude $V_{\mathrm{AC2}}$. . . . . 72

3.43 Comparison between the experimental (solid lines) and simulated (dashed lines) frequency-response curves of actuator II under amplitude-modulated signals with an electrical resonance of $f_e = 13.1$ MHz, an amplifier voltage amplitude of $V_{\mathrm{AC1}} = 7.5$ V, and five levels of the actuation voltage amplitude $V_{\mathrm{AC2}}$. . . . . 73

3.44 Amplitude-modulated signals measured by an oscilloscope with common carrier frequency of $f_e = 13.1$ MHz, baseband frequency of $f_b = 1.5406$ MHz, and first voltage amplitude of $V_{\mathrm{AC1}} = 7.5$ V and four levels of the second voltage amplitude: (a) $V_{\mathrm{AC2}} = 7.5$ V (b) $V_{\mathrm{AC2}} = 6$ V (c) $V_{\mathrm{AC2}} = 5$ V (d) $V_{\mathrm{AC2}} = 4$ V. . . 74

3.45 simulated (red line) experimental (blue line) frequency response of actuator II under conventional excitation with an amplitude of $V_{\mathrm{AC}} = 15$ V and a cubic nonlinearity of $\alpha_3 = 30$. . . . . 75

3.46 The Experimental frequency-response curves of actuator II showing the frequency shift between in the response under conventional excitation (solid lines) and amplitude-modulation excitation (dashed lines). . . . . 76

4.1 A microscopic image of the actuator. . . . . 82

4.2 A schematic model of the actuator chip. . . . . 83

4.3 The experimental setup for capacitance measurement. . . . . 85

4.4 The VNA-measured overall capacitance for four actuator wiring configuration. . 85

4.5 The frequency response-curves of actuator I connected in series with a 2.2 mH inductor under unbiased resonance matching excitation with the same voltage amplitude $V_{\mathrm{AC}}$. . . . . 88

4.6 The experimental frequency-response curves of actuator II under conventional excitation with an amplitude of: (a) $V_{\mathrm{AC}} = 30$ V (b) $V_{\mathrm{AC}} = 45$ V (c) $V_{\mathrm{AC}} = 54$ V (d) $V_{\mathrm{AC}} = 60$ V. . . . . 89

4.7 (a) The experimental setup for characterization of the RLC circuit and (b) a lumped element schematic of the circuit. . . . . 91

4.8 The measured frequency response of an RLC circuit composed of a typical MEMS actuator and two external inductors: (a) $L = 950$ µH (b) $L = 675$ µH . . . . . 91

4.9 FFT of the measured tip velocity for actuator III under pulse excitation showing the response of (a) the first out-of-plane and (b) the first in-plane bending modes. 92

4.10 Non-stationary 'frequency-response' curves of actuator III beam tip velocity using four excessively fast slew rates. . . . . 93

4.11 The stationary frequency-response curve of actuator III obtained using the stitching technique. . . . . 94

5.1 Frequency response of the second out-of-plane bending mode of actuator I′. . . . 99

# List of Tables


2.1 Actuator dimensions . . . . . 10

3.1 The measured quality factors of Actuator I. . . . . 54

3.2 The measured quality factors of Actuator I′. . . . . 55

3.3 The measured quality factors of Actuator II. . . . . 57

3.4 The measured quality factors of Actuator I. . . . . 59

3.5 The predicted electrical quality factors for resonance matching excitation with (a) unbiased signals and (b) biased signals with a voltage amplitude of $V_{\mathrm{AC}} = 10\,\mathrm{V}$. 63

3.6 The electrical quality factors for multi-frequency excitation with an amplifier voltage amplitude $V_{\mathrm{AC1}} = 7.5\,\mathrm{V}$ and an electrical resonance of (a) $f_e = 6.21\,\mathrm{MHz}$ and (b) $f_e = 13.5\,\mathrm{MHz}$. . . . . 69

3.7 The electrical quality factors for amplitude modulation excitation with an amplifier voltage amplitude $V_{\mathrm{AC1}} = 7.5\,\mathrm{V}$ and an electrical resonance of (a) $f_e = 6.21\,\mathrm{MHz}$ and (b) $f_e = 13.1\,\mathrm{MHz}$. . . . . 73

3.8 Realized magnification factors for actuator I. . . . . 77

3.9 Realized magnification factors actuator II. . . . . 78

4.1 Actuator dimensions. . . . . 83

4.2 Average capacitance for four actuator wiring configuration. . . . . 86

4.3 Realized amplification of actuator II response. . . . . 90

# Chapter 1

# Introduction

## 1.1 MEMS Sensors and Actuators

Micro-Electro-Mechanical Systems (MEMS) is an emerging microfabrication technology that integrates electrical and mechanical properties into a single system. It represents a radical transformation in scale, with feature sizes ranging from one micron to several millimeters. MEMS technology has resulted in significant improvements in the overall performance of many systems, including low power consumption, sensitivity, and reliability compared to large-scale devices. Furthermore, it has introduced novel devices such as low-cost ink-jet print heads, lab-on-a-chip bio-sensors, and micromirror arrays.

MEMS utilizes the same fabrication techniques initially developed for integrated circuit (IC) technology, allowing for batch processing of thousands of devices on a single wafer which helps to improve efficiency and reduce manufacturing costs. Silicon represents the core material of MEMS technology due to its mechanical, electrical, and thermal properties, as well as its compatibility with existing manufacturing processes. Most MEMS devices are manufactured through

surface or bulk micromachining techniques [1, 2].

Bulk and surface micromachining are two common techniques used in MEMS manufacturing. One key difference between the two techniques is the way structures are defined. The structures in bulk micromachining are defined by patterning and etching inside a substrate, which results in relatively thick structures. In contrast, surface micromachining involves depositing, patterning, and etching a sequence of thin films on top of a substrate. Surface micromachining is commonly used in commercial MEMS production as it is compatible with the IC process, making it easy to integrate electrical and mechanical components onto a single chip. Bulk micromachining, however, is typically less expensive than surface micromachining as it involves fewer manufacturing processes [1, 3].

The vast majority of MEMS can be categorized as either sensors or actuators. MEMS sensors are used to detect physical changes in the environment and convert them into electrical signals [4]. They are widely utilized in many applications, such as accelerometers for vehicle airbags, pressure sensors for catheter tips, and gyroscopes for transportation and navigation systems [4, 5]. On the other hand, MEMS actuators are devices that translate different forms of energy into mechanical motion [4]. They can be used in various applications that require precise movements, such as scanning micromirrors for medical purposes like confocal microscopy, medical endoscopy, and laparoscopy [6].

## 1.2 Actuation Methods for MEMS

Actuation methods refer to the mechanisms employed to transform the input energy into mechanical motion. Different MEMS designs require different actuation approaches. The most widely used actuation techniques are electrothermal, electromagnetic, piezoelectric, and electrostatic actuation. Each method has its own advantages and limitations. Therefore, choosing

the proper actuation principle for a given MEMS device requires careful consideration of the device application, performance criteria, and the advantages and disadvantages of each actuation method.

### 1.2.1 Electrothermal Actuation

Electrothermal actuation can be utilized to achieve a desired motion, particularly in flexible microstructures [2]. This method relies on the conversion of electrical signals into mechanical motion through the thermal expansion caused by Joule heating [7]. When an electric current is applied through the microstructure, its temperature rises, and its material expands. This expansion creates thermal stress, resulting in deflection [8].

Thermal actuation is simple in terms of fabrication, operates at low voltages, and can achieve a large deflection of microstructures. However, its main disadvantage is the time required for the microstructure to reach thermal equilibrium, resulting in a slow response time. This limits its efficiency for high-frequency MEMS excitation. Moreover, thermal actuation has a high power consumption due to Joule heating. It can also cause material degradation and fatigue due to thermal stress cycles for a long period of time [2, 8].

### 1.2.2 Electromagnetic Actuation

Electromagnetic transduction has been commonly used in macro-scale applications, such as loudspeakers. It has also been explored in microdevices due to its ability to generate significant forces and large deflection at low operating voltages compared to other actuation types, such as piezoelectric [2]. For instance, Cho and Yoon [10] utilized electromagnetic actuation to displace a three-axis micromirror. At an applied current of 115 mA, the micromirror was able to

rotate 4.2°around the x-axis and 9.2°around the y-axis while achieving a deflection $42\,\mu\mathrm{m}$ along the z-axis. In all three cases, the actuation voltage is set equal to 3 V.

Despite its advantages, electromagnetic actuation has not achieved commercial success in microdevices. This is due to its drawbacks, including high power consumption caused by the need for high currents and complex fabrication processes that may involve coil fabrication and deposition of magnetic materials to create a magnetic field [1, 2].

### 1.2.3 Piezoelectric Actuation

Piezoelectric actuation is a widely used technique in MEMS that relies on the piezoelectric effect. This effect refers to the ability of a piezoelectric material to generate an electric field because of mechanical deformation. It can also work in the opposite direction, where the material undergoes mechanical deformation when subjected to an electric field [1, 9]. This effect is small. Hence, piezoelectric actuators require high actuation voltages of up to a few hundred volts [1, 11]. While this can be a disadvantage, these actuators offer several advantages, such as high force capability, fast response times typically in the millisecond range, and precise positioning mechanisms. However, a significant limitation of piezoelectric actuators is the strong hysteresis observed between the input voltage and output displacement, which can significantly degrade positioning accuracy and trigger system instability [11–15].

### 1.2.4 Electrostatic Actuation

Electrostatic actuation is popular in MEMS due to its distinct advantages, such as simple design, ease of fabrication and integration with electrical circuits, and low power consumption [16]. Furthermore, it offers a rapid response time on the order of picoseconds, which is the time constant

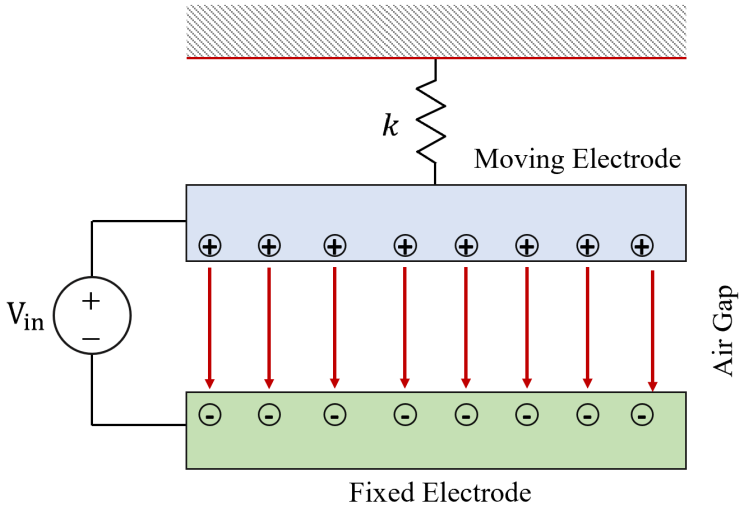



Figure 1.1: A typical electrostatic MEMS actuator.

required for charging a MEMS capacitor. Electrostatic actuation utilizes the attractive forces that arise from the electric charges of opposite polarity across two parallel electrodes, Figure 1.1, to generate force or displacement [1, 2]. The two most commonly used configurations of electrostatic actuators are based on either a two-parallel-plate capacitor consisting of a moving electrode and a fixed electrode or a comb-drive structure composed of multiple interdigitated or non-interdigitated fingers [8].

Electrostatic actuators exhibit inherent nonlinear behavior due to several factors, including nonlinear stiffness and damping, as well as the nonlinear relationship between the applied voltage and the resulting force or displacement [17]. While the nonlinearity of electrostatic actuators can provide desirable characteristics like high sensitivity in sensors [18], it can also result in pull-in instability, which is a saddle-node bifurcation that causes the moving electrode to snap into the fixed electrode when the voltage exceeds a threshold value commonly referred to as pull-in voltage. The stable travel range of the moving plate is limited to one-third of the capacitive gap by the pull-in point, which often leads to mechanical failure, dielectric charging, or stiction upon

contact between the two electrodes [19–21].

## 1.3 Resonant Drive

Electrostatic MEMS are widely utilized in various applications, such as sensors, micromirrors, micro-tweezers, and RF switches [22–25]. However, they require high voltages, typically provided by a power supply and a high-voltage amplifier. While voltage amplifiers can produce high voltages at low frequencies, they are often limited in gain at high frequencies. For instance, the Tabor 9250 amplifier has a bandwidth of up to 15 MHz, but its output voltage is limited to only $\pm$20 V [26]. Although other amplifiers in the market offer higher voltage levels, they have smaller bandwidth ranges. The Falco WMA-300 amplifier can provide an output voltage of up to $\pm$150 V, but its bandwidth is limited to only 5 MHz [27]. Similarly, the Acquitek A1230 amplifier offers an output voltage of up to $\pm$75 V, with a bandwidth that ranges from DC to 7 MHz [28]. The demand for high-sensitivity sensors and large amplitude actuators has shifted the researchers' interest to explore higher frequency MEMS [29] and different nonlinear phenomena, such as bifurcations [22], sub-harmonic, and super-harmonic resonances [30]. Hence, various methods have been proposed to amplify the voltage signal fed into the system by coupling it in series to a resonant circuit constituted by introducing an external inductor $L$. These methods are based on utilizing the electrical quality factor of an RLC circuit driven at its natural frequency to amplify the actuation voltage of the MEMS.

- Three methods have been proposed in the literature.

    1) Resonance Matching where the electrical and mechanical resonances are matched and activated simultaneously $f_e \approx f_m$ by tuning the external inductor $L$, Figure 1.2.

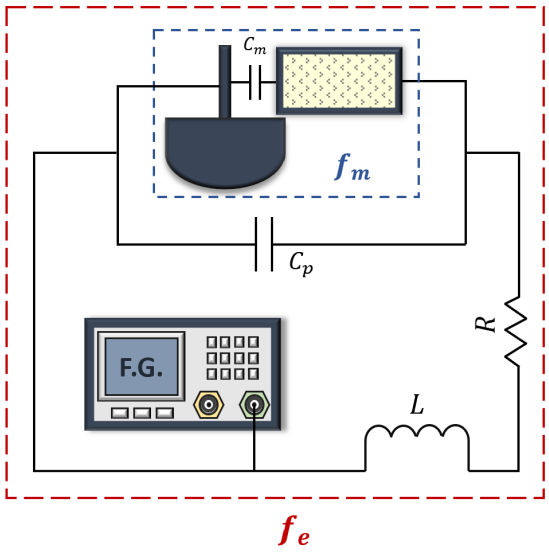



Figure 1.2: A schematic showing the electrical resonance $f_e$ of an RLC circuit and the mechanical resonance $f_m$ of a MEMS actuator.

2) Multi-frequency excitation where the MEMS is driven with a two-frequency signal. One frequency is set equal to the electric resonance $f_1 \approx f_e$ while the sum or difference of the two frequencies is set equal to the mechanical resonance $f_1 \pm f_2 \approx fm$ [32–34].

3) Amplitude Modulation (AM) where a signal that contains an RF carrier frequency and a baseband frequency is used to drive the MEMS. The LC circuit is tuned to match the carrier frequency to the electrical resonance $f_c \approx f_e$, and the baseband frequency is set equal to the mechanical resonance $f_b \approx f_m$ [35].

In this thesis, we analyzed and compared among these three resonant drive techniques. We also compared their performance to a voltage amplifier.

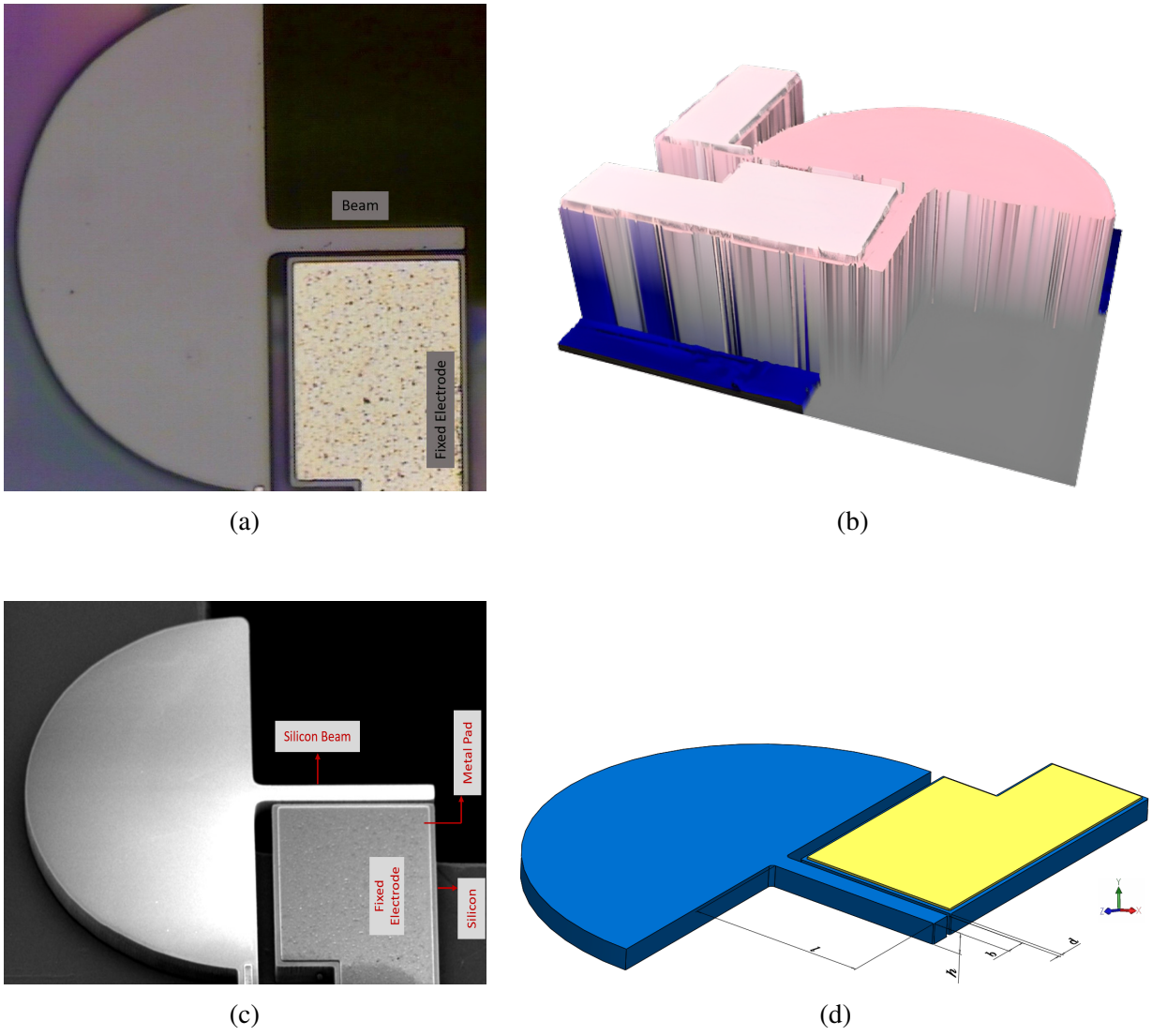
# Chapter 2

# Electrostatic MEMS Actuator

In this chapter, we introduce a decoupled electromechanical lumped-element model to investigate the behavior of a one-degree-of-freedom electrostatic actuator. The proposed model analyzes the behavior of the microbeam subjected to various excitation schemes as well as the flow of the electric charge through the circuit.

## 2.1 Actuator Design

The electrostatic MEMS actuator under study is an in-plane actuator composed of a stationary silicon electrode with a metal pad on top made of aluminum, and a movable silicon microbeam, as shown in Figure 2.1. The actuator was fabricated using the PiezoMUMPs [36] process. The substrate underneath the beam was fully etched during the fabrication. The dimensions of the actuator are listed in Table 2.1.




(a) (b)

(c) (d)

Figure 2.1: (a) A microscopic image, (b) a white light profilometer image, (c) an SEM image, and (d) a schematic of the actuator.

## 2.2 Lumped-Element Model

The proposed model studies the first out-of-plane bending mode, Figure 2.2, of the microbeam while accounting for the fringing field. The model incorporates both electrical and mechanical

Table 2.1: Actuator dimensions

| Parameter | μm |
|---|---|
| beam length ($l$) | 86 |
| beam width ($b$) | 10 |
| beam thickness ($h$) | 10 |
| capacitive gap ($d$) | 2 |

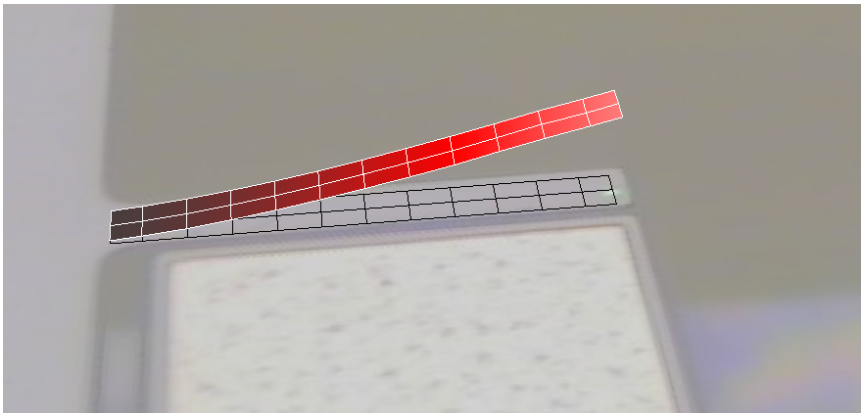


Figure 2.2: Out-of-plane bending mode.

subsystems represented as lumped parameters. The mechanical subsystem is an electrostatic MEMS actuator modeled as a simple parallel plate capacitor electrically excited by a force consisting of a static voltage $V_{\mathrm{DC}}$ and a time-varying voltage $V_{\mathrm{AC}}$, while the electrical subsystem is an LC tank constituted by introducing an external inductor $L$ connected in series with the MEMS actuator.

In lumped-parameter modeling, the spatially distributed system is assumed to be a point mass, a spring, and a damper. Thus, the effective mass of the microbeam and the distributed electrostatic force acting on the system is considered to be a point mass and a point force located at the center of the beam tip.

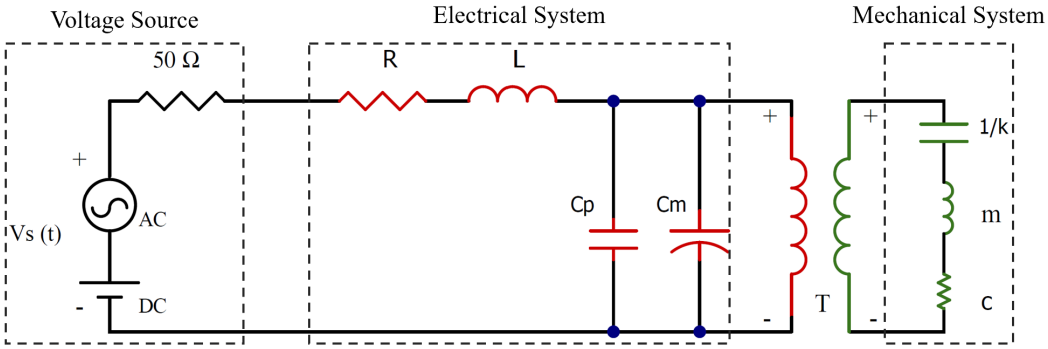



Figure 2.3: Equivalent circuit of the electromechanical system.

The equivalent circuit of the electromechanical system is presented in Figure 2.3, with the 50 Ω resistor representing the internal resistance of the voltage source. The electrical characteristics of the system is represented by a series RLC circuit, where $R$ represents the circuit's parasitic resistance, $L$ is the external inductor, and $C$ represents the total capacitance of the system, consisting of the MEMS variable capacitance $C_m$ parallel to the parasitic capacitance in the system $C_p$ due to coupling with other structures on the chip and wire bonding. The transformer $T$ represents the nonlinearities in the system and the energy flow from the electrical domain to the mechanical domain. The mechanical parameters of the system are represented in an electrical analogy, where the capacitor $\frac{1}{k}$ represents the reciprocal of the mechanical stiffness, the inductor $m$ refers to the system's effective mass, and the resistor $c$ represents mechanical damping.

### 2.2.1 Mechanical Subsystem

The potential energy $U$ stored in a parallel plate capacitor can be expressed as

$$U = \frac{1}{2} CV^2 \tag{2.1}$$

where $V$ is the voltage across the MEMS capacitor. The total capacitance of the system $C$ can be written as

$$C = C_m + C_p \tag{2.2}$$

The model describes the transverse deflection of the microbeam along the vertical (y-direction), Figure 2.4, as it moves up and down due to the asymmetry in the electrostatic field between the beam and the fixed electrode. This asymmetry arises from the aluminum pad on top of the stationary electrode. The gap between the fixed electrode and the beam $d$ is assumed to remain unchanged during this motion, while the overlap area varies along the y-direction. Consequently, the MEMS capacitance can be written as

$$C_m = \frac{\epsilon\, l\, (h+ \mid w_\circ - w \mid)}{d} \tag{2.3}$$

where $\epsilon = \epsilon_\circ \epsilon_r$, $\epsilon_\circ$ is the permittivity of free space, $\epsilon_r$ is the permittivity of the medium (air), and $w$ is the out-of-plane displacement in the $y$-direction. We assume that the top surface of the beam is initially parallel to the top surface of the metal pad on top of the fixed electrode and $w_\circ$ is the metalizat thickness. The metalization layer thickness was measured using a white light profilometer and found to be $w_\circ = 0.7$ µm.

To account for the fringing field, the capacitance expression is modified [37] such as

$$C_f = \beta C \tag{2.4}$$

where $\beta$ is

$$\beta = \kappa\Big(1.13 \times 10^{-6} \left(\frac{b}{d}\right)^3 - 0.00019 \left(\frac{b}{d}\right)^2 + 0.013\left(\frac{b}{d}\right) + 1.638\Big) \tag{2.5}$$

and $\kappa$ is a factor that accounts for the geometry of the resonator's fringing field during the out-of-plane motions, Figure 2.4.

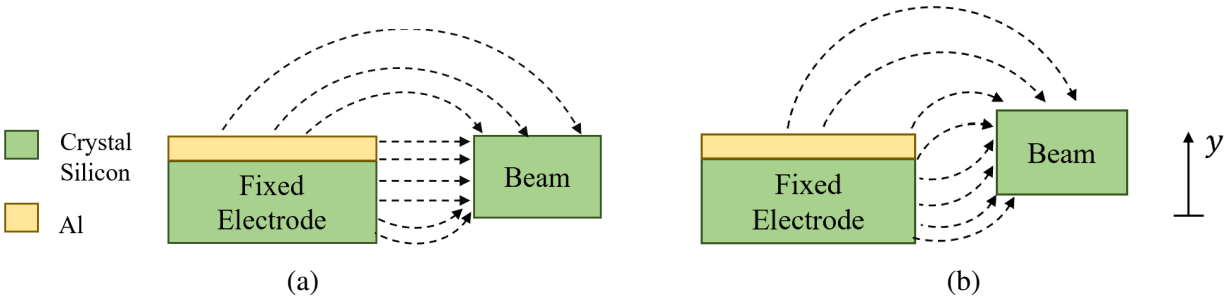



Figure 2.4: Electrostatic field of the actuator at (a) equilibrium (b) out-of-plane motion.

The electrostatic force for voltage controlled actuator can be derived as

$$F_{es} = -\frac{\partial U}{\partial w} = \frac{1}{2}\,\frac{\partial C_f}{\partial w}\,V^2 = \beta\,\frac{\epsilon\,l\,V^2}{2\,d}\;\mathrm{sgn}(w_\circ - w) \tag{2.6}$$

where

$$\mathrm{sgn}(w) = \begin{cases} 1 & \text{for} \quad w > 0 \\ 0 & \text{for} \quad w = 0 \\ -1 & \text{for} \quad w < 0 \end{cases}$$

The total mass of the microbeam $m_T$ can be written in the form

$$m_T = \rho\,l\,h\,b \tag{2.7}$$

where $\rho$ is the material density. The effective mass $m$ can be estimated from [38]

$$m = \frac{33}{140}\,m_T \tag{2.8}$$

The equation of motion for a spring-mass-damper representation of the actuator can be expressed as

$$m\ddot{w} + c\dot{w} + kw = F_{es} \tag{2.9}$$

where $c$ is the damping coefficient and k is the effective stiffness. Inserting the expression for the electrostatic force, Eq. (2.6), we can rewrite the equation of motion as

$$m\ddot{w} + c\dot{w} + kw = \frac{\epsilon\,\beta\,l\,V(t)^2}{2d}\ \mathrm{sgn}(w_\circ - w) \tag{2.10}$$

Rearranging, the equation simplifies to

$$\ddot{w} + \frac{\omega_m}{Q_m}\,\dot{w} + \omega_m^2\,w = \frac{\epsilon\,\beta\,l\,V(t)^2}{2m\,d}\ \mathrm{sgn}(w_\circ - w) \tag{2.11}$$

where $\omega_m = \sqrt{\frac{k}{m}}$ is the undamped angular natural frequency of the uncoupled mechanical subsystem and $Q_m$ is its quality factor.

### 2.2.2 Electrical Subsystem

The equation of motion for an RLC circuit can be written as

$$L\ddot{q} + R\dot{q} + \frac{1}{C}q = V_\mathrm{s}(t) \tag{2.12}$$

where $V_s(t)$ is the source voltage of the circuit. Rearranging and using Eqs. (2.2) yields

$$\ddot{q} + \frac{R}{L}\,\dot{q} + \frac{1}{L(C_m + C_p)}\,q = \frac{V_\mathrm{s}(t)}{L} \tag{2.13}$$

Substitute for the MEMS capacitance with Eq. (2.3) and simplifying results in

$$\ddot{q} + \frac{R}{L}\,\dot{q} + \frac{d}{L(C_p\,d + \epsilon\,h\,l\, + \epsilon\mid w_\circ - w \mid l)}\,q = \frac{V_{\rm s}(t)}{L} \tag{2.14}$$

### 2.2.3 Nondimensionalization

We introduced the following nondimensional parameters to nondimensionalize the equations of motion

$$\hat{t} = \frac{t}{T}\,, \quad \hat{w} = \frac{w}{\ell}\,, \quad \hat{q} = \frac{q}{C_\circ} \tag{2.15}$$

where $T = \sqrt{\frac{m}{k}}$ is a time-scale, $\ell = 0.01h$ is the resonator's characteristic length, and $C_\circ$ is the nominal capacitance at zero displacement and 1 V. Hence,

$$\dot{w} = \frac{\partial w}{\partial t} = \frac{\partial(h\hat{w})}{\partial(T\hat{t})} = \frac{\ell}{T}\dot{\hat{w}} \tag{2.16}$$

$$\ddot{w} = \frac{\partial \dot{w}}{\partial t^2} = \frac{\partial(h\hat{w})}{\partial(T^2\hat{t^2})} = \frac{\ell}{T^2}\ddot{\hat{w}} \tag{2.17}$$

$$\dot{q} = \frac{\partial q}{\partial t} = \frac{\partial(C_\circ\hat{q})}{\partial(T\hat{t})} = \frac{C_\circ}{T}\dot{\hat{q}} \tag{2.18}$$

$$\ddot{q} = \frac{\partial \dot{q}}{\partial t^2} = \frac{\partial(C_\circ\hat{q})}{\partial(T^2\hat{t^2})} = \frac{C_\circ}{T^2}\ddot{\hat{q}} \tag{2.19}$$

Using Eqs. (2.15)–(2.17) in Eq. (2.11) yields

$$\frac{\ell}{T^2}\,\ddot{\hat{w}} + \frac{\ell}{T}\,\frac{\omega_m}{Q_m}\,\dot{\hat{w}} + \ell\,\omega_m^2\hat{w} = \frac{\epsilon\,\beta\,l\,V(\hat{t})^2}{2m\,d}\ \mathrm{sgn}(\hat{w}_\circ - \hat{w}) \tag{2.20}$$

Multiplying by $\frac{T^2}{h}$, we obtain

$$\ddot{\hat{w}} + \frac{1}{Q_m}\,\dot{\hat{w}} + \hat{w} = \frac{\epsilon\,\beta\,l\,T^2\,V(\hat{t})^2}{2\ell\,m\,d}\;\mathrm{sgn}(\hat{w}_\circ - \hat{w}) \tag{2.21}$$

where the nondimensional natural frequency of the mechanical subsystem is set to unity $\hat{\omega}_m = 1$. Dispensing with the over-hat for the sake of simplicity, we can rewrite the equation of motion as

$$\ddot{w} + \frac{1}{Q_m}\,\dot{w} + w = \alpha\,V(t)^2\;\mathrm{sgn}(w_\circ - w) \tag{2.22}$$

where a transduction parameter $\alpha = \frac{\epsilon\,\beta\,l\,T^2}{2\ell\,m\,d}$ has been introduced.

Substituting with Eqs. (2.15), (2.18), and (2.19) into Eq. (2.14), we obtain

$$\frac{C_\circ}{T^2}\,\ddot{\hat{q}} + \frac{C_\circ}{T}\,\frac{R}{L}\,\dot{\hat{q}} + \frac{C_\circ\,d}{L\gamma(\hat{w})}\,\hat{q} = \frac{V_\mathrm{s}(\hat{t})}{L} \tag{2.23}$$

where the capacitance parameter

$$\gamma(\hat{w}) = C_p\,d + \ell\,\epsilon\,l + \ell\,\epsilon\;\mid \hat{w}_\circ - \hat{w} \mid l$$

Multiplying by $\frac{T^2}{C_\circ}$, and dropping the over-hat for the sake of simplicity, we can write the nondimensional equation as

$$\ddot{q} + T\,\frac{R}{L}\,\dot{q} + \frac{T^2 d}{L\gamma(w)}\,q = \frac{T^2}{C_\circ}\,\frac{V_\mathrm{s}(t)}{L} \tag{2.24}$$

and rearrange it as

$$\ddot{q} + \frac{\omega_e}{Q_e}\,\dot{q} + \omega_e^2 q = \frac{T^2}{C_\circ}\,\frac{V_\mathrm{s}(t)}{L} \tag{2.25}$$

where the electrical subsystem quality factor is defined as

$$Q_e = \frac{1}{R}\sqrt{\frac{Ld}{\gamma(w)}}$$

and a nondimensional parameter defined as

$$\omega_e = T\sqrt{\frac{d}{L\gamma(w)}}$$

has been introduced. This parameter arises from the natural frequency of the uncoupled electrical subsystem

$$\omega_{eo} = T\sqrt{\frac{d}{L\gamma(0)}}$$

### 2.2.4 Static Analysis

We solve for the static equilibrium of the system by setting the time varying variables in the system equations, Eqs. (2.22) and (2.24), equal to zero, substituting with $w = w_s$ and $q = q_s$, and rearranging to obtain

$$w_s = \alpha\, V_{\mathrm{DC}}^2\, \mathrm{sgn}(w_\circ - w_s) \tag{2.26}$$

$$q_s = \frac{\gamma(w_s)}{C_\circ d}\, V_{DC} \tag{2.27}$$

### 2.2.5 Dynamic Analysis

The effective stiffness of the system will be calculated from experimental measurements of the damped natural frequency as

$$k = m\, w_m^2 \tag{2.28}$$

In chapter 3, the model will be used to generate frequency-response curves for comparison with those measured experimentally for two actuators dubbed actuator I and actuator II, Figure 2.1. Their frequency response is obtained by amplifying the excitation signal through a voltage amplifier or the resonant drive technique.

All model parameters have been described above except for the excitation voltage. It is important to note that the voltage amplification in the resonant techniques occurs within the half-power bandwidth of an electrically resonant RLC circuit and is, therefore, frequency dependent. To derive an equation for the frequency-dependent voltage, we start by expressing the overall voltage in the circuit as

$$V_{\mathrm{AC}} = IZ \tag{2.29}$$

where $I$ is the total current and $Z$ is the circuit impedance

$$Z = \sqrt{R^2 + (x_{\mathrm{L}} - x_{\mathrm{C}})^2} \tag{2.30}$$

where $x_L$ is the inductive reactance and $x_C$ is the capacitive reactance written as

$$x_{\mathrm{L}} = \Omega L, \qquad x_{\mathrm{C}} = \frac{1}{\Omega C} \tag{2.31}$$

where $\Omega = 2\pi f$ is the dimensional signal frequency. Since the capacitance of the MEMS ac-

tuator is negligible compared to parasitic capacitance $C_p >> C_m$, we will account only for its capacitance at zero displacement in the total (system) capacitance $C_\circ$ and write

$$x_{\mathrm{C}} \approx \frac{1}{\Omega C_\circ} \tag{2.32}$$

Using the voltage divider rule, we can write the amplified time-varying voltage $V_{\mathrm{C}}$ across the capacitor as

$$V_{\mathrm{C}} = \frac{V_{\mathrm{AC}}\, x_{\mathrm{C}}}{Z} \tag{2.33}$$

Substituting with Eqs. (2.30)–(2.32) yields

$$V_{\mathrm{C}} = \frac{V_{\mathrm{AC}}\,(\frac{1}{\Omega C_\circ})}{\sqrt{R^2 + (\Omega L - \frac{1}{\Omega C_\circ})^2}} \tag{2.34}$$

Rearranging, we obtain

$$V_{\mathrm{C}} = \frac{V_{\mathrm{AC}}}{\sqrt{(1 - \Omega^2 L C_\circ)^2 + (\Omega R C_\circ)^2}} \tag{2.35}$$

The maximum voltage across the system capacitor occurs at electrical resonance $\Omega = \frac{\omega_{eo}}{T} = \frac{1}{\sqrt{LC_\circ}}$ and can be written as

$$V_{\mathrm{Cr}} = \frac{V_{\mathrm{AC}}}{\sqrt{\frac{1}{LC_\circ}\, R^2 C_\circ^2}} \tag{2.36}$$

Noting that the electrical subsystem quality factor is $Q_e = \frac{1}{R}\sqrt{\frac{L}{C_\circ}}$, we can rewrite the maximum

capacitor voltage as

$$V_{\mathrm{Cr}} = Q_e \, V_{\mathrm{AC}} \tag{2.37}$$

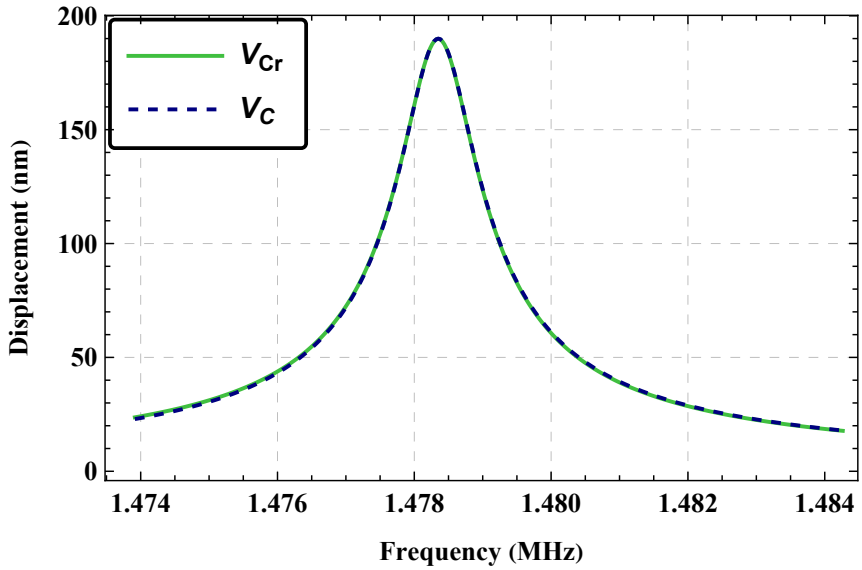



Figure 2.5: Constant amplification $V_{\mathrm{Cr}}$ vs. frequency dependent amplification $V_{\mathrm{C}}$.

We hypothesize that the frequency independent $V_{\mathrm{Cr}}$ can be used to represent the voltage across the MEMS instead of the frequency dependent $V_{\mathrm{C}}$, since the first term in the denominator of Eq. (2.35) is negligible ($\Omega^2 \approx LC_{\circ}$) throughout the frequency range of interest (the half-power bandwidth of the MEMS). To test this hypothesis, we compare in Figure 2.5, the frequency-response curves of the MEMS obtained by numerically integrating its equation of motion, Eq. (2.22), driven by the resonance matching excitation technique. In one case shown in green solid line, the amplitude of the voltage signal $V(t)$ is set to $V_{\mathrm{Cr}}$. In another case shown in black dashed line, the amplitude $V(t)$ is set to $V_{\mathrm{C}}$. No significant differences can be seen between the two cases. Thus, we will use $V_{\mathrm{Cr}}$ instead of $V_{\mathrm{C}}$ for simplicity.

# Chapter 3

# Results

In this chapter, we experimentally characterize the actuators and circuits under test then use them to investigate the frequency responses of two electrostatically actuated MEMS resonators, actuator I and actuator II, under ambient air conditions. The primary focus of the experiments is to compare among the responses of the first out-of-plane bending mode of the actuators under various excitation techniques.

## 3.1 Characterization

In this section, we present the modal analysis carried out to determine the resonant frequency of the actuators. The actuators share the same design, Figure 2.1, and dimensions, Table 2.1. The chip containing the actuators was placed into a DIP-40 chip carrier and the actuators-under-test were wire-bonded to it to reduce parasitic incurred through probing.

### 3.1.1 Experimental Setup

The experimental setup shown in Figure 3.1 was utilized to characterize the actuators. The chip carrier is placed on a breadboard under the Polytec UHF-120 Laser Doppler Vibrometer (LDV) [39] to measure the beam tip displacement optically. The Liquid Instruments' Moku:Pro [40] served as a function generator to feed the excitation signal to a high voltage amplifier, Tabor Electronics-9400 [41]. The actuation signal was supplied to the fixed electrode while the microbeam was grounded.

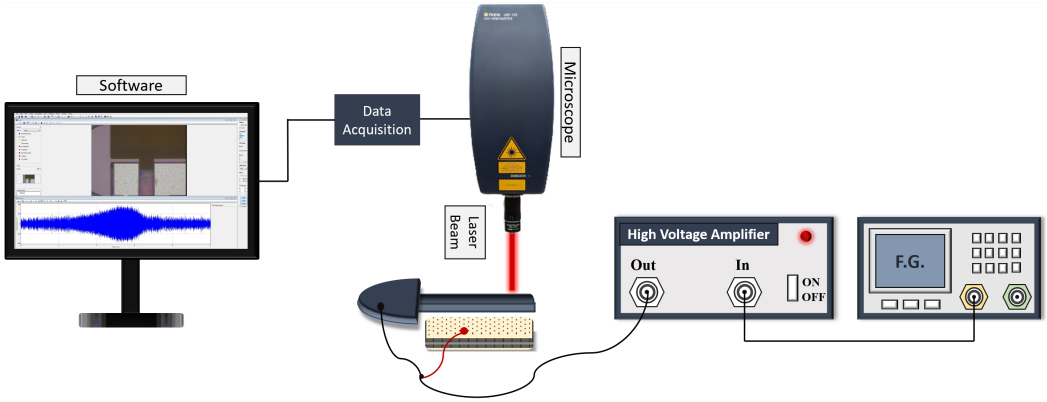



Figure 3.1: The experimental setup for actuator characterization.

### 3.1.2 Modal Analysis

For the initial characterization, the damped natural frequencies of the actuators were obtained by applying a pulse train with a 0.01% duty cycle and a 312.5 Hz frequency to the fixed electrode. The Fast Fourier Transform (FFT) of the measured tip displacement to a single pulse was obtained using the LDV software, PSV [42], and averaged over 30 samples.

For actuator I, Figure 3.2, the first out-of-plane bending mode of was found at $f_{\text{out}} = 1.4781\,\text{MHz}$, Figure 3.2. The first in-plane bending mode was found at $f_{\text{in}} = 1.6956$ MHz.

They were distinguished by the high variability in the in-plane mode peak, compared to that of the out-of-plane mode, as the laser spot of the LDV was moved across the beam width. The quality factors of the modes were calculated using the half-power bandwidth method from the measured FFT as $Q_{\text{out}} = 1211$, corresponding to a settling time of $t_s = Q_{\text{out}}T_{\text{out}} = 0.81929$ ms, and $Q_{\text{in}} = 720.5$, corresponding to a settling time of $t_s = Q_{\text{in}}T_{\text{in}} = 0.42492$ ms.

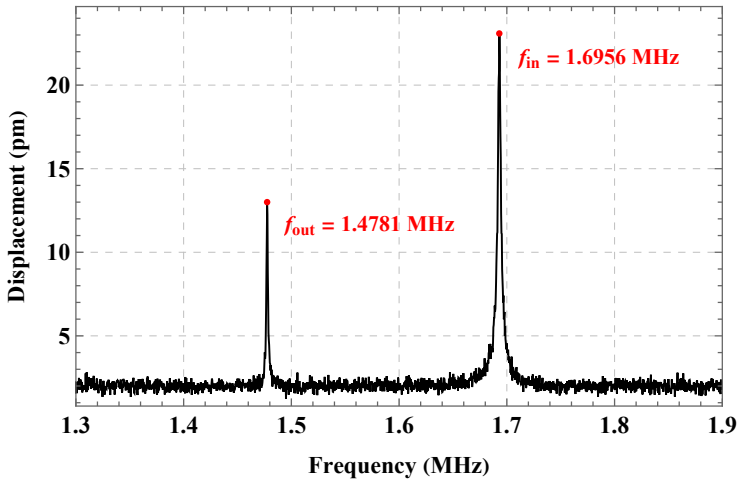
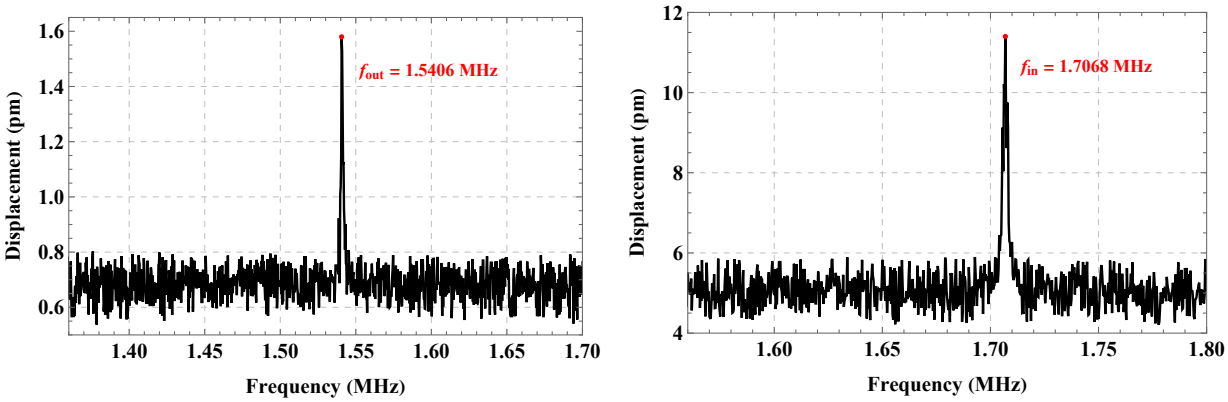



Figure 3.2: FFT of the measured tip displacement under a pulse excitation showing the first out-of-plane and in-plane bending modes of actuator I.

For actuator II, the first out-of-plane bending mode was observed at $f_{\text{out}} = 1.5406$ MHz under a voltage amplitude of 100 V, Figure 3.3(a). The first in-plane bending mode was measured at $f_{\text{in}} = 1.6956$ MHz under an amplitude of 150 V, Figure 3.3(b). The quality factors of the modes were calculated using the half-power bandwidth method from the measured FFT as $Q_{\text{out}} = 1100.5$, corresponding to a settling time of $t_s = Q_{\text{out}}T_{\text{out}} = 0.71432$ ms, and $Q_{\text{in}} = 685.5$, corresponding to a settling time of $t_s = Q_{\text{in}}T_{\text{in}} = 0.40161$ ms.

Although both actuators share the same design, they exhibit different resonance frequencies due to chip-to-chip variability in the fabrication process.




(a) (b)

Figure 3.3: FFT of the measured tip displacement for actuator II under pulse excitation showing the response of (a) the first out-of-planeand (b) the first in-plane bending modes.

## 3.2 Conventional Excitation

We obtained the frequency response of the actuators under various excitation levels through a conventional excitation scheme following the experimental setup shown in Figure 3.1. These curves serve as the 'ground truth' for comparison with the results obtained from the resonant drive techniques.

The response of the first out-of-plane bending mode was measured under an unbiased voltage waveform. Due to the quadratic nature of the electrostatic force, applying a signal with a frequency $f$ to the actuator results in an electrostatic excitation at $2f$

$$F_{es}(t) \propto \alpha V(t)^2 = \alpha(V_{\mathrm{AC}}\cos(2\pi f t))^2 = \alpha\frac{V_{\mathrm{AC}}^2}{2} + \alpha\frac{V_{\mathrm{AC}}^2}{2}\cos(4\pi f t) \tag{3.1}$$

For example, to excite actuator I the signal frequency was swept-up in the frequency range $f = [737 - 741]$ kHz resulting in an excitation frequency range of $2f = [1.474 - 1.482]$ MHz which covers the half-power bandwidth of its first out-of-plane mode. The beam's tip displacement was

recorded over a time window of 100 ms, with a sampling frequency of 100 MHz. The sweep time was set to more than 10 times longer the settling time $t_s$ to minimize transients ion the response. The frequency-response curves, Figure 3.4, were obtained for four signal amplitudes $V_{\mathrm{AC}}$ by post-processing the measured displacement to evaluate its RMS over a moving time window extending over 180 excitation periods. The reported voltage amplitudes $V_{\mathrm{AC}}$ are those obtained from the voltage amplifier.

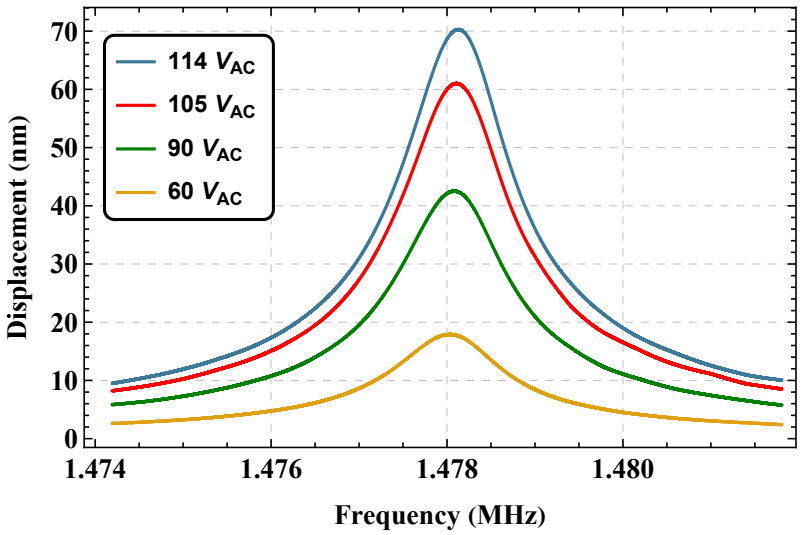



Figure 3.4: The frequency-response curves of actuator I beam tip displacement under four levels of the amplified voltage amplitude $V_{\mathrm{AC}}$.

The largest RMS displacement for this excitation scheme was $w_{\mathrm{RMS}} = 70.28$ nm obtained for the highest voltage amplitude $V_{\mathrm{AC}} = 114\,\mathrm{V}$ at resonance. It corresponds to only 3.5% of the air gap. It is worth mentioning that the voltage amplifier utilized to obtain those curves was operating beyond its specifications. Although its declared gain is x50, the input voltage in the MEMS measured by an oscilloscope was found to represent a gain of x60 in this frequency range.

During the experimental campaign, it was observed that the resonant frequency of actuator I has dropped by 500 Hz, indicating a degradation in its stiffness. Results obtained after degrada-

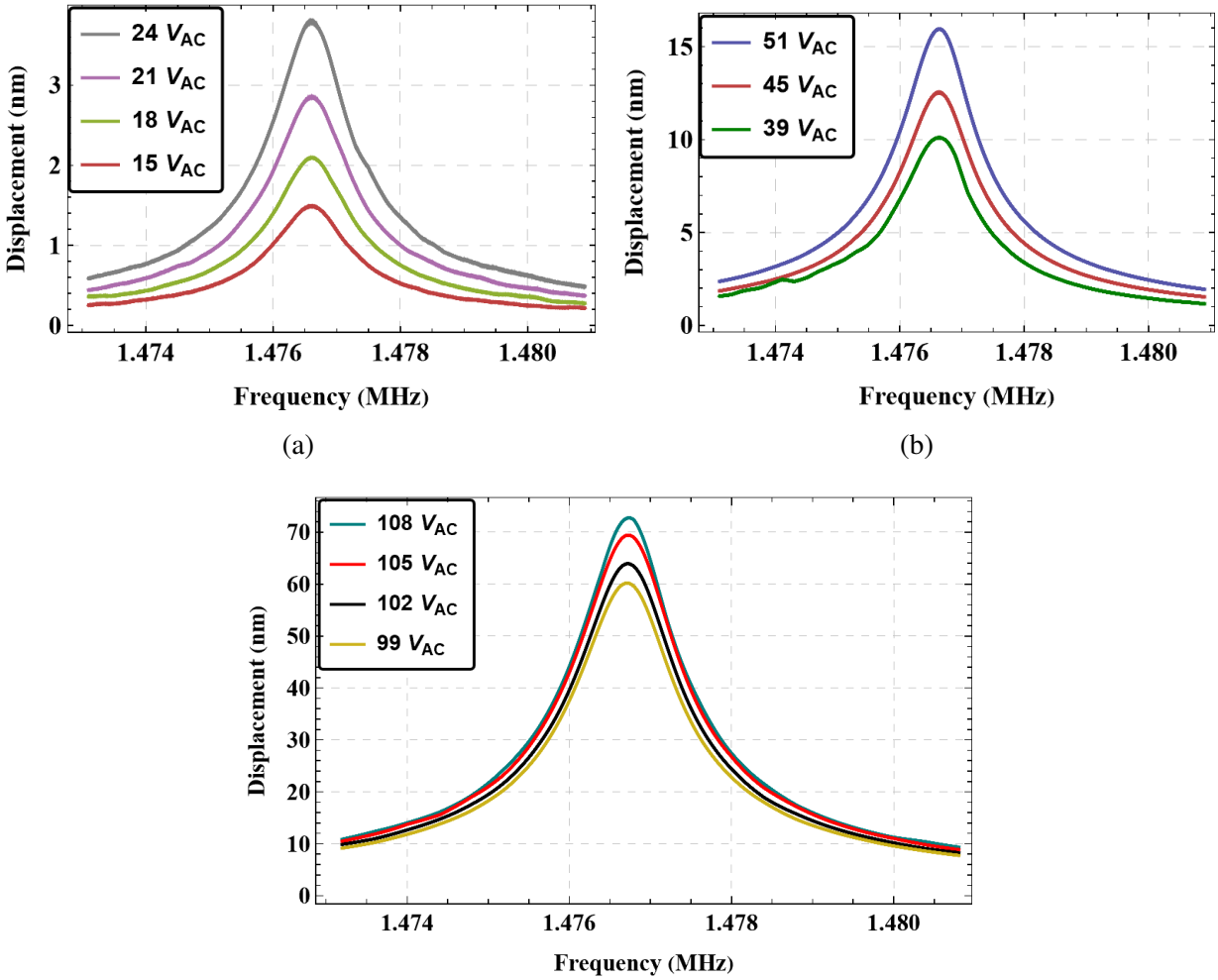



Figure 3.5: The frequency-response curves of the beam tip displacement of actuator I′ under eleven levels of the amplified voltage amplitude $V_{\mathrm{AC}}$.

tion are dubbed as those of actuator I′. Figure 3.5 shows the frequency response of actuator I′ to 11 unbiased and amplified voltage amplitudes $V_{\mathrm{AC}}$. For comparison, under a voltage amplitude of $V_{\mathrm{AC}} = 105$ V, the peak response of actuator I, Figure 3.4, is $w_{\mathrm{RMS}} = 61$ nm, whereas actuator that of I′is $w_{\mathrm{RMS}} = 69$ nm, Figure 3.5(c), indicating a drop in beam stiffness. Similarly, for a voltage amplitude of $V_{\mathrm{AC}} = 90$ V, actuator I achieved a displacement of $w_{\mathrm{RMS}} = 43$ nm at

resonance compared to a displacement of $w_{\mathrm{RMS}} = 60\,\mathrm{nm}$ for actuator I′.

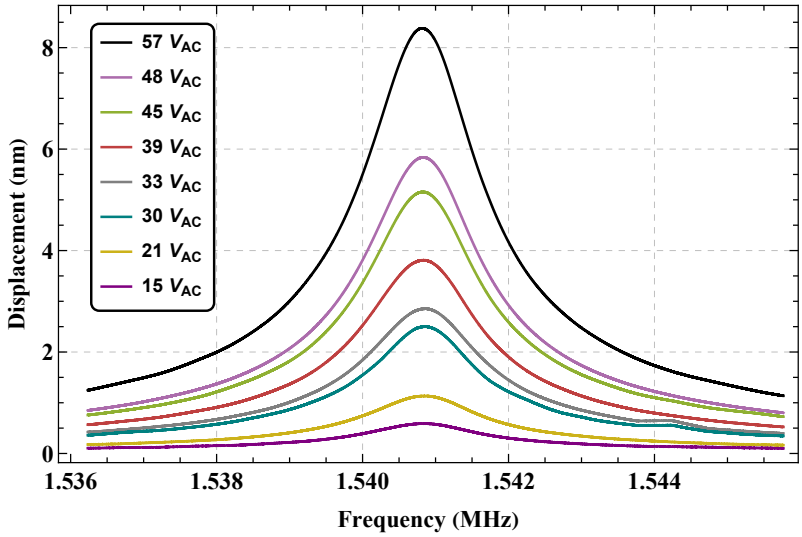



Figure 3.6: The frequency-response curves of actuator II beam tip displacement for eight levels of the amplified voltage amplitude $V_{\mathrm{AC}}$.

The frequency response of actuator II was obtained using the same experimental procedure. The frequency-response-curves for eight levels of the amplified voltage amplitude $V_{\mathrm{AC}}$ are shown in Figure 3.6. The excitation frequency was swept-up in the vicinity of the first out-of-plane bending mode over a frequency range of $2f = [1.536 - 1.546]$ MHz. The maximum measured displacement was $w_{\mathrm{RMS}} = 8.3$ nm observed at resonance under a voltage amplitude of $V_{\mathrm{AC}} = 57\,\mathrm{V}$.

For comparison, we shown in Figure 3.7 the frequency response of actuator II driven directly by the function generator alone for two signal amplitudes. We note that the maximum RMS displacement achieved was $w_{\mathrm{RMS}} = 250$ pm, which is only 0.01285% of the air gap.

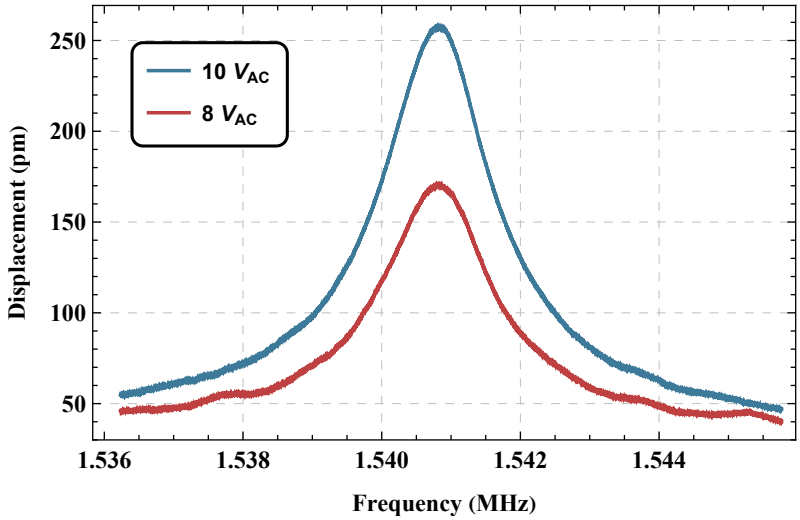



Figure 3.7: The frequency-response curves of actuator II beam tip displacement under two levels of the voltage amplitude $V_{\mathrm{AC}}$.

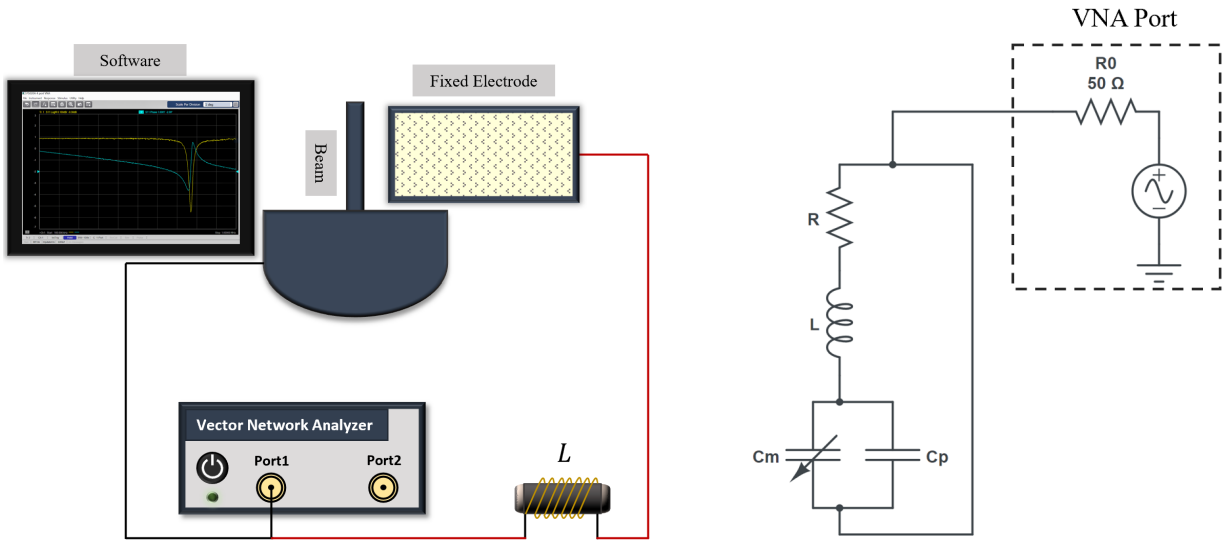
## 3.3 Resonant Drive

In this section, we describe the experimental procedure used to characterize the circuits of the resonant drive techniques, the characterization of those circuits, and the measured response of the actuators under these excitation regimes.

### 3.3.1 Electrical Characterization

The experimental setup shown in Figure 3.8(a) was used to measure the natural frequency $f_e$ of series RLC circuits consisting of an external inductor $L$, the circuit parasitic resistance $R$, the capacitance of the actuator $C_m$, and the circuit parasitic capacitance $C_p$. A lumped-element representation of the circuit is shown in Figure 3.8(b). The measurements were carried out using a Vector Network Analyzer (VNA) (Keysight P5020A). To simplify the measurement process, only a 1-port S-parameter $S_{11}$ measurements were undertaken. It represents the ratio of the reflected

wave to the incident wave as a function of frequency at the input port of the circuit. A calibration process was performed prior to measurements to account for the parastics presented by cables and connectors. Calibration was carried out using the short-open-load calibration approach with the Keysight 85521A Mechanical Calibration Kit.




(a) (b)

Figure 3.8: (a) The experimental setup for resonant drive circuit characterization. (b) The equivalent circuit.

To characterize the RLC circuit, the power level of the VNA was set to 0 dBm (1 mW). The input signal frequency was swept in the range $f = [0.1 - 1]$ MHz, with a step frequency of 1 kHz. The intermediate frequency bandwidth (IF-BW) was set to 1 kHz, and the data was averaged over 5 samples. The amplitude and phase of the frequency response of the RLC circuit are shown in Figure 3.9 when a 2.2 mH inductor was connected in series with the actuator, Figure 2.1. The magnitude of $S_{11}$ is represented in a linear scale, while the phase is shown in degrees. The electrical resonance was found at the minimum value of the $S_{11} = 0.873$ as $f_e = 780$ kHz. The corresponding phase angle swung from a minimum of $-3.5°$ to a maximum of $0.25°$. The

electrical quality factor of the RLC circuit was calculated using the half power bandwidth method from the measured $S_{11}$ magnitude as $Q_e = 54.35$. It was also found that the natural frequencies of the circuits were insensitive to the MEMS actuator in them but varied with the inductor and parastics in the circuit.

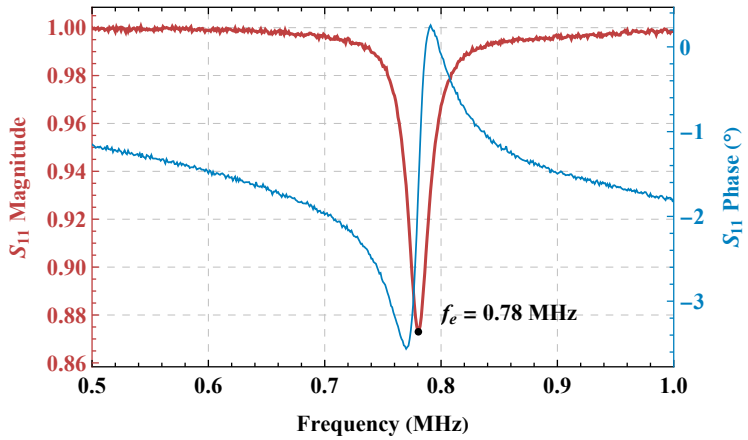
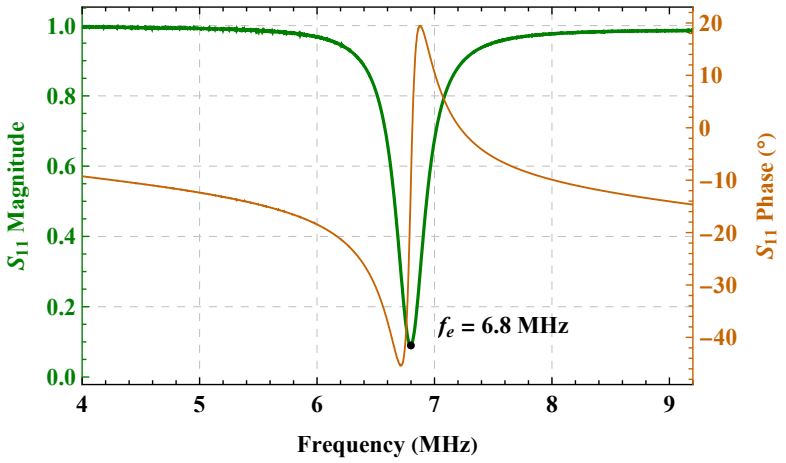


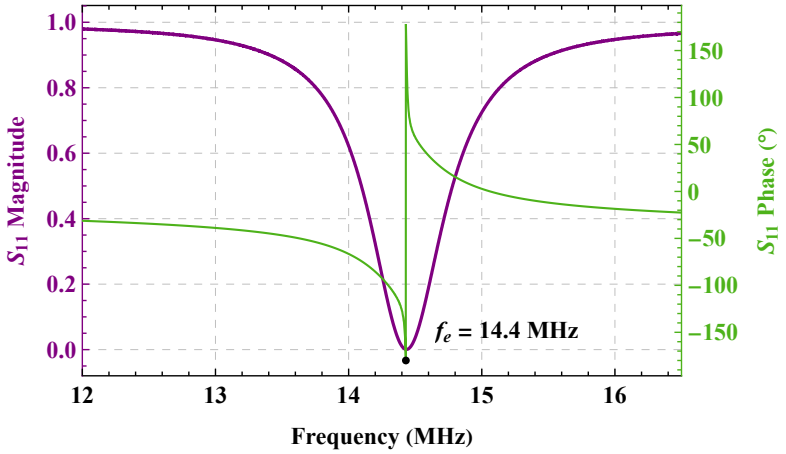

Figure 3.9: The measured $S_{11}$ parameter of an RLC circuit composed of a typical MEMS actuator and an external inductor $L = 2.2$ mH.

Next, we characterized the resonant circuit with $60$ µH and $10$ µH inductors. The signal frequency was swept in the range $f = [3 - 15]$ MHz and the IF-BW was set to 2 kHz. The amplitude and phase of the frequency response of the RLC circuit are shown in Figure 3.10(a) when a 60 µH was connected to the actuator. The electrical resonance was found at the minimum value of $S_{11} = 0.0898$ to be $f_e = 6.8$ MHz and the corresponding phase angle swung from a minimum of $-45.4°$ to a maximum of $19.4°$. The calculated quality factor in this case was found to be $Q_e = 35.15$.

Figure 3.10(b) shows the $S_{11}$ magnitude and phase of the frequency response of the resonant circuit when a $10$ µH inductor is connected with the actuator. The electrical resonance was found at the minimum value of $S_{11} = 0.0006$ to be $f_e = 14.4$ MHz and the corresponding phase angle




(a)




(b)

Figure 3.10: The measured $S_{11}$ parameter of an RLC circuit composed of a typical MEMS actuator and an external inductor (a) $L = 60$ µH (b) $L = 10$ µH.

swung from a minimum of $-176.6°$ to a maximum of $178.3°$. The calculated quality factor in this case was found to be $Q_e = 32.58$.

The resonant circuit was characterized with a $5.6$ mH, a $950$ µH and a $675$ µH inductors. The signal frequency was swept in the range $f = [0.15 - 15]$ MHz with a step of $5$ kHz and the IF-BW was set to $1$ kHz. The magnitude of the $S_{11}$ is e shown in Figure 3.11(a) when a $5.6$

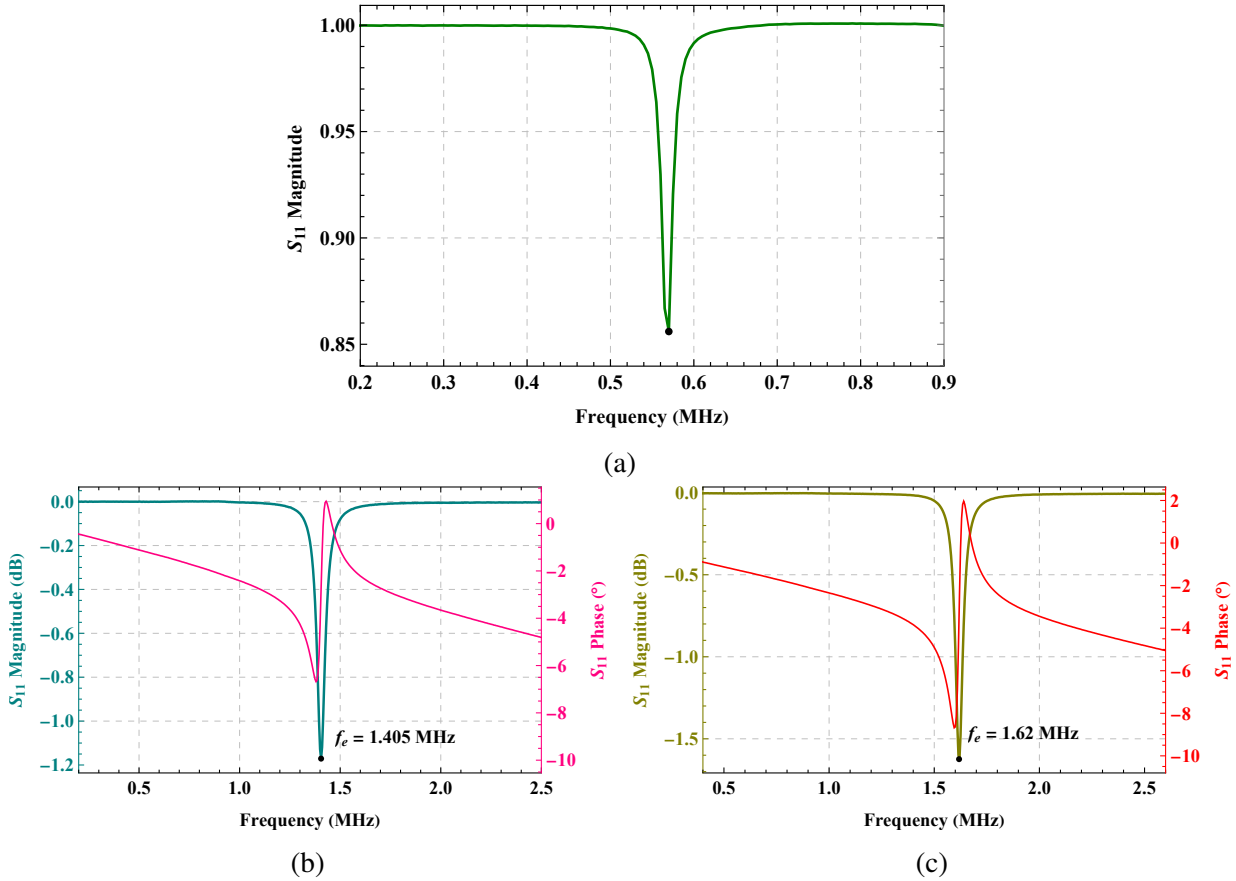



Figure 3.11: The measured $S_{11}$ parameter of an RLC circuit composed of a typical MEMS actuator and an external inductor (a) $L = 950$ µH (b) $L = 675$ µH.

µH, composed of two series inductors 2.4 mH and 3.2 mH, was connected to the actuator. The electrical resonance was found at the minimum value of $S_{11} = 0.856236$ to be $f_e = 0.57$ MHz and the quality factor was calculated as $Q_e = 69.9$.

The $S_{11}$ magnitude, in dB, and phase of the frequency response of the RLC circuit are shown in Figure 3.11(b) when a $950$ µH was connected to the actuator. The electrical resonance was found at the minimum value of $S_{11} = -1.17$ dB to be $f_e = 1.405$ MHz and the corresponding phase angle at resonance swung from a minimum of $-6.67°$ to a maximum of $0.94°$.

Figure 3.11(c) shows the magnitude and phase of the frequency response of the resonant circuit a $675$ μH inductor is connected in series with the actuator. The electrical resonance occurred at a minimum value of $S_{11} = -1.62$ dB corresponding to a frequency of $f_e = 1.62$ MHz. The phase angle at this resonance swung from a minimum of $-8.68°$ to a maximum of $1.96°$.

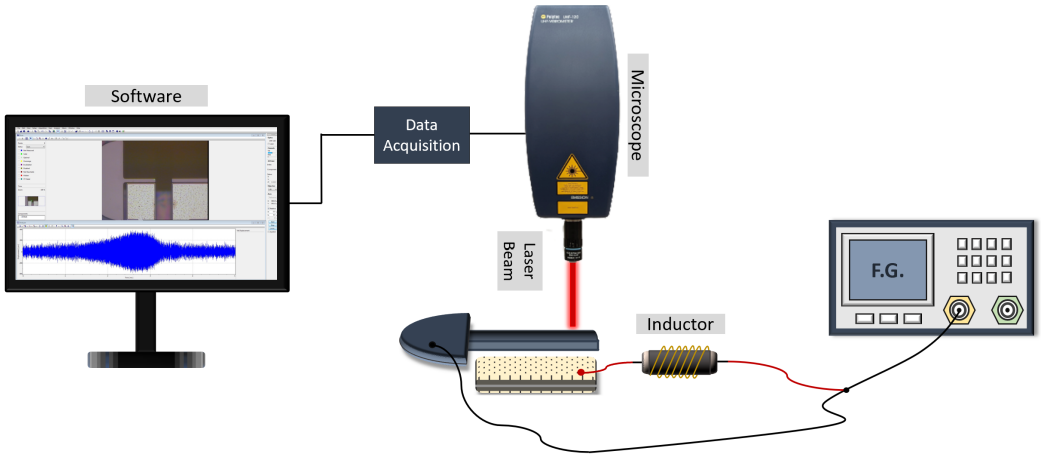
### 3.3.2 Experimental Setup

The experimental setup for the resonant drive experiments is shown in Figure 3.12. The fixed electrode of the actuator is connected in series to an external inductor to tune the electrical natural frequency of the circuit. The LDV [39] is used to measure the tip displacement. The ground of the function generator (Liquid Instruments' Moku:Pro [40]) is connected to the beam while it supplies the drive signal of the circuit. Voltage amplification is achieved by the dynamic amplification $(Q_e)$ of the RLC circuit.

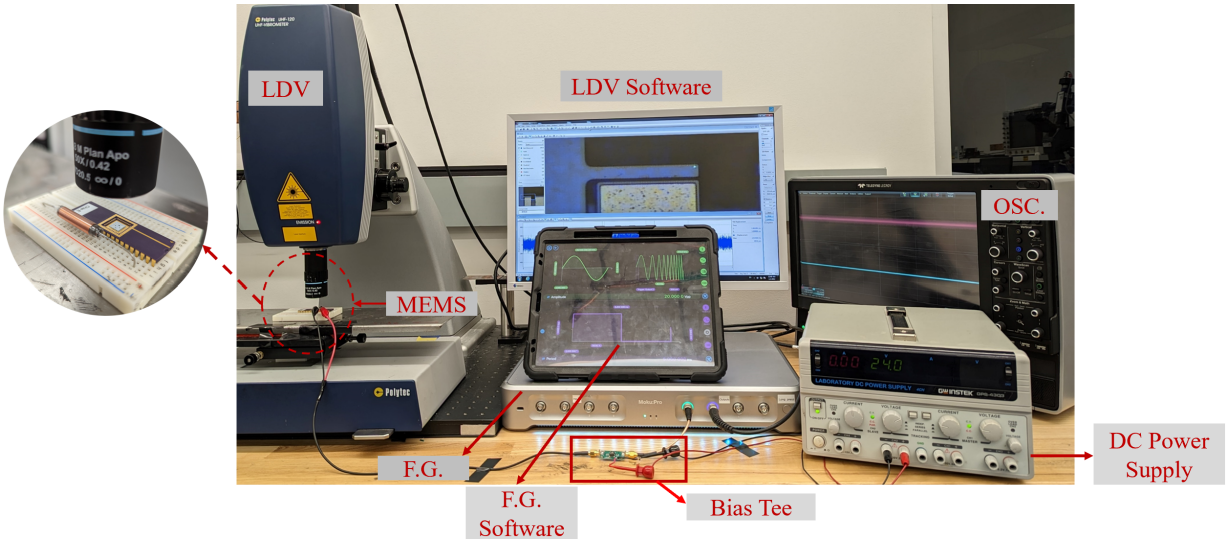
Figure 3.12(a) presents the experimental setup used to excite the actuator with unbiased signals, whereas Figure 3.12(b) depicts the setup used for biased signals. In the latter case, a bias tee and a DC power supply are introduced to the circuit.

### 3.3.3 Resonance Matching

The first technique employed was resonance matching. It calls for the use of a single tone signal designed to match the electrical resonance $f_e$ of the RLC circuit and to result in an electrostatic excitation force with a dominant in the frequency-domain peak that matches the mechanical resonance $f_m$ of the actuator. For unbiased signals, the external inductor $L$ is sized such that




(a)




(b)

Figure 3.12: (a) A schematic and (b) a picture of the experimental setups of unbiased and biased, respectively, resonant drive experiments.

$f_e \approx \frac{1}{2} f_m$ as per Eq. (3.1). For biased signals, the electrostatic force is described by

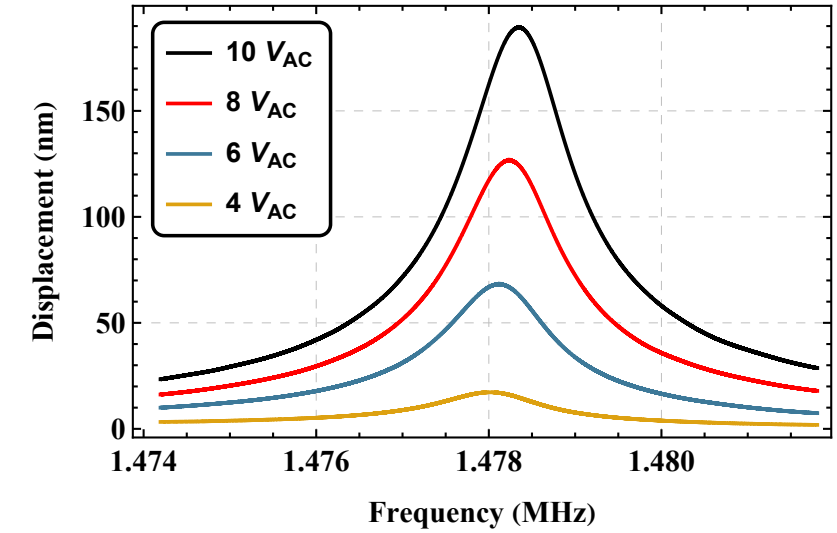
$$\begin{aligned} F_{es}(t) \propto \alpha V(t)^2 &= (V_{\mathrm{DC}} + V_{\mathrm{AC}} \cos(2\pi f t))^2 \\ &= V_{\mathrm{DC}}^2 + \frac{1}{2} V_{\mathrm{AC}}^2 + 2 V_{\mathrm{DC}} V_{\mathrm{AC}} \cos(2\pi f t) + \frac{1}{2} V_{\mathrm{AC}}^2 \cos(4\pi f t) \end{aligned} \tag{3.2}$$

Therefore, the external inductor $L$ is sized such that $f_e \approx f_m$.

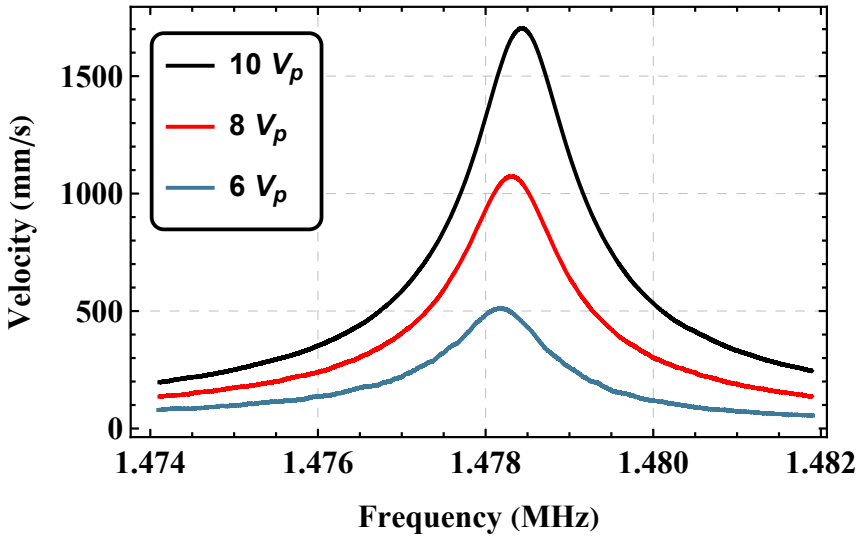
To excite actuator I with an unbiased signal, a $L = 2.2$ mH inductor was connected in series with the actuator resulting in a VNA-measured electrical resonance of $f_e = 780\,\text{kHz}$. It was found that the electrical natural frequency drops in the drive setup, Figure 3.12(a), due to uncharacterized reactive loading the function generator introduces into the circuit. Hence, the electrical natural frequency we intentionally set to a value larger than the desired signal frequency $f_e > f$. The signal frequency was swept within the range $f = [737 - 741]$ kHz in a time window of 100 ms while the voltage amplitude $V_{\text{AC}}$ was held constant.

The frequency response of actuator I is presented in Figure 3.13(a) for four values of the voltage amplitude. For a voltage amplitude of $V_{\text{AC}} = 10\,\text{V}$, this excitation scheme achieves a maximum displacement of $w_{\text{RMS}} = 189$ nm at resonance, which is more than twice the maximum displacement attained using a conventional voltage amplifier, Figure 3.4. The peak of the frequency-response curves was observed to shift to the right. Therefore, the experiment was repeated using a longer time window to investigate whether this shift was due to hardening of the resonator or an artifact of the sweep transients, see chapter 4. The tip velocity of actuator I was measured using the OFV-5000 LDV [43], and the data was collected by a digital oscilloscope in 4s-long time windows. The actuator velocity, Figure 3.13 (b), demonstrate a similar hardening behavior as the voltage amplitude is increased from $V_{\text{AC}} = 6\,\text{V}$ to $10\,\text{V}$ which confirms the presence of a hardening nonlinearity. Give the relatively small displacements involved, the source of this nonlinearity is probably the electrostatic field rather than the mechanical potential.

To investigate the effects of mistuning the electrical and mechanical resonances away from $f_e \approx \frac{1}{2} f_m$ on the resonance matching technique, we set the inductance of the external inductor to $L = 4$ mH. As a result, the VNA-measured electrical resonance was set to $f_e = 593\,\text{kHz}$ well below half of the mechanical resonance of actuator I at $\frac{1}{2} f_m = 739\,\text{kHz}$. Figure 3.14 shows the frequency-response curve of actuator I tip displacement under this excitation regime and a




(a)




(b)

Figure 3.13: The frequency-response curves of the beam tip (a) displacement and (b) velocity of actuator I connected in series with a 2.2 mH inductor under resonance matching excitation with three unbiased voltage amplitudes $V_{\mathrm{AC}}$.

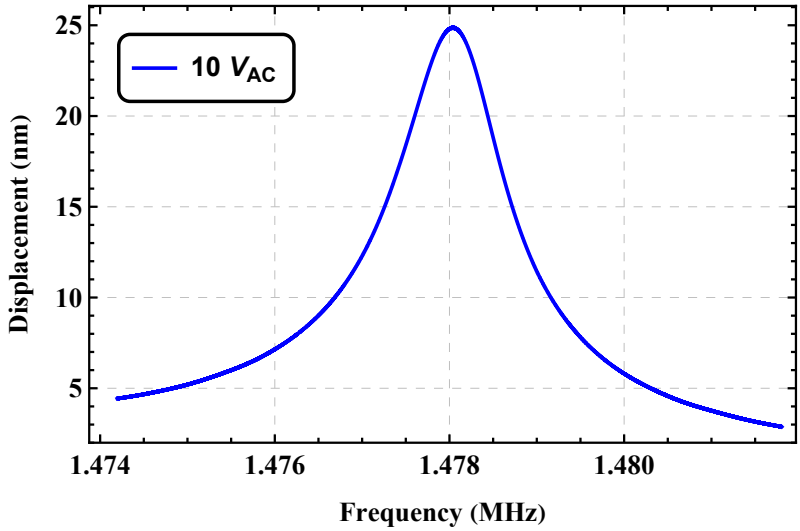



Figure 3.14: The frequency-response curve of actuator I tip displacement under a mistuned resonance matching excitation with an oversized inductor ($L = 4$ mH).

voltage amplitude of $V_{\mathrm{AC}} = 10$ V as the signal frequency was swept from $f = 737$ kHz to 741 kHz over a time window of 100 ms. The actuator displacement drops in this case, Figure 3.14, to $w_{\mathrm{RMS}} = 25$ nm which is much lower than the displacement obtained in the tuned case ($w_{\mathrm{RMS}} = 189$ nm).

Likewise, we set the inductance of the external inductor to $L = 950\,\mu$H resulting in a VNA-measured electrical resonance of $f_e = 1.405$ kHz, Figure 3.11(b), well above half of the mechanical resonance of actuator I. Figure 3.15 shows the frequency-response curve of actuator I tip velocity under a voltage amplitude of $V_{\mathrm{AC}} = 10$ V as the signal frequency swept in the range $f = [738.2 - 740]$ kHz over a time window of 30 ms. The tip velocity dropped to $V_{\mathrm{RMS}} = 9$ mm/s compared to $V_{\mathrm{RMS}} = 1.703$ m/s in the tuned case.

The experimental setup of Figure 3.12(b) was adopted for the biased resonance matching excitation of actuator I. The signal frequency was swept over the range of $f = [1.474 - 1.482]$ MHz in the vicinity of the mechanical resonant frequency $f_m$. An external inductor made of two

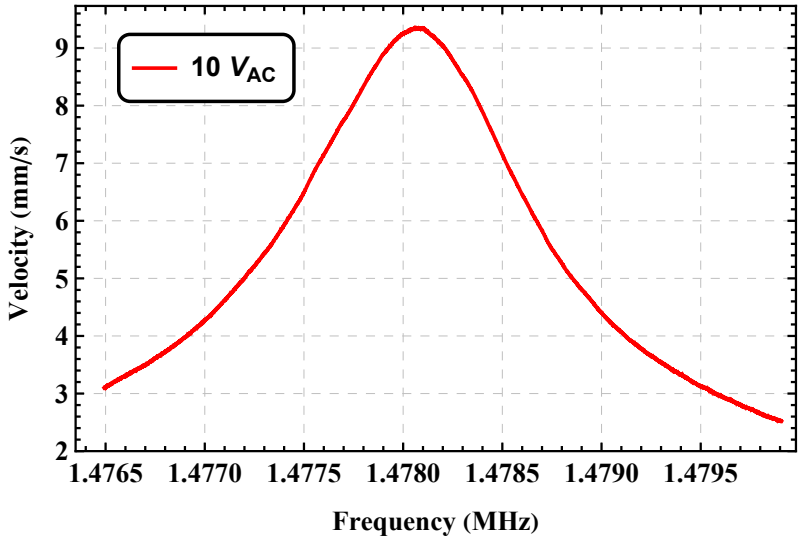



Figure 3.15: The frequency-response curve of actuator I velocity under a mistuned resonance matching excitation with an undersized inductor ($L = 950$ μH).

series inductors, $L_1 = 470$ μH and $L_2 = 27$ μH, was used to set the electric natural frequency to $f_e \approx f_m$. Figure 3.16 shows the frequency response of the actuator under three levels of bias voltage and the a voltage amplitude of $V_{\mathrm{AC}} = 10$ V. The maximum measured displacement $w_{\mathrm{RMS}} = 171.6$ nm was realized at resonance for a bias voltage of $V_{\mathrm{DC}} = 31.5$ V.

We note that the introduction of bias into the signal degrades the efficiency of the resonance matching technique. This can be seen in the fact that adding a bias voltage of $V_{\mathrm{DC}} = 31.5$ V to a harmonic signal (with $V_{\mathrm{AC}} = 10$ V) ends up reducing the realized displacement, in addition to incurring the cost and complexity of biasing the signal (compare the experimental setups in subfigures 3.12(a) and (b) and operating in a higher frequency range.

We investigated the impact of mistuning on resonance matching with biased signals. The experimental setup of Figure 3.12(a) was adopted in this case. First, a significantly oversized external inductor with $L = 950$ μH was introduced to the drive circuit, thereby mistuning the electrical resonance to the lower side of the mechanical resonance $f_e < f_m$. Figure 3.17 shows

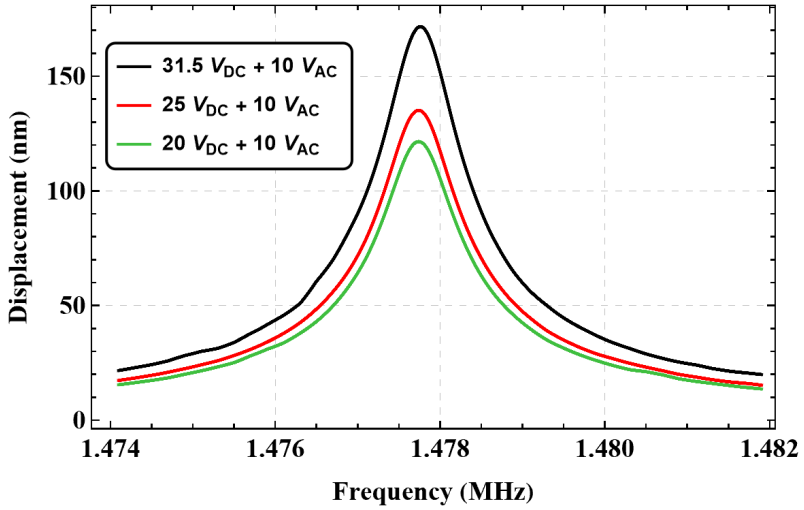



Figure 3.16: The frequency-response curves of actuator I tip displacement. The actuator is connected in series to two inductors, $L_1 = 470\,\mu$H and $L_2 = 27\,\mu$H, under actuation with three bias levels and a voltage amplitude of $V_{\rm AC} = 10$ V.

the measured frequency-response curve of actuator I′ tip displacement under resonance matching excitation with the voltage waveform $V_{AC} = V_{DC} = 5V$ as the signal is swept in the frequency range $f = [1.25 - 1.52]$ MHz over a time window of 200 ms. The electrical and mechanical resonances are mismatched with the former appearing at $f_e = 1.359$ MHz and the latter appearing at $f_m = 1.477$ MHz. Note that the VNA-measured electrical resonance was $f_e = 1.405$ MHz, Figure 3.11(b).

Second, we investigated the effects of using an undersized inductor on resonance matching of biased signals. In this case, the external inductor was undersized with an inductance of $L = 675\,\mu$H. Figure 3.18 shows the measured frequency-response curve of actuator I′ tip displacement under the same voltage waveform ($V_{\rm AC} = V_{\rm DC} = 5$ V) as the signal was swept in the frequency range $f = [1.45 - 1.59]$ MHz over a time window of 100 ms. Distinct peaks corresponding to the mismatched electrical and mechanical resonances appear in the frequency response with the electrical resonance at $f_e = 1.56$ MHz and the mechanical resonance at $f_m = 1.477$ MHz. Note

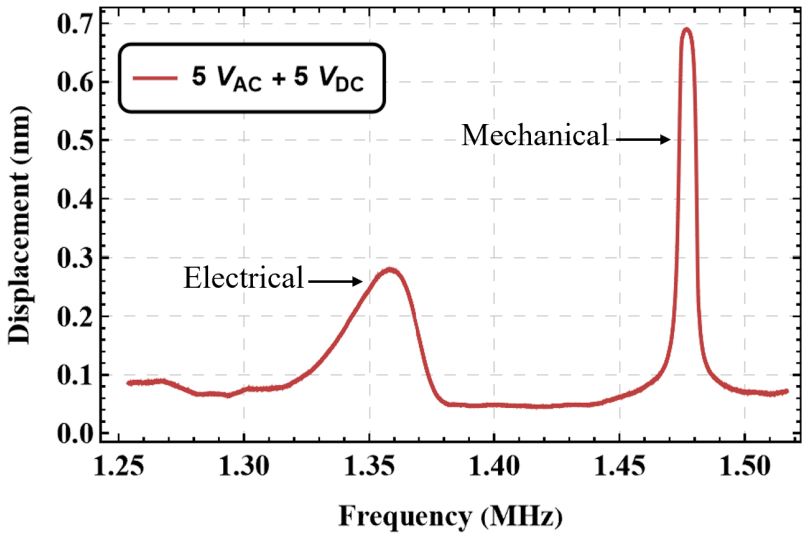



Figure 3.17: The frequency-response curve of actuator I′ tip displacement under a mistuned resonance matching excitation with an oversized inductor ($L = 950$ µH).

that the VNA-measured electrical resonance was $f_e = 1.62$ MHz, Figure 3.11(c). A bandpass filter with a frequency range of $[1.2 - 1.65]$ MHz was utilized to ensure that the observed peaks were not due to modal interactions or excitation of the in-plane mode at $f_{\text{in}} = 1.69$ kHz.

The two previous cases demonstrate that optical measurement of the MEMS response can serve as an indicator of the precise location of electrical resonance $f_e$. To accurately match the two resonances ($f_e = f_m$), the electrical resonance $f_e$ should be observed optically under a biased signal and adjusted iteratively until it merges with the mechanical resonance $f_m$ into a single peak. Note that when this technique is used to tune the two resonances for an unbiased signal, the response observed at $\frac{1}{2} f_m$ is the superharmonic rather than primary resonance.

We note that the undersized inductor in the last case, had an inductance larger than that of the matching inductor used for actuator I, Figure 3.16, $L = 497$ µH. The parasitic loading of the capacitor in the bias tee, of Figure 3.12 (b) experimental setup, accounts for this drop in the inductance required to match the electrical and mechanical resonances.

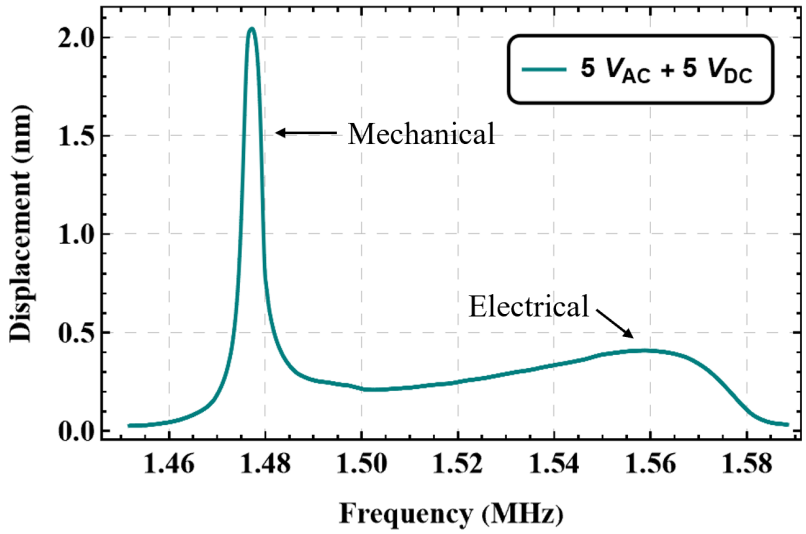



Figure 3.18: The frequency-response ccurve of actuator I′ tip displacement under a mistuned resonance matching excitation with an undersized inductor ($L = 675$ µH).

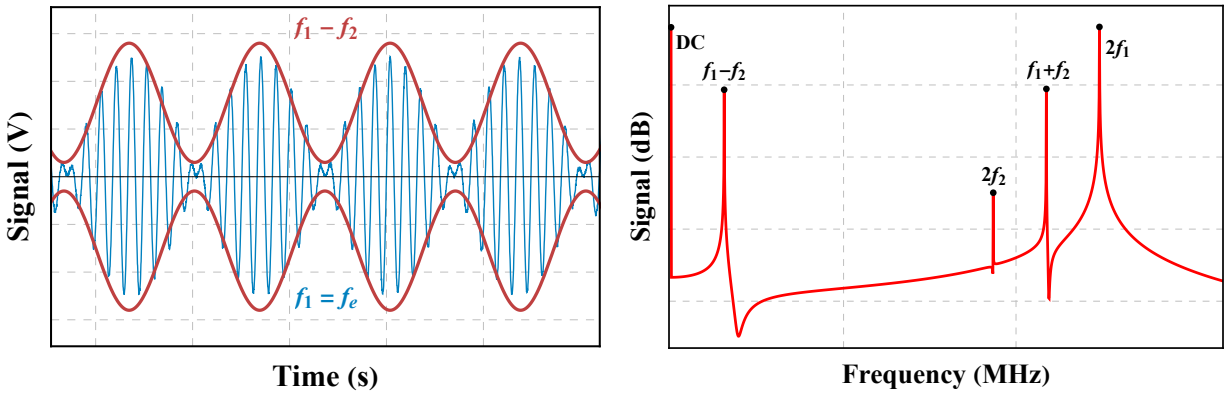
### 3.3.4 Multi-Frequency Excitation

The multi-frequency excitation technique utilizes the summation of two voltage signals resulting in an electrostatic force of the form

$$\begin{aligned} F_{es}(t) \propto \alpha V(t)^2 &= \alpha(V_{\mathrm{AC1}}\,\cos(2\pi f_1 t) + V_{\mathrm{AC2}}\,\cos(2\pi f_2 t))^2 \\ &= \frac{\alpha}{2}(V_{\mathrm{AC1}}^2 + V_{\mathrm{AC2}}^2) + \frac{\alpha}{2}\Big(V_{\mathrm{AC1}}^2\cos(4\pi f_1 t) + V_{\mathrm{AC2}}^2\cos(4\pi f_2 t)\Big) \\ &\quad + \alpha V_{\mathrm{AC1}}V_{\mathrm{AC2}}\Big(\cos\big(2\pi(f_1 - f_2)t\big) + \cos\big(2\pi(f_1 + f_2)t\big)\Big) \end{aligned} \tag{3.3}$$

The frequency of one signal is set equal to the electric resonance of the RLC circuit $f_1 \approx f_e$ while the sum or difference of the frequencies of the two signals is set equal to the mechanical resonance $f_1 \pm f_2 = f_m$ to drive the actuator with one of the last terms on the right hand-side of Eq. (3.3). Figure 3.19 shows the signal for the case of $f_1 > f_2$.

As noted in Subsection 3.3.3, it was found that the reactive loading of the function gener-




(a) (b)

Figure 3.19: Representations of the multi-frequency signal in (a) the time and (b) frequency domains.

ator in the drive setup, Figure 3.8(a), causes a drop in the electrical resonance away from that measured using the VNA. To address that, a two-step process was developed to determine the electrical resonance $f_e$. First, an estimate of the electrical resonance $\hat{f}_e$ was obtained using the VNA and the setup of Figure 3.8(a) to measure the electrical resonance. Then the drive setup, Figure 3.12(a), was used to vary the first signal frequency $f_1$ in the vicinity of $\hat{f}_e$ while measuring the response of the actuator. The electrical resonance $f_e$ was determined as the first signal frequency $f_1$ at peak response.

First, we tested the use of a higher electric resonance $(f_e > f_m)$ in multi-frequency excitation which corresponds to driving the actuator via the electrostatic force of the frequency difference $(f_1 - f_2)$. Actuator I′ was connected in series to an external inductor with $L_1 = 60$ µH resulting in an estimated electrical resonance of $\hat{f}_e = 6.8$ MHz, Figure 3.10(a). Based on that, the electrical resonance was found to be $f_e = 6.27$ MHz using the search routine described above. The frequency of the first signal was set to match the electrical resonance frequency $f_1 = f_e$. The frequency of the second signal was swept-down in the range $f_2 = [4.797 - 4.789]$ MHz over 100 ms, so that the difference between the two frequencies is swept-up in the vicinity of the

mechanical natural frequency $f_1 - f_2 = [1.473 - 1.481]$ MHz.

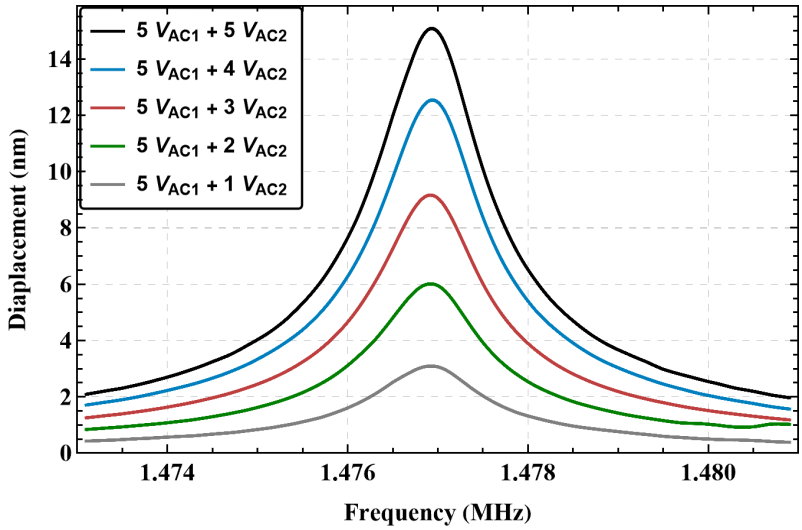



Figure 3.20: The frequency response of actuator I′ tip displacement under multi-frequency excitation ($f_e = 6.27$ MHz).

Figure 3.20 shows the frequency-response curves of actuator I′ tip displacement under five levels of the second signal voltage amplitude $V_{\mathrm{AC2}}$ while the amplitude of the amplifier (first) signal is held constant at $V_{\mathrm{AC1}} = 5$ V. The maximum displacement realized was $w_{\mathrm{RMS}} = 15$ nm observed at resonance under a voltage amplitude of $V_{\mathrm{AC2}} = 5$ V, which is 0.75% of the air gap. The response under this excitation scheme is well regulated as the second signal amplitude is varied.

To test the flexibility of this technique, we tuned the the electrical resonance to a higher value by using a smaller external inductor with $L_2 = 10\,\mu$H. As a result, the estimated electrical resonance increased to $\hat{f}_e = 14.4$ MHz, Figure 3.10(b). The electrical resonance was found to be $f_e = 13.25$ MHz using the drive setup. The first signal frequency was set equal to it $f_1 = f_e$ while the second signal frequency was swept-down in the range $f_2 = [11.777 - 11.769]$ MHz over 100 ms. Figure 3.21 shows the frequency response of actuator I′ under a fixed amplifier voltage

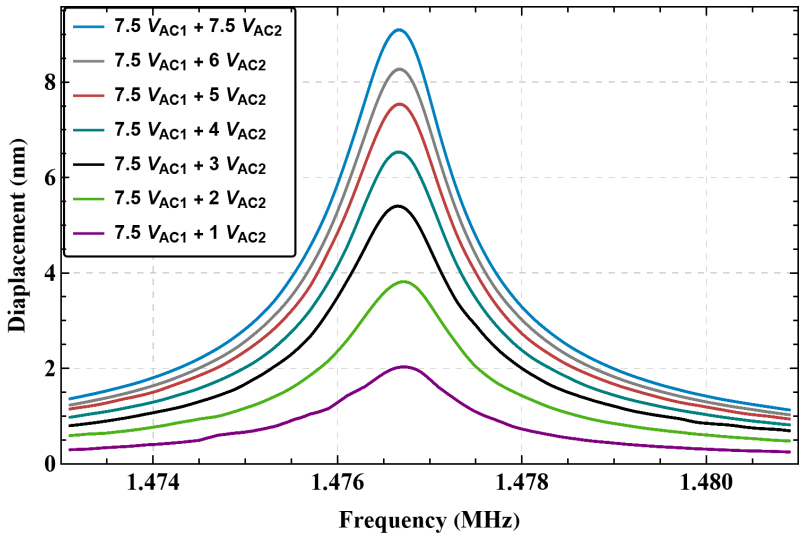



Figure 3.21: The frequency response of actuator I′ tip displacement under multi-frequency excitation ($f_e = 13.25$ MHz).

amplitude $V_{\mathrm{AC1}} = 7.5\,\mathrm{V}$ and seven levels of the second signal voltage amplitude $V_{\mathrm{AC2}}$. The maximum measured displacement with this inductor was $w_{\mathrm{RMS}} = 9$ nm for a voltage amplitude of $V_{\mathrm{AC2}} = 7.5$ V, corresponding to 0.45% of the air gap.

The drop in displacement with the increase in the amplifier signal voltage from $V_{\mathrm{AC1}} = 5\,\mathrm{V}$ to 7.5 V and the actuation signal voltage from $V_{\mathrm{AC2}} = 5\,\mathrm{V}$ to 7.5 V is an interesting finding. It is even more so given that the smaller inductor $L_2$ in the second case imposes lower losses on the RLC circuit, due to a smaller equivalent series resistance (ESR), than the inductor $L_1$ of the first case. We postulate that the ESR of both inductors are negligible compared to the overall resistance of the circuit. On the other hand, the larger inductor $L_1$ results in a better electrical quality factor than the smaller inductor $L_2$ given that:

$$Q_e = \frac{1}{R}\sqrt{\frac{L}{C}}$$

thereby making for a better amplifier circuit.

We applied the same excitation technique to actuator II to verify the scheme repeatability. An external inductor $L_1 = 60\,\mu\text{H}$ was connected in series with the actuator resulting in an electrical resonance of $f_e = 6.21$ MHz. The frequency of the amplifier signal was set to match the electrical resonance $f_1 = f_e$. The frequency of the second signal was swept-down in the range $f_2 = [4.674 - 4.664]$ MHz over 100 ms, so that the difference between the two frequencies is swept-up in the vicinity of the mechanical natural frequency $f_1 - f_2 = [1.536 - 1.546]$ MHz.

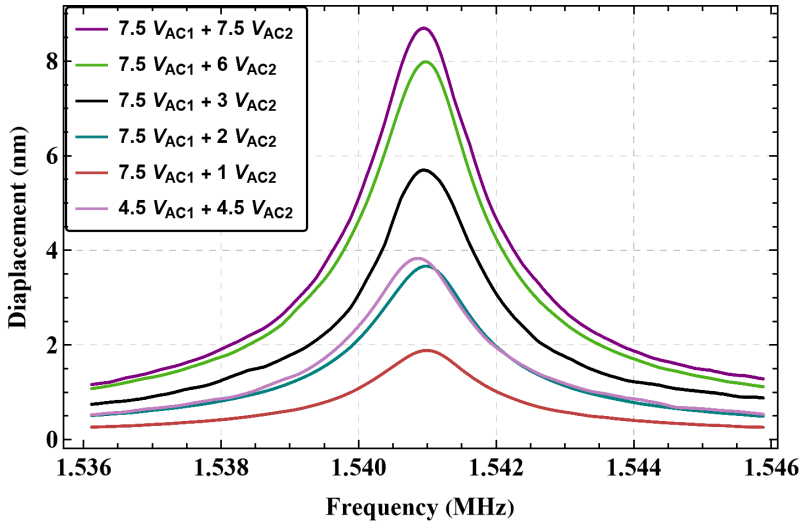



Figure 3.22: The frequency response of actuator II tip displacement under multi-frequency excitation ($f_e = 6.21$ MHz).

Figure 3.22 shows the frequency response of actuator II under a fixed amplifier voltage amplitude $V_{\text{AC1}} = 7.5\,\text{V}$ and five levels of second signal voltage amplitude $V_{\text{AC2}}$. The largest realized displacement with this inductor was $w_{\text{RMS}} = 8.7$ nm for a voltage amplitude of $V_{\text{AC2}} = 7.5$ V, corresponding to 0.435% of the air gap. For comparison, the figure also incorporates a frequency-response curve with a lower amplifier voltage amplitude of $V_{\text{AC1}} = 4.5\,\text{V}$ and an actuation voltage amplitude of $V_{\text{AC2}} = 4.5\,\text{V}$. It can be seen that the response in the latter case is comparable

to that of the higher amplifier voltage under a much smaller actuation voltage of $V_{\mathrm{AC2}} = 2\,\mathrm{V}$, thereby demonstrating the efficacy of the amplifier circuit.

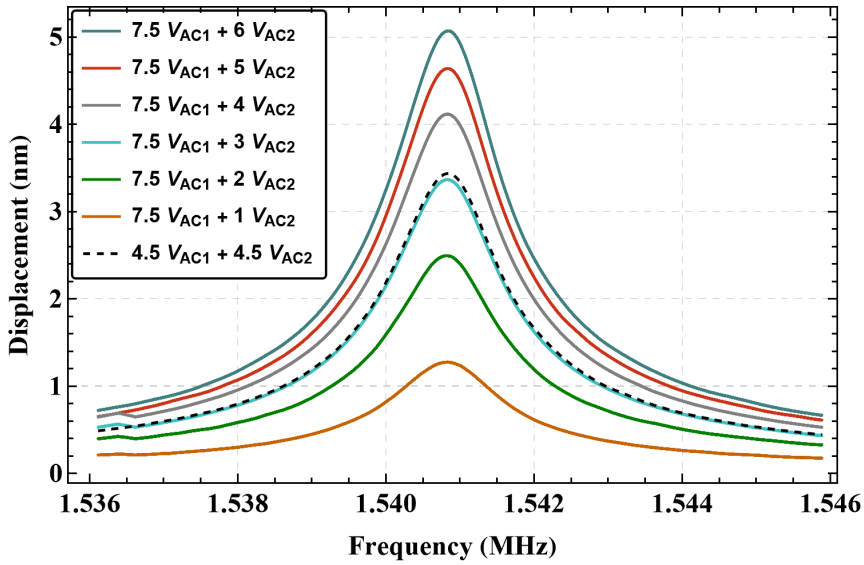



Figure 3.23: The frequency response of actuator II tip displacement under multi-frequency excitation ($f_e = 13.5$ MHz).

A smaller external inductor $L_2 = 10$ µH was also used in conjunction with actuator II resulting in an electrical resonance frequency of $f_e = 13.5$ MHz. The first signal frequency was set equal to it $f_1 = f_e$ while the second signal frequency was swept-down in the range $f_2 = [11.964 - 11.954]$ over 100 ms. Figure 3.23 shows the frequency response of actuator II tip displacement under seven levels of the second signal voltage amplitude while the amplitude of the first amplifier signal was held constant $V_{\mathrm{AC1}} = 7.5\,\mathrm{V}$. The maximum measured tip displacement was $w_{\mathrm{RMS}} = 5.1$ nm for a voltage amplitude of $V_{\mathrm{AC2}} = 6\,\mathrm{V}$, corresponding to 0.255% of the air gap.

Similar to the case of actuator I′, the realized tip displacement using the larger $L_1$ inductor is greater than that observed with the smaller $L_2$ inductor, thus confirming our earlier hypothesis. Figure 3.23 also incorporates a frequency-response curve with a lower amplifier voltage ampli-

tude of $V_{\mathrm{AC1}} = 4.5\,\mathrm{V}$ and an actuation voltage amplitude of $V_{\mathrm{AC2}} = 4.5\,\mathrm{V}$. It can be seen that the response in this case is comparable to that of the higher amplifier voltage under a smaller actuation voltage of $V_{\mathrm{AC2}} = 3\,\mathrm{V}$, which confirms the efficacy of the amplifier circuit.

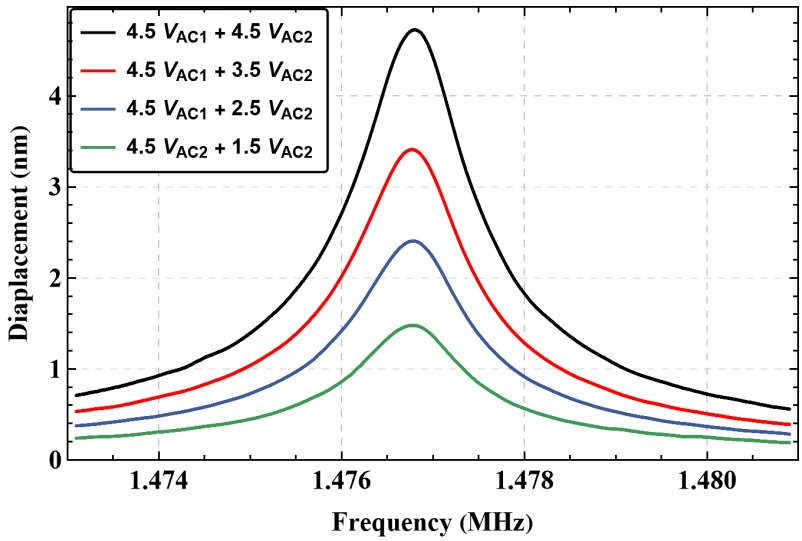



Figure 3.24: The frequency response of actuator I′ tip displacement under multi-frequency excitation ($f_e = 528$ kHz).

Next, we tested the use of a lower electric resonance ($f_e < f_m$) to drive the actuator via the electrostatic force of the frequency sum ($f_1 + f_2$). Actuator I′ was connected in series to a large inductor, made of two series connected individual inductors $L_3 = 3.2$ mH and $L_4 = 2.4$ mH, resulting in an estimated electrical resonance of $\hat{f}_e = 570$ kHz, Figure 3.11(a). The electrical resonance was found to be $f_e = 528$ kHz using the drive setup. The first signal frequency was set equal to the electrical resonance $f_1 = f_e$ while the second signal frequency was swept-up in the range $f_2 = [945 - 953]$ kHz over 100 ms, so that the frequency sum is swept past the mechanical resonance $f_m$ in the range $f_1 + f_2 = [1.473 - 1.481]$.

The frequency-response curves of actuator I′ tip displacement are shown in Figure 3.24 for four values of the second signal voltage amplitude $V_{\mathrm{AC2}}$ while the amplifier voltage amplitude is

held constant at $V_{\mathrm{AC1}} = 4.5$ V. The largest displacement in this case was $w_{\mathrm{RMS}} = 5.1$ nm realized at resonance for a voltage amplitude of $V_{\mathrm{AC2}} = 4.5$, corresponding to 0.255% of the air gap.

Electrical characterization shows that the measured electrical quality factor $Q_e$, see subsection 3.3.1, increases for larger inductors since the ESR of the inductor is negligible compared to the parasitic resistance of the circuit. However, we found that the displacement of actuator I′ when driven by the electrostatic force of the frequency sum $(f_1 + f_2)$ was smaller than that realized above under excitation with the frequency difference $(f_1 - f_2)$ force. We postulate that the reason for this dropped response is due to losses due to the loss tangent of the parasitic capacitor which is dominate when $f_1$ is set to low values.

### 3.3.5 Amplitude Modulation

In this excitation scheme, we utilize an amplitude-modulated signal resulting in an electrostatic force of the form

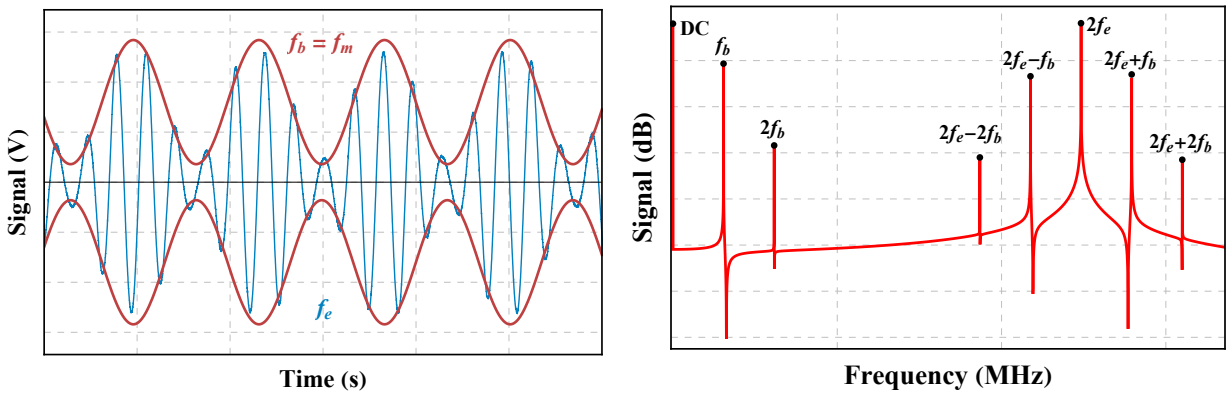
$$\begin{aligned} F_{es}(t) \propto \alpha V(t)^2 &= \alpha\big(V_{\mathrm{AC1}} + V_{\mathrm{AC2}}\,\cos(2\pi f_b t)\big)^2 \cos^2(2\pi f_e t) \\ &= \frac{\alpha}{4}(2V_{\mathrm{AC1}}^2 + V_{\mathrm{AC2}}^2) + \frac{\alpha}{4}(2V_{\mathrm{AC1}}^2 + V_{\mathrm{AC2}}^2)\,\cos(4\pi f_e t) \\ &\quad + \frac{\alpha}{2} V_{\mathrm{AC1}} V_{\mathrm{AC2}} \Big( \cos\big(2\pi(2f_e - f_b)t\big) + \cos\big(2\pi(2f_e + f_b)t\big)\Big) \\ &\quad + \frac{\alpha}{8} V_{\mathrm{AC2}}^2 \Big( \cos\big(4\pi(f_e - f_b)t\big) + \cos\big(4\pi(f_e + f_b)t\big)\Big) \\ &\quad + \alpha\, V_{\mathrm{AC1}} V_{\mathrm{AC2}}\,\cos(2\pi f_b t) + \frac{\alpha}{4} V_{\mathrm{AC2}}^2\,\cos(4\pi f_b t) \end{aligned} \tag{3.4}$$

The drive signal, shown in Figure 3.25, is the product of an RF carrier signal with a frequency $f_e$ and a baseband signal with a frequency $f_b$. Given that $f_e$ is, by definition, much larger than $f_b$, the actuator acts as a low-pass filter, thereby attenuating the higher frequency forces at $2f_e$, $2f_e \pm f_b$, and $2f_e \pm 2f_b$. To guarantee that, the RF carrier frequency $f_e$ is typically set in the range

of 3–100 $f_m$ [35]. On the other hand, the actuator follows the electrostatic force generated by the envelope of the signal. Provided that we set $V_{\mathrm{AC1}} > V_{\mathrm{AC2}}$, the force at $f_b$, which is proportional to $(V_{\mathrm{AC1}}V_{\mathrm{AC2}})$ per Eq. (3.4), can be used as the dominant excitation force. The ratio between the two amplitudes

$$\mu = \frac{V_{\mathrm{AC2}}}{V_{\mathrm{AC1}}}$$

is the signal modulation index.




(a) (b)

Figure 3.25: Representations of the amplitude-modulated signal in (a) the time and (b) frequency domains . $f_e$ is the carrier frequency and $f_b$ is the baseband frequency.

The RLC circuit was tuned to set the electrical resonance frequency higher than that of the actuator $f_e > f_m$ using a small external inductor $L_1 = 60$ µH connected in series with actuator I′. The resulting electrical resonance was measured as $f_e = 6.27$ MHz using the technique described in Subsection 3.3.4. The carrier signal frequency was set to match the electrical resonance $f_e$, while the frequency of the baseband signal was swept-up past the mechanical resonance $f_m$ in the range $f_b = [1.473 - 1.481]$ over 100 ms.

Figure 3.26 shows the frequency response of actuator I′ tip displacement under six levels of the second voltage amplitude $V_{\mathrm{AC2}}$ while the amplitude of the first (amplifier) signal is held

constant at $V_{\mathrm{AC1}} = 7.5$ V. The maximum displacement realized was $w_{\mathrm{RMS}} = 19.8$ nm observed at resonance $f_m = 1.477$ MHz under a second voltage amplitude of $V_{\mathrm{AC2}} = 7.5$ V (a modulation index of $\mu = 1$), which is 0.99% of the air gap.

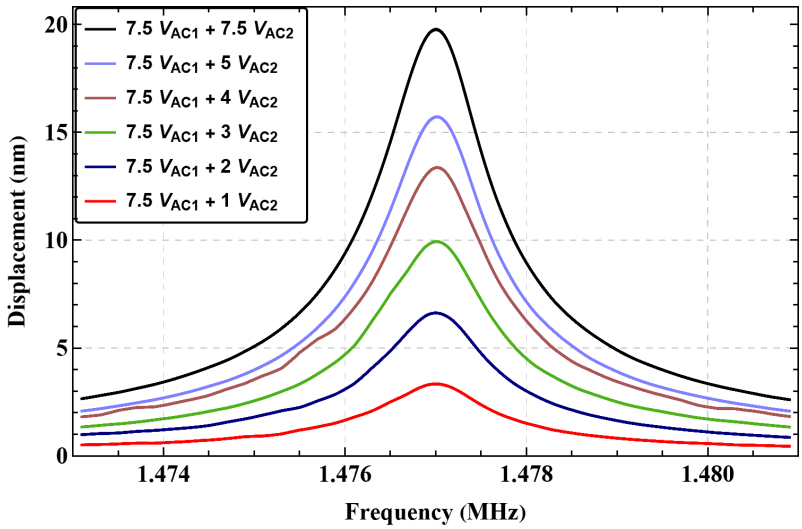



Figure 3.26: The frequency response of actuator I′ tip displacement under excitation with an amplitude-modulated signal where the carrier frequency is set to $f_e = 6.27$ MHz.

To test the flexibility of this technique, we tuned the the electrical resonance to a higher value by using a smaller external inductor $L_2 = 27$ µH. As a result the electrical resonance increased to $f_e = 9.11$ MHz. Figure 3.27 shows the frequency response of actuator I′ under four levels of the second voltage amplitude $V_{\mathrm{AC2}}$ while the amplifier signal amplitude is held constant at $V_{\mathrm{AC1}} = 7.5$ V. The maximum measured displacement was $w_{\mathrm{RMS}} = 9.2$ nm for a voltage amplitude of $V_{\mathrm{AC2}} = 7.5$ V, corresponding to 0.46% of the air gap.

A third inductor $L_3 = 10$ µH was also used with actuator I′ to set the electrical resonance to $f_e = 13.25$ MHz. Figure 3.28 shows the frequency response of actuator I′ under seven levels of the second signal voltage amplitude $V_{\mathrm{AC2}}$ while the amplifier signal amplitude is held constant at $V_{\mathrm{AC1}} = 7.5$ V. The maximum measured displacement was $w_{\mathrm{RMS}} = 9.3$ nm for a voltage

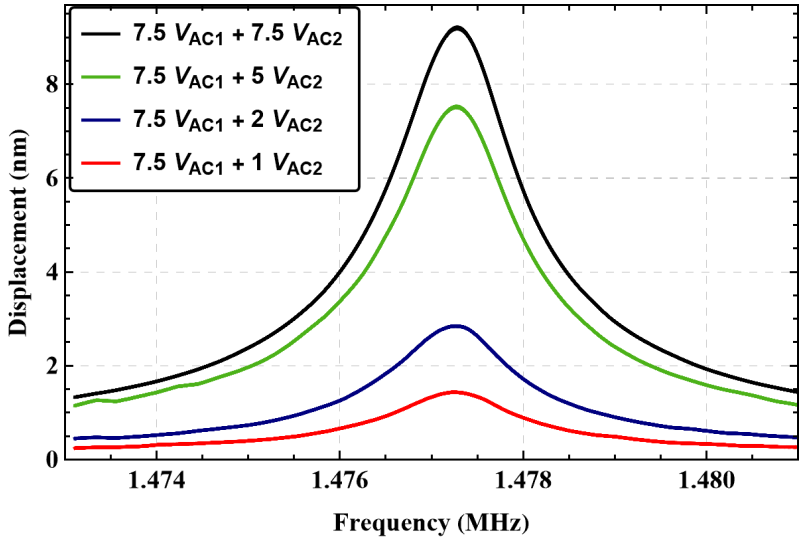



Figure 3.27: The frequency response of actuator I′ tip displacement under excitation with an amplitude-modulated signal where the carrier frequency is set to $f_e = 9.11$ MHz.

amplitude of $V_{\mathrm{AC2}} = 7.5$ V, corresponding to 0.47% of the air gap. The smaller displacements realized in the last two cases compared to the case of the first case, with the larger $L_1$ inductor, confirms our hypothesis above that the ESR of inductors at μH level is negligible compared to the other circuit losses which allows the larger inductance of $L_1$ to improve the overall circuit quality factor $Q_e$.

We applied the same excitation technique to actuator II to verify the scheme repeatability. An external inductor $L_1 = 60$ μH was connected in series with the actuator resulting in an electrical resonance at $f_e = 6.21$ MHz. The difference between the electrical resonance in this case and that in actuator I′ case is due to inter-inductor variability and variations in the circuit wiring. The baseband signal frequency was swept-up in the range $f_b = [1.536 - 1.546]$ MHz. Figure 3.29 shows the frequency-response curves under eight levels of the second voltage amplitude $V_{\mathrm{AC2}}$. The maximum tip displacement achieved was $w_{\mathrm{RMS}} = 7.9$ nm at resonance $f_m = 1.5408$ MHz for a second voltage amplitude of $V_{\mathrm{AC2}} = 7.5$ V, which is 0.395% of the air gap.

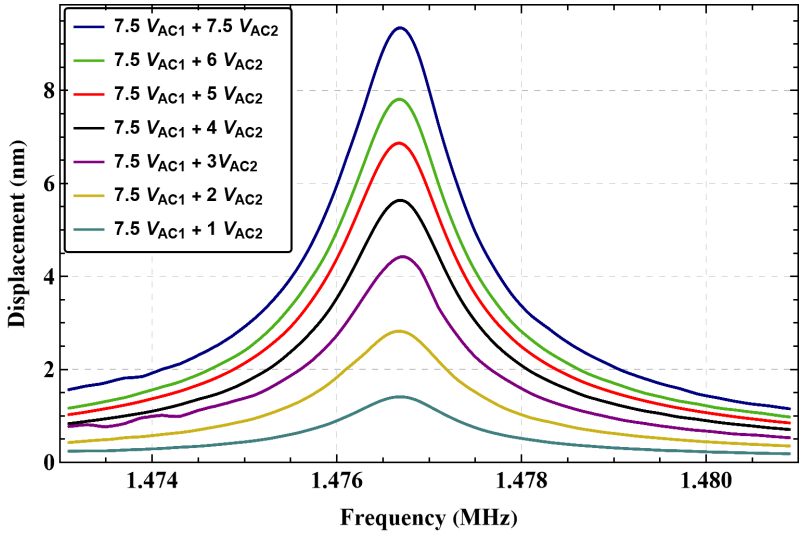



Figure 3.28: The frequency response of actuator I′ tip displacement under excitation with an amplitude-modulated signal where the carrier frequency is set to $f_e = 13.25$ MHz.

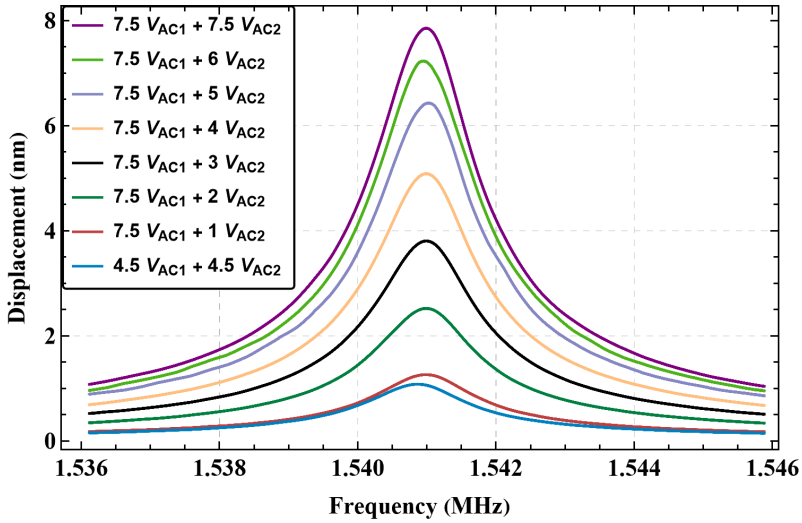



Figure 3.29: The frequency response of actuator II tip displacement under excitation with an amplitude-modulated signal where the carrier frequency is set to $f_e = 6.21$ MHz.

For comparison, the figure also incorporates a frequency-response curve with a lower amplifier voltage amplitude of $V_{\mathrm{AC1}} = 4.5\,\mathrm{V}$ and a second voltage amplitude of $V_{\mathrm{AC2}} = 4.5\,\mathrm{V}$. It can

be seen that the response in the latter case is comparable to that of the higher amplifier voltage under a much smaller second voltage of $V_{\mathrm{AC2}} = 1\,\mathrm{V}$, thereby demonstrating the efficacy of the amplifier circuit.

The smaller $L_3 = 10$ µH inductor was connected in series with actuator II resulting in an electrical resonance of $f_e = 13.1$ MHz. Figure 3.30 shows the frequency-response curves of the tip displacement for seven levels of the second voltage amplitude $V_{\mathrm{AC2}}$. The largest measured RMS displacement was $w_{\mathrm{RMS}} = 4.5$ nm at resonance for the second voltage amplitude of $V_{\mathrm{AC2}} = 7.5$ V, corresponding to 0.23% of the air gap. The results also confirm that larger inductors $(L_1)$ result in higher amplification (larger $Q_e$) for µH sized inductors.

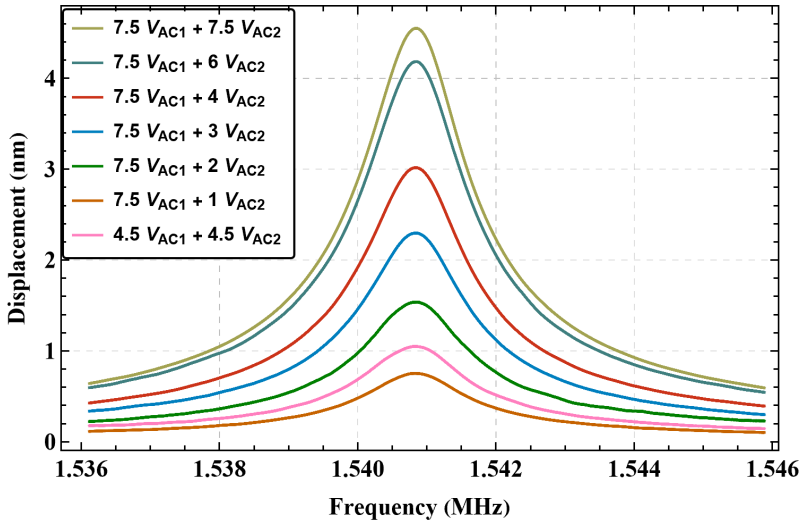



Figure 3.30: The frequency response of actuator II tip displacement under excitation with an amplitude-modulated signal where the carrier frequency is set to $f_e = 13.1$ MHz.

Figure 3.30 also incorporates a frequency-response curve with a lower amplifier voltage amplitude of $V_{\mathrm{AC1}} = 4.5\,\mathrm{V}$ and a second voltage amplitude of $V_{\mathrm{AC2}} = 4.5\,\mathrm{V}$. It can be seen that the response in this case falls between those for the smaller voltage amplitudes $V_{\mathrm{AC2}} = 1$ and $2\,\mathrm{V}$ and the higher amplifier voltage $V_{\mathrm{AC2}} = 7.5\,\mathrm{V}$, further confirming the efficacy of the amplifier

circuit.

## 3.4 Model Validation

Assuming the dominance of linear viscous damping mechanisms and that the mechanical and electrical resonators are dynamically uncoupled, the actuators' quality factors $Q_m$ were determined as the average of the quality factors measured from the frequency-response curves obtained for each actuator under all attempted actuation techniques and excitation levels. The measured quality factors and their averages for actuators I, I′, and II are listed in Tables 3.1, 3.2, and 3.3 with standard deviations of 0.54%, 3.75%, and 3.39%, respectively.

Table 3.1: The measured quality factors of Actuator I.

| Technique | $V_{\mathrm{AC}}$ (V) | $Q_m$ | $f_m$ (MHz) |
|---|---|---|---|
| Voltage Amplifier | 60 | 1325.11 | 1.47803 |
| | 90 | 1328.02 | 1.47808 |
| | 105 | 1332.11 | 1.47810 |
| | 114 | 1337.19 | 1.47810 |
| Resonance Matching (unbiased) | 4 | 1312.62 | 1.478013 |
| | 6 | 1330.68 | 1.47812 |
| | 8 | 1329.59 | 1.47824 |
| | 10 | 1324.45 | 1.47835 |
| $(Q_m)_{\mathrm{Avg}} \pm \sigma$ | | 1327.47 $\pm$ 7.23 | |

Table 3.2: The measured quality factors of Actuator I′.

| Technique | $V_{\mathrm{AC}}$ (V) | $Q_m$ | $f_m$ (MHz) |
|---|---|---|---|
| Voltage Amplifier | 15 | 1366.61 | 1.476619 |
| | 18 | 1362.7 | 1.476623 |
| | 21 | 1336.05 | 1.476601 |
| | 24 | 1393.16 | 1.476606 |
| | 39 | 1424.64 | 1.476637 |
| | 45 | 1384.95 | 1.476630 |
| | 51 | 1392.39 | 1.476634 |
| | 99 | 1329.17 | 1.476713 |
| | 102 | 1321.33 | 1.476722 |
| | 105 | 1312.18 | 1.476728 |
| | 108 | 1380.13 | 1.476735 |
| Multi-Frequency (60 µH) | $V_{\mathrm{AC2}}$ (V) | $Q_m$ | $f_m$ (MHz) |
| | 1 | 1366.14 | 1.476934 |
| | 2 | 1393.19 | 1.476918 |
| | 3 | 1402.98 | 1.476916 |
| | 4 | 1403.14 | 1.47694 |
| | 5 | 1376.32 | 1.476933 |
| Multi-Frequency (10 µH) | 1 | 1340.64 | 1.476713 |
| | 2 | 1372.16 | 1.476718 |
| | 3 | 1372.48 | 1.476655 |
| | 4 | 1377.10 | 1.476664 |
| | 5 | 1370.84 | 1.476673 |

| | | | |
|---|---|---|---|
| | 6 | 1365.14 | 1.476671 |
| | 7.5 | 1370.59 | 1.476668 |
| Multi-Frequency (5.6 mH) | 1.5 | 1377.71 | 1.476767 |
| | 2.5 | 1369.04 | 1.476782 |
| | 3.5 | 1367.51 | 1.476771 |
| | 4.5 | 1384.07 | 1.476806 |
| AM (60 µH) | 1 | 1375.50 | 1.477012 |
| | 2 | 1392.08 | 1.476999 |
| | 3 | 1339.21 | 1.477012 |
| | 4 | 1387.91 | 1.477013 |
| | 5 | 1413.28 | 1.477017 |
| | 7.5 | 1400.40 | 1.477005 |
| AM (27 µH) | 1 | 1212.75 | 1.477255 |
| | 2 | 1238.49 | 1.477267 |
| | 5 | 1221.69 | 1.477268 |
| | 7.5 | 1219.58 | 1.477280 |
| AM (10 µH) | 1 | 1364.28 | 1.476695 |
| | 2 | 1348.81 | 1.476676 |
| | 3 | 1452.17 | 1.476712 |
| | 4 | 1367.93 | 1.476685 |
| | 5 | 1374.55 | 1476.675 |
| | 6 | 1384.99 | 1.476678 |
| | 7.5 | 1361.51 | 1.476689 |
| $(Q_m)_{\text{Avg}} \pm \sigma$ | | 1360.62 $\pm$ 51.00 | |

Table 3.3: The measured quality factors of Actuator II.

| Technique | $V_{\mathrm{AC}}$ (V) | $Q_m$ | $f_m$ (MHz) |
|---|---|---|---|
| Function Generator | 8 | 1043.00 | |
| | 10 | 1080.00 | |
| Voltage Amplifier | 15 | 1068.70 | 1.54081 |
| | 21 | 1084.04 | |
| | 30 | 1185.82 | |
| | 33 | 1086.00 | |
| | 39 | 1076.90 | |
| | 44 | 1094 | |
| | 48 | 1092.70 | |
| | 57 | 1096.20 | |
| Multi-Frequency (60 μH) | $V_{\mathrm{AC2}}$ (V) | $Q_m$ | $f_m$ (MHz) |
| | 1 | 1142.66 | 1.54095 |
| | 2 | 1139.36 | |
| | 3 | 1185.9 | |
| | 6 | 1155.76 | |
| | 7.5 | 1117.93 | |
| Multi-Frequency (10 μH) | 1 | 1135.39 | 1.54084 |
| | 2 | 1168.44 | |
| | 3 | 1149.87 | |
| | 4 | 1151.25 | |
| | 5 | 1152.97 | |
| | 6 | 1144.33 | |

| | | | |
|---|---|---|---|
| AM (60 μH) | 1 | 1135.16 | 1.54099 |
| | 2 | 1140.29 | |
| | 3 | 1152.06 | |
| | 4 | 1154.48 | |
| | 5 | 1172.77 | |
| | 6 | 1142.88 | |
| | 7.5 | 1150.42 | |
| AM (10 μH) | 1 | 1140.85 | 1.54084 |
| | 2 | 1132.07 | |
| | 3 | 1146.88 | |
| | 4 | 1145.35 | |
| | 5 | 1196.23 | |
| | 6 | 1143.58 | |
| | 7.5 | 1148.77 | |
| $(Q_m)_{\text{Avg}} \pm \sigma$ | | 1129.34 $\pm$ 38.27 | |

Actuation using a biased voltage signal in the resonance matching technique was attempted only using actuator I. The average measured quality factor $Q_m$ in this case, Table 3.4, is larger by more than 20% that for conventional actuation or resonance matching with an unbiased signal, Table 3.1. The similar ranges of motion of the biased and unbiased voltage signals and the unchanged natural frequency in all cases, rule out a change in the dissipation process in the mechanical resonator between the biased and unbiased cases. The 'apparent' change in $Q_m$ in the case of biased signals is an indication that the combination of the quadratic electrostatic nonlinearity and the electrostatic force at the second harmonic $(2f_e)$ in the in-plane direction are large enough to activate principal parametric resonance. Further the ratio of the force amplitude

driving primary resonance in the biased to the unbiased cases is $\frac{4V_{\mathrm{DC}}}{Q_e V_{\mathrm{AC}}}$, as per Eq. (3.5), which corresponds to the range of 0.4–0.625. This suggest that the dominant contributor to the response in the biased signal case is parametric rather than primary resonance and therefore the $Q_m$ measured in Table 3.4 representing the elevated quality factor available under parametric excitation due to noise squeeze [46].

Table 3.4: The measured quality factors of Actuator I.

| Technique | $V_{\mathrm{AC}}$ (V) | $V_{\mathrm{DC}}$ (V) | $Q_m$ | $f_m$ (MHz) |
|---|---|---|---|---|
| Resonance Matching (biased) | 10 | 31.5 | 1619.46 | 1.47776 |
| | | 25 | 1613.78 | |
| | | 20 | 1627.29 | |
| $(Q_m)_{\mathrm{Avg}}$ | | | 1620.18 | |

The model was calibrated to determine the fringing field correction factor $\kappa$ for each actuator by matching its measured peak response under conventional actuation to the model results. Using the response at resonance for unbiased voltage amplitudes of $V_{\mathrm{AC}} = 114\,\mathrm{V}$ and 57 V, the correction factors for actuators I and II were found to be $\kappa = 0.0145$ and $\kappa = 0.0088$, respectively.

The frequency response for actuators I and II under conventional excitation was simulated by numerically integrating Eq. (2.22) where the voltage signal $V(t)$ generated by the function generator alone ($V_{\mathrm{AC}} \leq 10\,\mathrm{V}$) or in combination with the voltage amplifier ($V_{\mathrm{AC}} > 10\,\mathrm{V}$) is described by Eq. (3.2). The bias voltage was set to $V_{\mathrm{DC}} = 0$, the excitation frequency was set to the lower end of the frequency range, and integration was carried out for $5 \times 10^4$ nondimensional time units starting from initial conditions corresponding to the static equilibrium $w(0) = w_s$ and $\dot{w}(0) = 0$. The RMS of the displacement was obtained over the last 6,000 nondimensional time units. The excitation frequency was increased in small steps to obtain the frequency-response

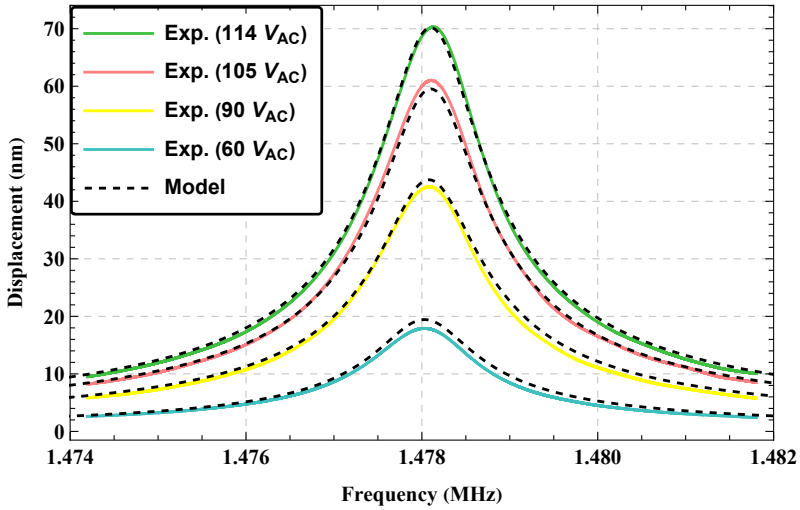



Figure 3.31: Comparison between the experimental (solid lines) and simulated (dashed lines) frequency-response curves of actuator I under conventional excitation for four levels of the voltage amplitude $V_{\mathrm{AC}}$.

curve of the displacement. The results were redimensionalized using the measured resonant frequencies $f_m$ listed in Tables 3.1, 3.3, and 3.4.

The experimentally measured frequency-response curves of actuators I and II tip displacement for the case of $V_{\mathrm{AC}} > 10\,\mathrm{V}$ are compared in Figures 3.31 and 3.32, respectively, to those obtained by integrating the actuator equation of motion, Eq. (2.22). Good agreement can be seen between the model and experimental results for both actuators and throughout the actuation range.

The experimentally measured frequency-response curves of actuator II tip displacement for the case of $V_{\mathrm{AC}} \leq 10\,\mathrm{V}$ are compared in Figure 3.33 to those simulated using Eq. (2.22). It can be seen that in this case, the model underestimates the response. We postulate that our estimate of the field correction factor $\kappa$ accounts for circuit losses incurred in the voltage amplifier. Those losses are absent where the function generator is used alone to drive the actuator.

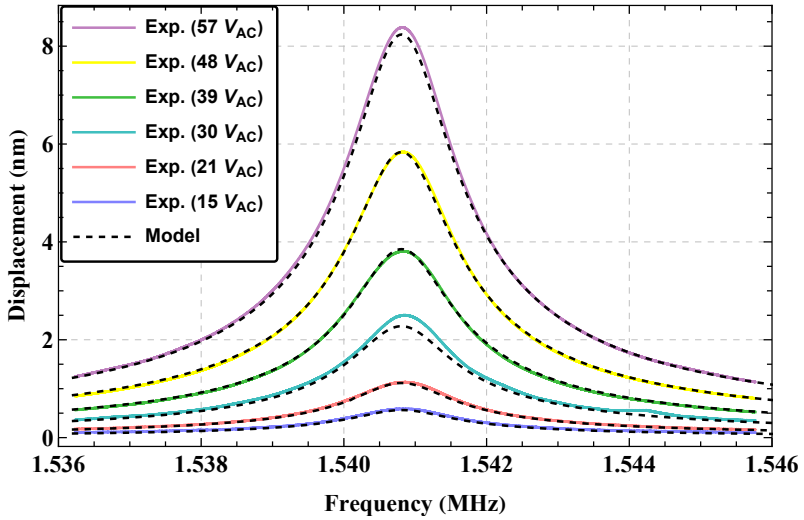



Figure 3.32: Comparison between the experimental (solid lines) and simulated (dashed lines) frequency-response curves of actuator II under conventional excitation for six levels of the voltage amplitude $V_{\mathrm{AC}}$.

## 3.5 Estimation of the Electrical Quality Factor

We used the calibrated models of actuators I and II to estimate the electrical quality factor $Q_e$ of the amplifier circuit, LC tank, for each resonant drive technique by matching the peak of its frequency-response curve obtained experimentally to that obtained by integrating the equation of motion, Eq. (2.22), subject to its signal as described below.

Since the resonance matching technique uses a single tone signal, $f_e$, the amplifier circuit can only work on the AC component of the signal in keeping with our assumption of dynamic decoupling between the electrical and mechanical as discussed in subsection 2.2.5 and section 3.4. Therefore, the electrostatic force generated by this scheme can be defined as

$$\begin{aligned} F_{es}(t) \propto V(t)^2 &= (V_{\mathrm{DC}} + Q_e\, V_{\mathrm{AC}}\, \cos(2\pi f_e t))^2 \\ &= V_{\mathrm{DC}}^2 + \frac{1}{2} Q_e^2 V_{\mathrm{AC}}^2 + 2 Q_e V_{\mathrm{DC}}\, V_{\mathrm{AC}}\, \cos(2\pi f_e t) + \frac{1}{2} Q_e^2 V_{\mathrm{AC}}^2 \cos(4\pi f_e t) \end{aligned} \tag{3.5}$$

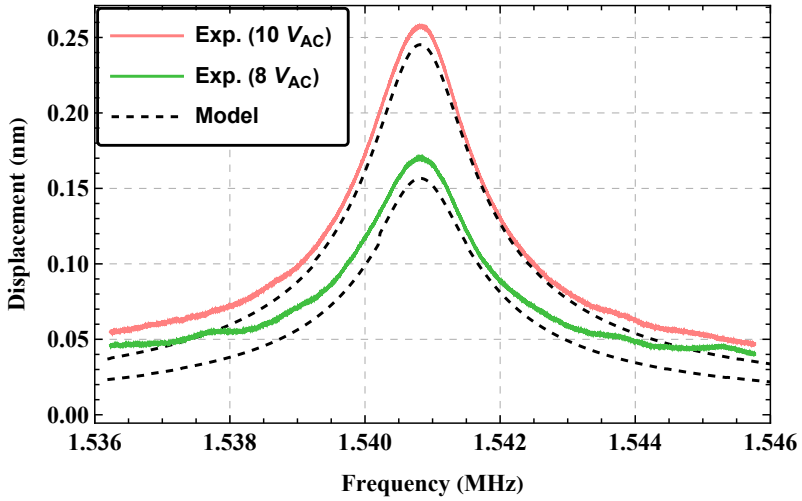



Figure 3.33: Comparison between the experimental (solid lines) and simulated (dashed lines) frequency-response curves of actuator II under conventional excitation for two levels of the voltage amplitude $V_{\mathrm{AC}}$.

The expression shows that the circuit in resonance matching technique amplifies the electrostatic force generated by an unbiased signal by a factor of $Q_e^2$, while amplifying the force generated by biased signal by a factor of $Q_e$ only. Since the electrical quality factor $Q_e$ is significantly larger than 2 in most cases, we conclude that resonance matching is more effective for unbiased signals than biased signals. This is true even after taking into account the the apparent coupling between mechanical and electrical resonances in the biased signals case.

In the biased signal case, the force expression also shows the presence of an actuation force at the second harmonic of the signal frequency $2f_e$. While this force component can be neglected when it is small compared to the first harmonic component ($V_{\mathrm{DC}} >> V_{\mathrm{AC}}$) and the DC component of the electrostatic field is also small enough not to trigger parametric resonance in the in-plane direction, that is not true when this condition is violated. The discrepancy in the apparent $Q_m$ of resonance matching excitation using a biased signal is a result of violating those conditions as discussed above.

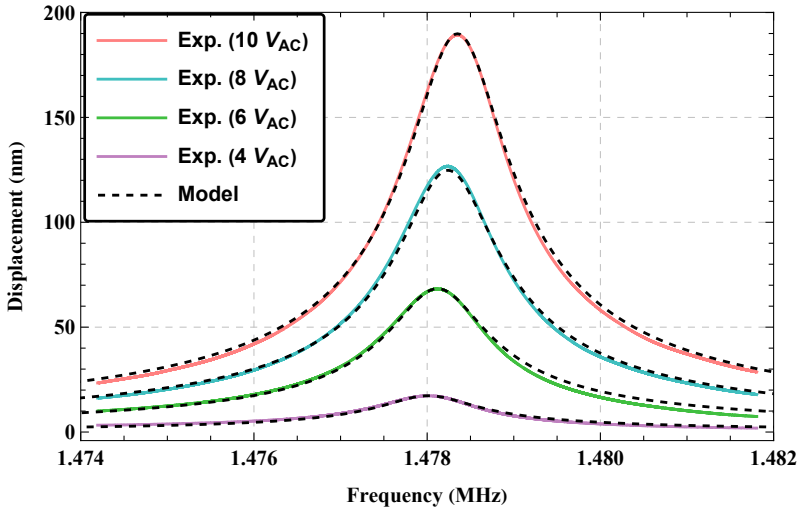



Figure 3.34: Comparison between the experimental (solid lines) and simulated (dashed lines) frequency-response curves of actuator I under resonance matching with unbiased signals for four levels of the voltage amplitude $V_{\mathrm{AC}}$.

Table 3.5: The predicted electrical quality factors for resonance matching excitation with (a) unbiased signals and (b) biased signals with a voltage amplitude of $V_{\mathrm{AC}} = 10\,\mathrm{V}$.

(a)

| $V_{\mathrm{AC}}$ | $Q_e$ |
|---|---|
| 10 | 18.75 |
| 8 | 19 |
| 6 | 18.75 |
| 4 | 14.15 |

(b)

| $V_{\mathrm{DC}}$ | $Q_e$ |
|---|---|
| 31.5 | 20.65 |
| 25 | 20.65 |
| 20 | 23 |

The experimental and simulated frequency response of actuator I under resonance matching actuation with unbiased signals are compared in Figure 3.34. The estimated electrical quality factors are listed in Table 3.5(a). Further, we note that the peak displacement under resonance matching actuation with $V_{\mathrm{AC}} = 6\,\mathrm{V}$ and conventional actuation with $V_{\mathrm{AC}} = 114\,\mathrm{V}$, Figure 3.31, are identical ($w_{\mathrm{RMS}} = 70\,\mathrm{nm}$). The ratio between the two voltages corresponds to an am-

plification factor of $Q_e = 19$, which is consistent with the electrical quality factor estimated by the model above at $Q_e = 18.75$. Similarly, the peak displacements are matched at about $w_{\mathrm{RMS}} = 17.9\,\mathrm{nm}$ for the cases of resonance matching with $V_{\mathrm{AC}} = 4\,\mathrm{V}$ and conventional actuation with $V_{\mathrm{AC}} = 60\,\mathrm{V}$. The ratio between the two voltages results in an amplification factor of $Q_e = 15$, which is consistent with the electrical quality factor estimated by the model at $Q_e = 14.15$. These finding validate the use of the model to estimate $Q_e$. The increase in $Q_e$ beyond $V_{\mathrm{AC}} = 4\,\mathrm{V}$ is due to a switch in the internal drive circuits of the function generate which results in a lower source resistance.

The VNA-measured, see subsection 3.3.1, electrical quality factor of the resonant circuit was $Q_e = 54.35$. We attribute this discrepancy to the resistive loading introduced by the internal electronics of the function generator and the cables connecting it to the resonant drive circuit, Figure 3.12(a). It is important to note that the VNA calibration accounts for measurement path impedance, thereby minimizing their circuit loading.

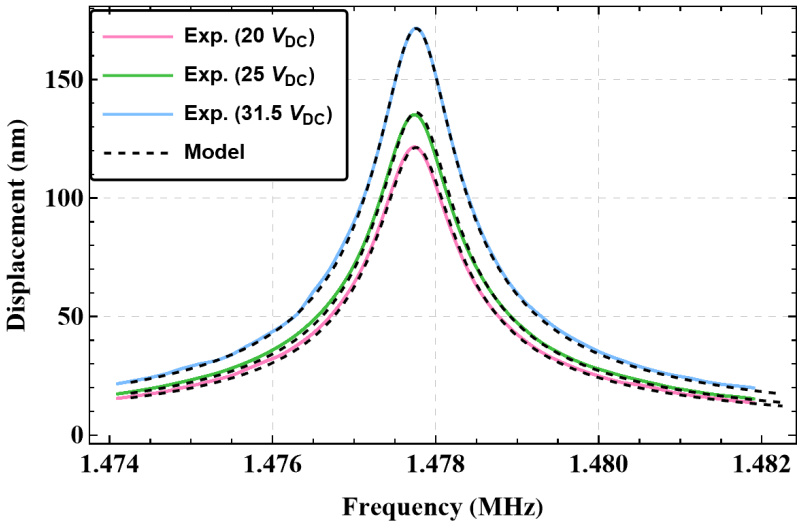



Figure 3.35: Comparison between the experimental (solid lines) and simulated (dashed lines) frequency-response curves of actuator I under resonance matching with biased signals for three levels of bias and a voltage amplitude of $V_{\mathrm{AC}} = 10\,\mathrm{V}$.

The experimental and simulated frequency response of actuator I under resonance matching actuation with biased signals are compared in Figure 3.35. They are found to be in good agreement. The electrical quality factors $Q_e$ estimated from the numerical simulations are listed in Table 3.5(b). We note they are similar to those for the unbiased case.

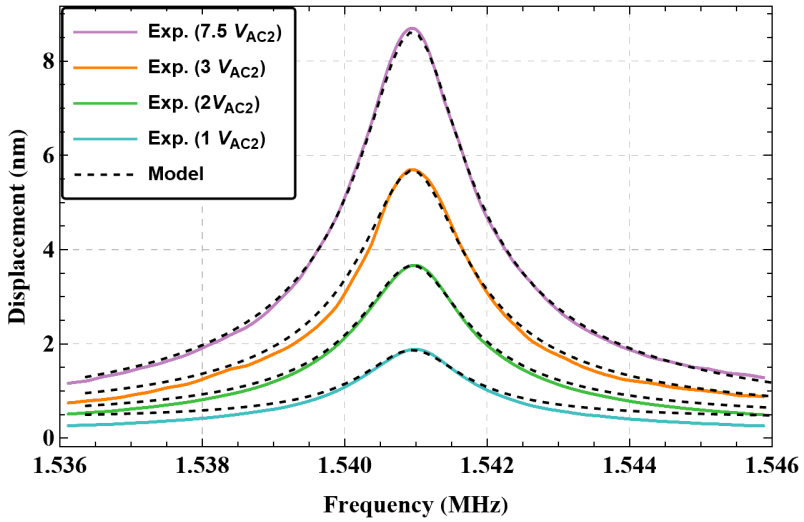



Figure 3.36: Comparison between the experimental (solid lines) and simulated (dashed lines) frequency-response curves of actuator II under multi-frequency excitation with an electrical resonance of $f_e = 6.21$ MHz, an amplifier voltage amplitude of $V_{AC1} = 7.5$ V, and four levels of the actuation voltage amplitude $V_{\mathrm{AC2}}$.

In multi-frequency excitation, a two-tone signal, $f_1$ and $f_2$, is utilized to derive the system. Since the first signal frequency is set equal to the electrical resonance $f_1 = f_e$, it is amplified (its voltage amplitude $V_{\mathrm{AC1}}$ is multiplied) by the electrical quality factor $Q_e$ of the RLC circuit.

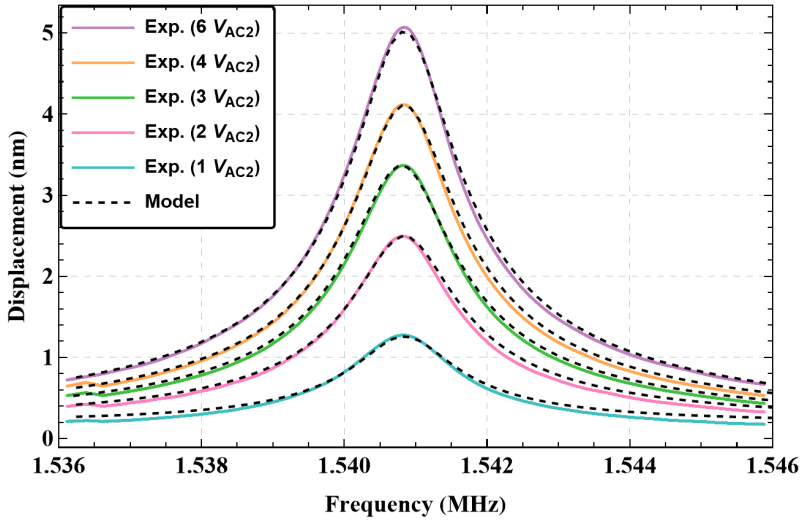
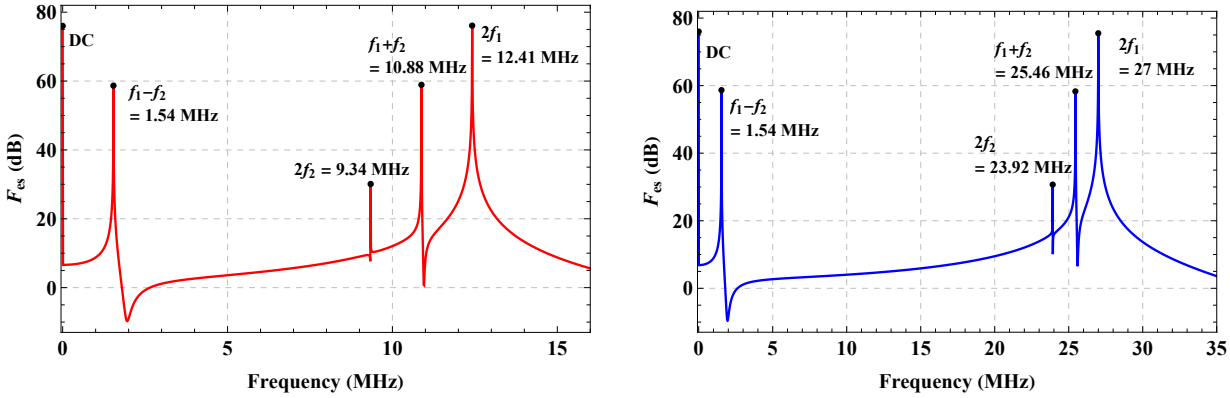



Figure 3.37: Comparison between the experimental (solid lines) and simulated (dashed lines) frequency-response curves of actuator II under multi-frequency excitation with an electrical resonance of $f_e = 13.5\,\text{MHz}$, an amplifier voltage amplitude of $V_{\text{AC1}} = 7.5\,\text{V}$, and five levels of the actuation voltage amplitude $V_{\text{AC2}}$.

Therefore, the electrostatic force can be expressed in the as

$$\begin{aligned} F_{es}(t) \propto V(t)^2 &= (V_{\text{DC}} + Q_e V_{\text{AC1}} \cos(2\pi f_1 t) + V_{\text{AC2}} \cos(2\pi f_2 t))^2 \\ &= \frac{1}{2}\left(Q_e^2 V_{\text{AC1}}^2 + V_{\text{AC2}}^2 + 2V_{\text{DC}}^2\right) \\ &\quad + 2\big(Q_e V_{\text{DC}} V_{\text{AC1}} \cos(2\pi f_1 t) + V_{\text{DC}} V_{\text{AC2}} \cos(2\pi f_2 t)\big) \\ &\quad + \frac{1}{2}\big(Q_e^2\, V_{\text{AC1}}^2 \cos(4\pi f_1 t) + V_{\text{AC2}}^2 \cos(4\pi f_2 t)\big) \\ &\quad + Q_e V_{\text{AC1}} V_{\text{AC2}}\Big(\cos\big(2\pi(f_1 - f_2)t\big) + \cos\big(2\pi(f_1 + f_2)t\big)\Big) \end{aligned} \tag{3.6}$$

The driving force is the term appearing at $(f_1 - f_2)$ or $(f_1 + f_2)$ depending on the specifications of the actuator under test. We note that the DC component doesn't appear in that term. While bias voltage can be introduced to tune the natural frequency of the actuator or its effective nonlinearity, it is irrelevant to the drive force and, therefore, will be set to $V_{\text{DC}} = 0$ in this study.




(a) (b)

Figure 3.38: FFT representation of multi-frequency signals (a) $f_1 = 6.21$ MHz and $f_2 = 4.6694$ MHz (b) $f_1 = 13.5$ MHz and $f_2 = 11.9594$ MHz

The FFT of the simulated scaled electrostatic force under multi-frequency excitation is shown in Figures 3.38(a) and 3.38(b) for a case with a lower electrical resonance of $f_e = 6.21\,\text{MHz}$ obtained via a larger inductor $L_1 = 60\,\mu\text{H}$ and a higher electrical resonance of $f_e = 13.5\,\text{MHz}$ obtained via smaller inductor $L_2 = 10\,\mu\text{H}$, respectively. The figure shows that the relevant forcing term appears in both cases at $f_1 - f_2 = 1.54$ MHz.

The experimental and simulated frequency response of actuator II under multi-frequency excitation are compared in Figures 3.36 and 3.37 for the cases of the lower electrical resonance of $f_e = 6.21\,\text{MHz}$ and higher electrical resonance of $f_e = 13.5\,\text{MHz}$, respectively. The model and experiment are in good agreement for both electrical resonances and the various levels of actuation except for low actuation amplitudes $V_{\text{AC2}}$ and the lower electrical resonance, Figure 3.39. In the latter case the model progressively diverges from (overestimates) the measured response as the excitation frequency $f_1 - f_2$ sweeps away from the half-power bandwidth of the resonator.

The electrical quality factors $Q_e$ for both cases of multi-frequency excitation are listed in

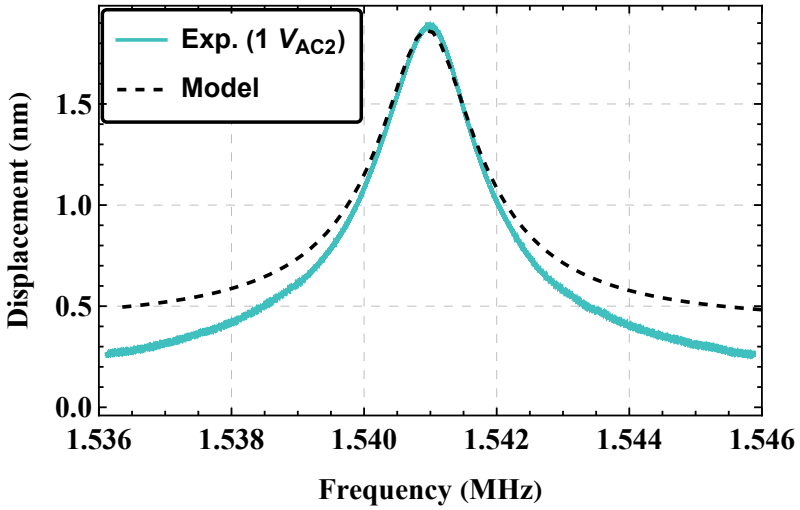



Figure 3.39: The measured (solid line) and simulated (dashed line) frequency-response curves of actuator II under multi-frequency excitation with an electrical resonance of $f_e = 6.21\,\text{MHz}$, an amplifier voltage amplitude of $V_{\text{AC1}} = 7.5\,\text{V}$ , and an actuation voltage amplitude of $V_{\text{AC2}} = 1\,\text{V}$.

Table 3.6. A similar pattern is seen where the quality factor drops for higher second voltage amplitudes $V_{\text{AC2}}$. We investigated whether this was due to the function generator being driven beyond its limitations, resulting in signal saturation for the case of $f_e = 13.5\,\text{MHz}$.

In Figure 3.40, we show six multi-frequency signals captured on an oscilloscope sharing common first signal frequency of $f_1 = 13.5\,\text{MHz}$, second signal frequency of $f_2 = 11.9594\,\text{MHz}$, and first voltage amplitude $V_{\text{AC1}} = 7.5\,\text{V}$ and six levels of the second voltage amplitude $V_{\text{AC2}}$. For the voltage levels $V_{\text{AC2}} = 7.5\,\text{V}$, $6\,\text{V}$, and $5\,\text{V}$, the signal had a peak-to-peak amplitudes of $V_{\text{pp}} = 20.88\,\text{V}$, $20.59\,\text{V}$, and $20.35\,\text{V}$, Figures 3.40(a), (b), and (c), respectively. The small difference in the peak-to-peak voltage amplitude among these cases suggests that the signal is saturated at these voltages. Similarly, saturation is observed for $V_{\text{AC2}} = 4\,\text{V}$ and $3\,\text{V}$ with output peak-to-peak amplitudes of $V_{\text{pp}} = 19.87\,\text{V}$ and $19.29\,\text{V}$, respectively, Figures 3.40(d) and (e). On the other hand, in Figure 3.40(f), the peak-to-peak amplitude for $V_{\text{AC2}} = 2\,\text{V}$ was measured as $V_{\text{pp}} = 18.38\,\text{V}$, which is lower by $1\,\text{V}$ from that for $V_{\text{AC2}} = 3\,\text{V}$. This proves that the signal

Table 3.6: The electrical quality factors for multi-frequency excitation with an amplifier voltage amplitude $V_{\mathrm{AC1}} = 7.5\,\mathrm{V}$ and an electrical resonance of (a) $f_e = 6.21\,\mathrm{MHz}$ and (b) $f_e = 13.5\,\mathrm{MHz}$.

(a)

| $V_{\mathrm{AC2}}$ | $Q_e$ |
|---|---|
| 7.5 | 30.2 |
| 3 | 49.6 |
| 2 | 47.9 |
| 1 | 47.9 |

(b)

| $V_{\mathrm{AC2}}$ | $Q_e$ |
|---|---|
| 6 | 22 |
| 4 | 27 |
| 3 | 29.5 |
| 2 | 32.7 |
| 1 | 32.7 |

saturates for the voltage levels of $V_{\mathrm{AC2}} > 2\,\mathrm{V}$, thereby explaining the apparent drop in quality factor $Q_e$ observed for these cases. The same behavior is observed for $V_{\mathrm{AC2}} > 3\,\mathrm{V}$ in the th case of $f_e = 6.21\,\mathrm{MHz}$.

Therefore, the electrical quality factor for the lower frequency circuit is in the range $Q_e = 47.9 - 49.6$ while that for the higher frequency circuit is $Q_e = 32.7$. On the other hand, the VNA-measured electrical quality factors, subsection 3.3.1, for those circuits are $Q_e = 35.15$ and $Q_e = 32.58$, respectively. While the quality factors match closely for the case of $f_e = 13.5\,\mathrm{MHz}$, the increase in the observed electrical quality factor $Q_e$ for the case of $f_e = 6.21\,\mathrm{MHz}$ needs further investigation.

In the third technique, the system is excited with an amplitude-modulated signal consisting of two frequencies $f_e$ and $f_b$. Since the first signal frequency is the electrical resonance frequency $f_e$, it is amplified (its voltage amplitude $V_{\mathrm{AC1}}$ is multiplied) by the electrical quality factor $Q_e$.

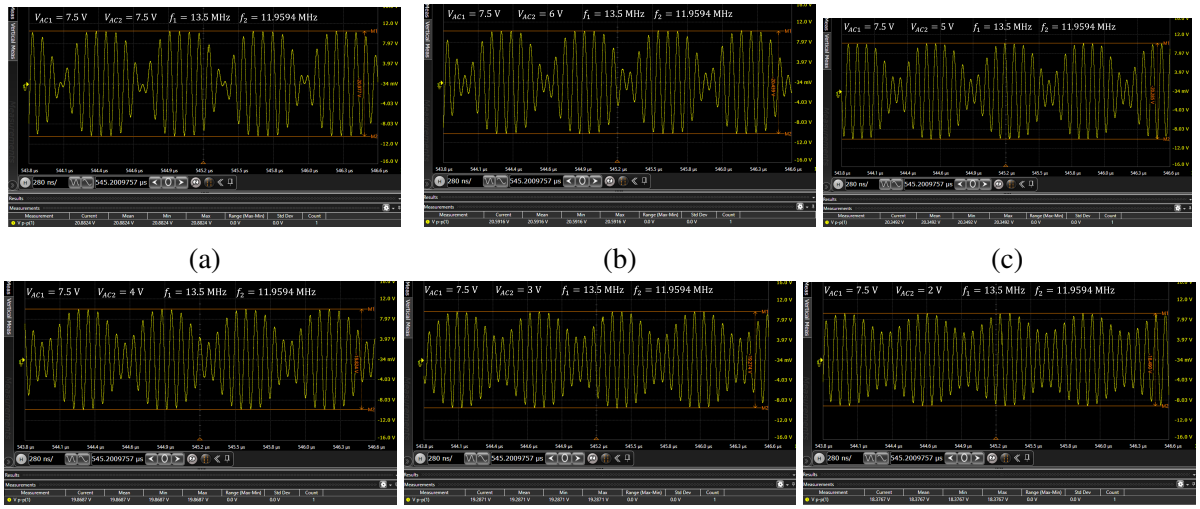


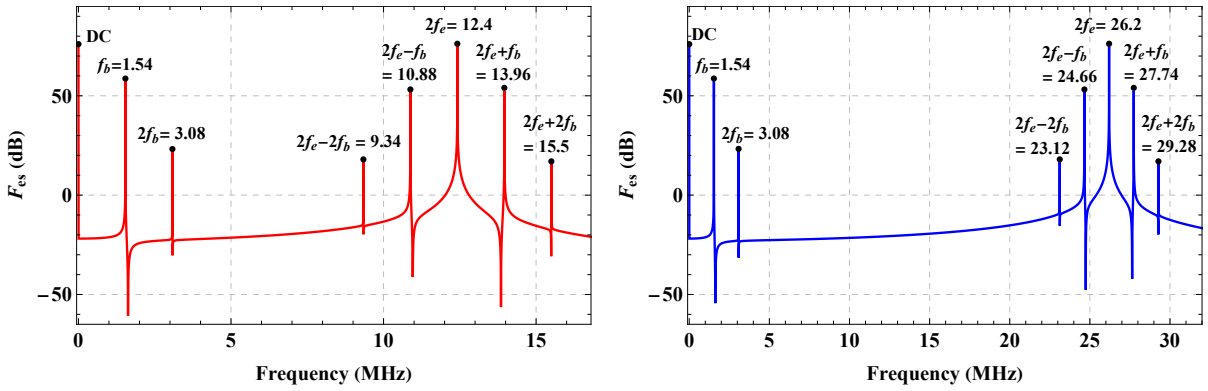

Figure 3.40: Multi-frequency signals measured by an oscilloscope with common first signal frequency of $f_1 = 13.5\,\text{MHz}$, second signal frequency of $f_2 = 11.9594\,\text{MHz}$, and first voltage amplitude of $V_{\text{AC1}} = 7.5\,\text{V}$ and six levels of the second voltage amplitude: (a) $V_{\text{AC2}} = 7.5\,\text{V}$ (b) $V_{\text{AC2}} = 6\,\text{V}$ (c) $V_{\text{AC2}} = 5\,\text{V}$ (d) $V_{\text{AC2}} = 4\,\text{V}$ (e) $V_{\text{AC2}} = 3\,\text{V}$ (d) $V_{\text{AC2}} = 2\,\text{V}$.

Thus, the electrostatic force can be written as

$$\begin{aligned} F_{es}(t) \propto V(t)^2 &= \left(Q_e\, V_{\text{AC1}} \cos(2\pi f_e t) + V_{\text{AC2}} \cos(2\pi f_b t)\right)^2 \cos^2(2\pi f_e t) \\ &= \frac{1}{4}(2Q_e^2\, V_{\text{AC1}}^2 + V_{\text{AC2}}^2) + \frac{1}{4}(2Q_e^2\, V_{\text{AC1}}^2 + V_{\text{AC2}}^2)\cos(4\pi f_e t) \\ &\quad + \frac{Q_e}{2} V_{\text{AC1}}\, V_{\text{AC2}} \Big( \cos\left(2\pi(2f_e - f_b)t\right) + \cos\left(2\pi(2f_e + f_b)t\right)\Big) \\ &\quad + \frac{1}{8} V_{\text{AC2}}^2 \Big( \cos\left(4\pi(f_e - f_b)t\right) + \cos\left(4\pi(f_e + f_b)t\right)\Big) \\ &\quad + Q_e\, V_{\text{AC1}} V_{\text{AC2}}\, \cos(2\pi f_b t) + \frac{1}{4} V_{\text{AC2}}^2 \cos(4\pi f_b t) \end{aligned} \tag{3.7}$$

The force expression shows the presence of two actuation forces at the first $f_b$ and second harmonics $2f_b$ of the baseband frequency. Unlike the case of resonance matching, this force component can be safely neglected since $V_{\text{AC2}}$ is not amplified provided that the DC components of the

electrostatic field is small enough not to trigger parametric resonance in the in-plane direction. Further, we set $V_{\mathrm{DC}} = 0$ since it will not affect the drive terms at $f_b$ and $2f_b$.




(a) (b)

Figure 3.41: The FFT of a scaled simulation of the electrostatic force under amplitude-modulated excitation with frequencies of (a) $f_e = 6.21$ MHz and $f_b = 1.54$ MHz (b) $f_e = 13.1$ MHz and $f_b = 1.54$ MHz

The FFT of the simulated scaled electrostatic force under amplitude-modulation excitation is shown in Figures 3.41(a) and 3.41(b) for a case with a lower electrical resonance $f_e = 6.21$ MHz obtained via a larger inductor $L_1 = 60$ µH and a higher electrical resonance of $f_e = 13.1$ MHz obtained via a smaller inductor $L_2 = 13.1$ MHz, respectively. The figure shows the relevant forcing terms appears in both cases at $f_b = 1.54$ MHz and $2f_b = 3.08$ MHz.

The experimental and simulated frequency response of actuator II under amplitude-modulated signals are compared in Figures 3.42 and 3.43 for the case of lower electrical resonance $f_e = 6.21$ MHz (a larger inductor $L_1 = 60$ µH) and a higher electrical resonance $f_e = 13.1H$ (a smaller inductor $L_2 = 10$ µH), respectively. The model and experiment are found to be in good agreement.

The estimated electrical quality factor $Q_e$ for both excitation cases are listed in Tables 3.7. The quality factors are almost constant in each case at $Q_e = 20$ and $Q_e = 33.5$ except for the highest second voltage amplitude ($V_{\mathrm{AC2}} = 7.5$ V). We investigated whether this discrepancy was

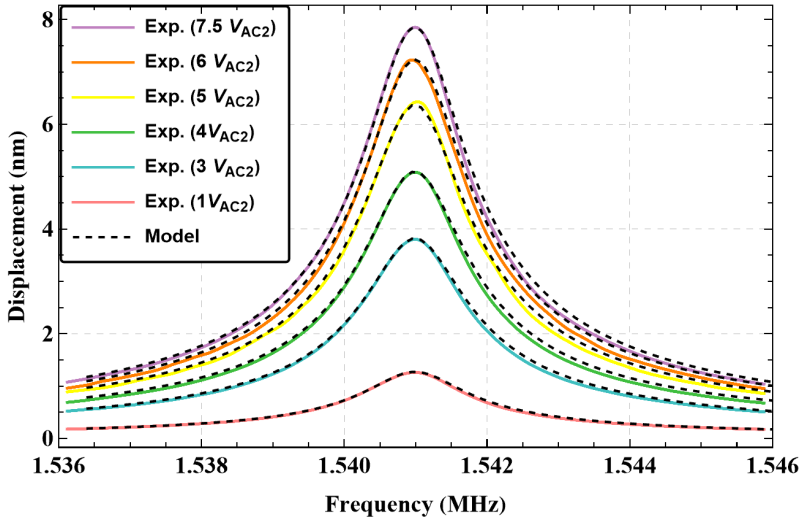



Figure 3.42: Comparison between the experimental (solid lines) and simulated (dashed lines) frequency-response curves of actuator II under amplitude-modulated signals with an electrical resonance of $f_e = 6.21$ MHz, an amplifier voltage amplitude of $V_{\mathrm{AC1}} = 7.5$ V, and six levels of the actuation voltage amplitude $V_{\mathrm{AC2}}$.

due to the function generator being driven beyond its limitations, resulting in signal saturation for the cases of $V_{\mathrm{AC2}} = 7.5$ V and 6 V.

In Figure 3.44, we show four amplitude modulated signals captured on an oscilloscope sharing common carrier frequency $f_e = 13.1$ MHz, basedband frequency $f_b = 1.5406$ MHz, and first voltage amplitude $V_{\mathrm{AC1}} = 7.5$ V and four levels of the second voltage amplitude $V_{\mathrm{AC2}}$. At the voltage levels $V_{\mathrm{AC2}} = 7.5$ and 6 V, the signal had a peak-to-peak amplitude of $V_{\mathrm{pp}} = 22.37$ V, Figures 3.44(a) and (b), respectively, which is very close to that observed in Figure 3.44(c) ($V_{\mathrm{pp}} = 22.33$V) for $V_{\mathrm{AC2}} = 5$ V. On the other hand, the peak-to-peak amplitude for $V_{\mathrm{AC2}} = 4$ V was measured as $V_{\mathrm{pp}} = 21.3$ V, Figure 3.44(d). This proves that the signal saturates for the cases of $V_{\mathrm{AC2}} = 7.5$ V and 6 V.

The estimated quality factor in the first amplitude modulated case ($f_e = 6.21$ MHz) was $Q_e = 33.5$ which is close to the VNA-measured quality factor of the circuit at $Q_e = 35.15$. In

Table 3.7: The electrical quality factors for amplitude modulation excitation with an amplifier voltage amplitude $V_{\mathrm{AC1}} = 7.5\,\mathrm{V}$ and an electrical resonance of (a) $f_e = 6.21\,\mathrm{MHz}$ and (b) $f_e = 13.1\,\mathrm{MHz}$.

(a)

| $V_{\mathrm{AC2}}$ | $Q_e$ |
|---|---|
| 7.5 | 27.5 |
| 6 | 31.8 |
| 5 | 33.5 |
| 4 | 33.5 |
| 3 | 33.5 |
| 1 | 33.5 |

(b)

| $V_{\mathrm{AC2}}$ | $Q_e$ |
|---|---|
| 7.5 | 16 |
| 4 | 20 |
| 3 | 20 |
| 2 | 20 |
| 1 | 20 |

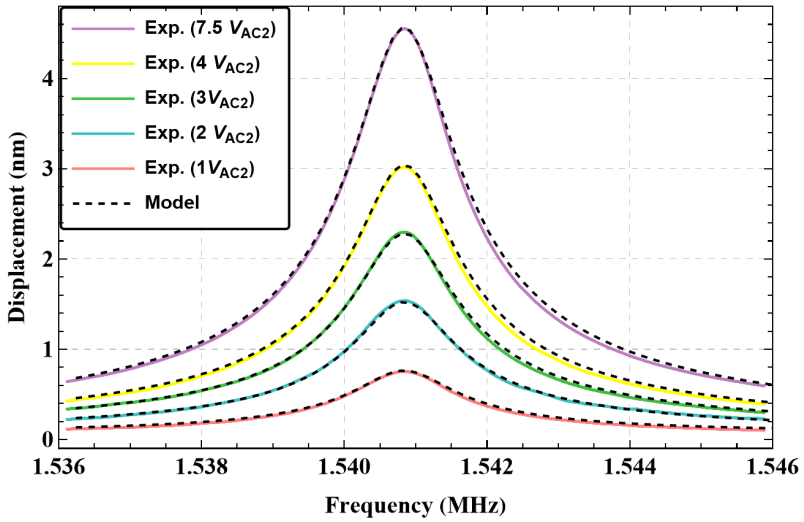
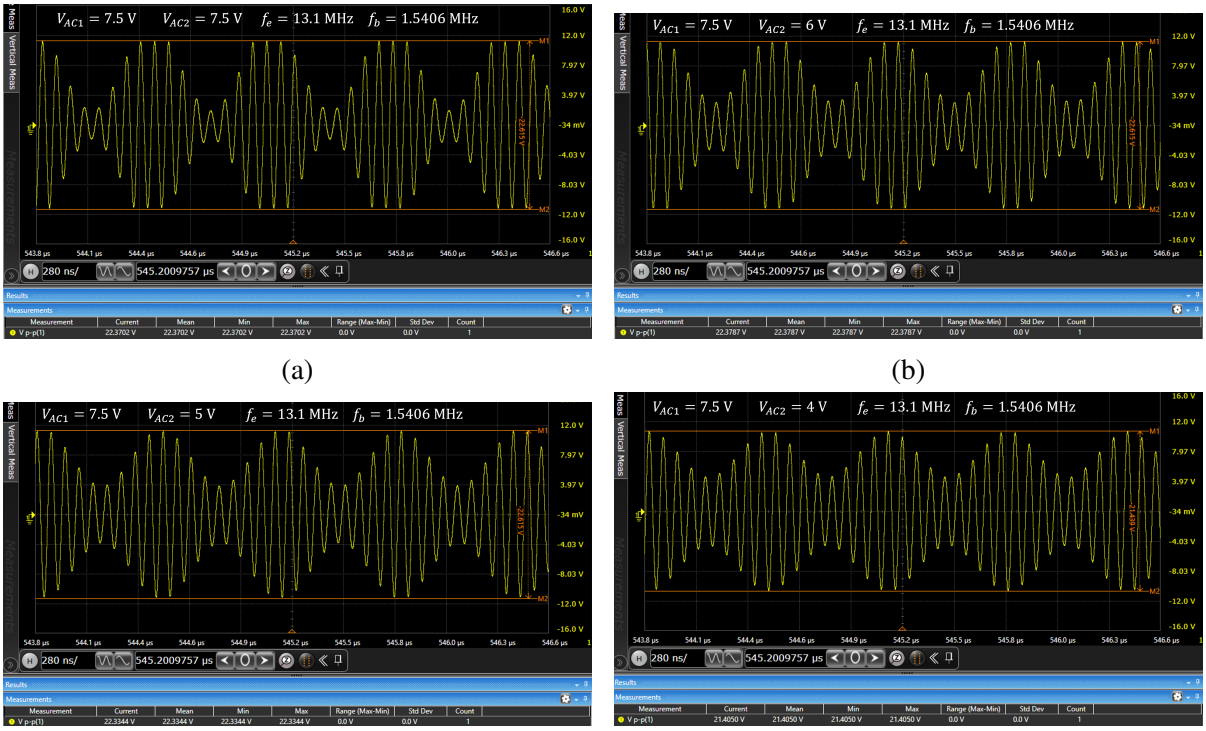



Figure 3.43: Comparison between the experimental (solid lines) and simulated (dashed lines) frequency-response curves of actuator II under amplitude-modulated signals with an electrical resonance of $f_e = 13.1\,\mathrm{MHz}$, an amplifier voltage amplitude of $V_{\mathrm{AC1}} = 7.5\,\mathrm{V}$, and five levels of the actuation voltage amplitude $V_{\mathrm{AC2}}$.

the second case ($f_e = 13.1\,\mathrm{MHz}$), the model estimated quality factor was $Q_e = 20$ compared to




(a) (b)

(c) (d)

Figure 3.44: Amplitude-modulated signals measured by an oscilloscope with common carrier frequency of $f_e = 13.1\,\text{MHz}$, baseband frequency of $f_b = 1.5406\,\text{MHz}$, and first voltage amplitude of $V_{\text{AC1}} = 7.5\,\text{V}$ and four levels of the second voltage amplitude: (a) $V_{\text{AC2}} = 7.5\,\text{V}$ (b) $V_{\text{AC2}} = 6\,\text{V}$ (c) $V_{\text{AC2}} = 5\,\text{V}$ (d) $V_{\text{AC2}} = 4\,\text{V}$.

the VNA-measured quality factor of the circuit at $Q_e = 32.58$. The reasons for this discrepancy are not obvious and requires further investigation.

### 3.5.1 Model Limitations

In the experiments for resonance matching and conventional excitations, it was observed that the resonant frequency shifted to larger values at higher displacement amplitudes as seen in frequency-response curves of Figures 3.31 and 3.34, and the resonant frequencies listed in Table

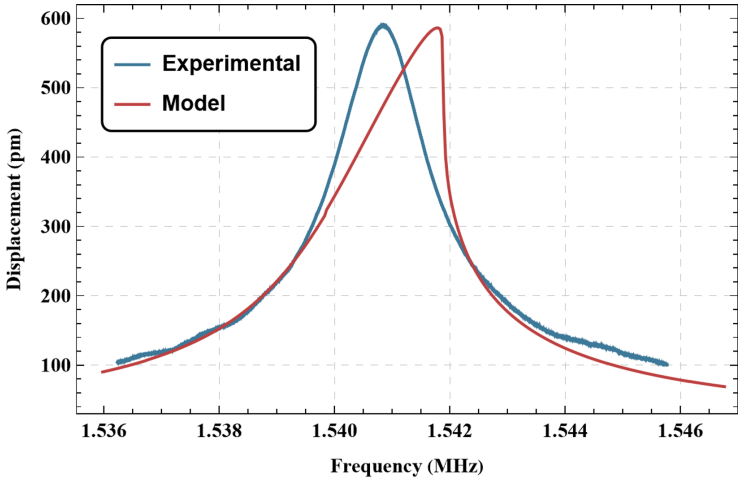



Figure 3.45: simulated (red line) experimental (blue line) frequency response of actuator II under conventional excitation with an amplitude of $V_{\mathrm{AC}} = 15\,\mathrm{V}$ and a cubic nonlinearity of $\alpha_3 = 30$.

3.1. The model does not account for this shift and assumes a constant natural frequency and, thus, a constant linear stiffness as per Eq. (2.28). We overcame this limitation by using the measured natural frequencies to redimensionalize the simulated frequency-response curves as described in section 3.4. The good agreement between the simulated and measured curves obtained using this adjustment indicates that the model lacks an amplitude-dependent linear stiffening.

To further investigate this hypothesis, we added a hardening cubic nonlinearity $\alpha_3$ to the model such that

$$\ddot{w} + \frac{1}{Q_m}\,\dot{w} + \alpha_3 w^3 = \alpha\, V(t)^2\ \mathrm{sgn}(w_\circ - w) \tag{3.8}$$

Figure 3.45, shows the simulated and measured frequency-response curves of actuator II under conventional excitation with an amplitude of $V_{\mathrm{AC}} = 15\,\mathrm{V}$ and $\alpha_3 = 30$. The simulated curve is qualitatively different, skewed to the right, from that observed experimentally. This appears to confirm of hypothesis. The origins of this linear hardening stiffness may lie in the fringing electrostatic field rather than the mechanical potential, as discussed in subsection 3.3.3.

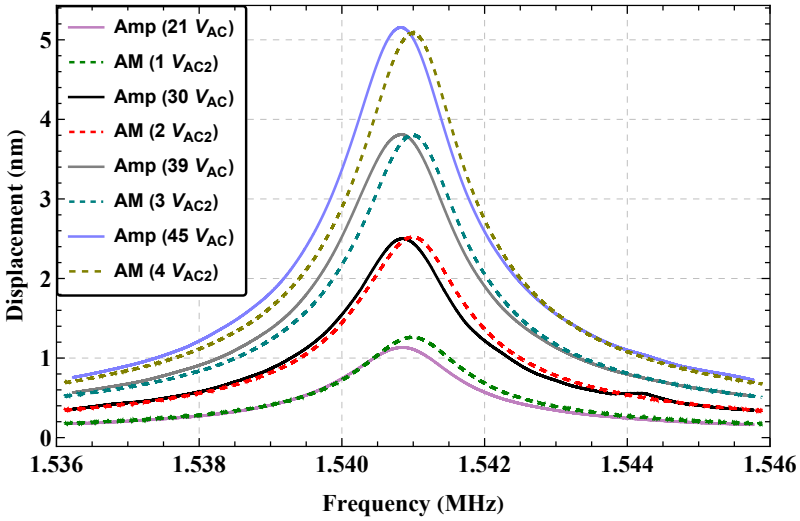



Figure 3.46: The Experimental frequency-response curves of actuator II showing the frequency shift between in the response under conventional excitation (solid lines) and amplitude-modulation excitation (dashed lines).

The shift of the frequency-response curves to higher frequencies when actuator II was excited by amplitude-modulation ($f_e = 6.21\,\text{MHz}$) versus a voltage amplifier, see Figure 3.46 and the corresponding resonant frequencies listed in Table 3.3, indicates a weak coupling between the mechanical and electrical subsystems. This is consistent since $f_e > f_m$, therefore the reactance of the RLC circuit is capacitive dominated at the mechanical resonance and will tend to stiffen the coupled system. Although the shift is marginal, it demonstrates the limitations of our assumption of dynamic decoupling between the two subsystems.

## 3.6 Comparison Among the Actuation Techniques

To evaluate the performance of the three actuation techniques and compare among them we define a magnification factor

$$\text{MF} = \frac{w_{\text{RMS}}}{V_{\text{RMS}}} \text{ (nm/V)} \tag{3.9}$$

that describes the efficiency of electromechanical coupling between the system input, namely the voltage signal applied to the MEMS circuit, and its output, the of the measured displacement $w(t)$. To avoid the ambiguity posed by the presence of multiple local maxima in cases where either signal contains more than one frequency, those signals are quantified in terms of their RMS. The magnification factor serves as a figure of merit allowing us to quantify the relative merits of various actuation schemes in various applications.

Table 3.8: Realized magnification factors for actuator I.

| $V_{\text{in}}$ (V) | $V_{\text{RMS}}$ (V) | $w_{\text{RMS}}$ (nm) | MF (nm/V) | $\text{MF}_{\text{Avg}}$ (nm/V) |
|---|---|---|---|---|
| Voltage Amplifier | | | | |
| 114 $V_{\text{AC}}$ | 80.61 | 70 | 0.868 | 0.694 |
| 105 $V_{\text{AC}}$ | 74.246 | 61 | 0.822 | |
| 90 $V_{\text{AC}}$ | 63.64 | 42 | 0.66 | |
| 60 $V_{\text{AC}}$ | 42.426 | 18 | 0.424 | |
| Resonance Matching (unbiased) | | | | |
| 10 $V_{\text{AC}}$ | 7.071 | 189 | 26.7 | 17.8 |
| 8 $V_{\text{AC}}$ | 5.657 | 127 | 22.5 | |
| 6 $V_{\text{AC}}$ | 4.243 | 68 | 16 | |
| 4 $V_{\text{AC}}$ | 2.828 | 17 | 6 | |
| Resonance Matching (biased) | | | | |

| $V_{\text{in}}$ (V) | $V_{\text{RMS}}$ (V) | $w_{\text{RMS}}$ (nm) | MF (nm/V) | $\text{MF}_{\text{Avg}}$ (nm/V) |
|---|---|---|---|---|
| 31.5 $V_{\text{DC}}$ + 10 $V_{\text{AC}}$ | 32.284 | 171 | 5.3 | 5.4 |
| 25 $V_{\text{DC}}$ + 10 $V_{\text{AC}}$ | 25.981 | 135 | 5.2 | |
| 20 $V_{\text{DC}}$ + 10 $V_{\text{AC}}$ | 21.213 | 121 | 5.7 | |

Table 3.9: Realized magnification factors actuator II.

| $V_{\text{in}}$ (V) | $V_{\text{RMS}}$ (V) | $w_{\text{RMS}}$ (nm) | MF (nm/V) | $\text{MF}_{\text{Avg}}$ (nm/V) |
|---|---|---|---|---|
| Function Generator | | | | |
| 10 $V_{\text{AC}}$ | 7.071 | 0.257 | 0.0364 | 0.0332 |
| 8 $V_{\text{AC}}$ | 5.657 | 0.17 | 0.0301 | |
| Voltage Amplifier | | | | |
| 57 $V_{\text{AC}}$ | 40.305 | 8.382 | 0.208 | 0.136 |
| 45 $V_{\text{AC}}$ | 31.82 | 5.155 | 0.162 | |
| 39 $V_{\text{AC}}$ | 27.577 | 3.809 | 0.138 | |
| 33 $V_{\text{AC}}$ | 23.334 | 2.854 | 0.122 | |
| 30 $V_{\text{AC}}$ | 21.213 | 2.501 | 0.118 | |
| 21 $V_{\text{AC}}$ | 14.849 | 1.133 | 0.0763 | |
| 15 $V_{\text{AC}}$ | 10.607 | 0.59 | 0.0896 | |
| Multi-Frequency Excitation (60 µH) | | | | |
| 7.5 $V_{\text{AC1}}$ + 7.5 $V_{\text{AC2}}$ | 7.5 | 8.696 | 1.16 | 0.871 |
| 7.5 $V_{\text{AC1}}$ + 6 $V_{\text{AC2}}$ | 6.792 | 7.986 | 1.18 | |
| 7.5 $V_{\text{AC1}}$ + 3 $V_{\text{AC2}}$ | 5.712 | 5.698 | 0.998 | |
| 7.5 $V_{\text{AC1}}$ + 2 $V_{\text{AC2}}$ | 5.489 | 3.666 | 0.668 | |
| 7.5 $V_{\text{AC1}}$ + 1 $V_{\text{AC2}}$ | 5.35 | 1.885 | 0.352 | |

| $V_{\text{in}}$ (V) | $V_{\text{RMS}}$ (V) | $w_{\text{RMS}}$ (nm) | MF (nm/V) | $\text{MF}_{\text{Avg}}$ (nm/V) |
|---|---|---|---|---|
| Multi-Frequency Excitation (10 µH) | | | | |
| 7.5 $V_{\text{AC1}}$ + 6 $V_{\text{AC2}}$ | 6.792 | 5.07 | 0.747 | 0.575 |
| 7.5 $V_{\text{AC1}}$ + 5 $V_{\text{AC2}}$ | 6.374 | 4.639 | 0.728 | |
| 7.5 $V_{\text{AC1}}$ + 4 $V_{\text{AC2}}$ | 6.011 | 4.116 | 0.685 | |
| 7.5 $V_{\text{AC1}}$ + 3 $V_{\text{AC2}}$ | 5.712 | 3.366 | 0.589 | |
| 7.5 $V_{\text{AC1}}$ + 2 $V_{\text{AC2}}$ | 5.489 | 2.494 | 0.464 | |
| 7.5 $V_{\text{AC1}}$ + 1 $V_{\text{AC2}}$ | 5.35 | 1.275 | 0.238 | |
| Amplitude Modulation (60 µH) | | | | |
| 7.5 $V_{\text{AC1}}$ + 7.5 $V_{\text{AC2}}$ | 6.495 | 7.853 | 1.21 | 0.826 |
| 7.5 $V_{\text{AC1}}$ + 6 $V_{\text{AC2}}$ | 6.093 | 7.229 | 1.19 | |
| 7.5 $V_{\text{AC1}}$ + 5 $V_{\text{AC2}}$ | 5.863 | 6.43 | 1.1 | |
| 7.5 $V_{\text{AC1}}$ + 4 $V_{\text{AC2}}$ | 5.668 | 5.085 | 0.897 | |
| 7.5 $V_{\text{AC1}}$ + 3 $V_{\text{AC2}}$ | 5.511 | 3.805 | 0.69 | |
| 7.5 $V_{\text{AC1}}$ + 2 $V_{\text{AC2}}$ | 5.397 | 2.521 | 0.467 | |
| 7.5 $V_{\text{AC1}}$ + 1 $V_{\text{AC2}}$ | 5.327 | 1.262 | 0.237 | |
| Amplitude Modulation (10 µH) | | | | |
| 7.5 $V_{\text{AC1}}$ + 7.5 $V_{\text{AC2}}$ | 6.495 | 4.55 | 0.701 | 0.46 |
| 7.5 $V_{\text{AC1}}$ + 6 $V_{\text{AC2}}$ | 6.093 | 4.184 | 0.687 | |
| 7.5 $V_{\text{AC1}}$ + 4 $V_{\text{AC2}}$ | 5.668 | 3.016 | 0.532 | |
| 7.5 $V_{\text{AC1}}$ + 3 $V_{\text{AC2}}$ | 5.511 | 2.297 | 0.417 | |
| 7.5 $V_{\text{AC1}}$ + 2 $V_{\text{AC2}}$ | 5.397 | 1.537 | 0.285 | |
| 7.5 $V_{\text{AC1}}$ + 1 $V_{\text{AC2}}$ | 5.327 | 0.753 | 0.141 | |

The magnification factors realized for for actuator I and II are listed in Tables 3.8 and 3.9,

respectively. Comparison across the various actuation schemes shows that unbiased resonance matching is most effective achieving the highest magnification factor, $\mathrm{MF}_{\mathrm{Avg}} = 17.8$ nm/V compared to a magnification factor of $\mathrm{MF}_{\mathrm{Avg}} = 5.4$ nm/V for the biased case. This is expected since unbiased resonance matching as it amplifies input voltage by $Q_e^2$ compared an amplification by $Q_e$ only in the biased case.

The performance of multi-frequency and amplitude modulated actuations is inferior to biased resonance matching but they are similar to each other with a slight advantage to the former. The advantage of biased resonance matching is due to its actuation voltage benefiting from amplification via the $Q_e$ of the RLC circuit and the bias voltage $V_{\mathrm{DC}}$ while the latter two realize their amplification only through the $Q_e$ of the RLC circuit. In both multi-frequency and amplitude modulated actuations, lower electrical resonance frequencies $f_e$ (larger inductors) were found to realize better magnification factors, $\mathrm{MF}_{\mathrm{Avg}} = 0.871$ nm/V compared to $\mathrm{MF}_{\mathrm{Avg}} = 0.575$ nm/V for multi-frequency and $\mathrm{MF}_{\mathrm{Avg}} = 0.826$ nm/V compared to $\mathrm{MF}_{\mathrm{Avg}} = 0.46$ nm/V for amplitude modulation. The advantage of multi-frequency over amplitude modulation is likely due to a slightly higher RMS of the actuation voltage given the same signal amplitudes.

Finally, we observe that the magnification factor of actuator I under voltage amplifier actuation was $\mathrm{MF}_{\mathrm{Avg}} = 0.694$ nm/V compared to $\mathrm{MF}_{\mathrm{Avg}} = 0.136$ nm/V for actuator II under the same actuation scheme. The discrepancy in the magnification factor between the two actuators is probably due to the higher stiffness of actuator II.

# Chapter 4

# Parasitics and Artifacts

In this chapter, we investigate various parasitics encountered in MEMS actuators, with a specific emphasis on parasitic capacitance. We also discuss and illustrate some experimental artifacts we encountered during the experiments presented in the previous chapter.

## 4.1 Parastic Capacitance

In this section, we investigate the impact of different wiring and circuit configurations as well as chip layout and wafer specifications on the parasitic capacitance of MEMS actuators. The electrostatic actuator under study in this case is composed of a fixed side electrode and a moving beam, Figure 4.1. The actuator was fabricated using a silicon-on-insulator (SOI) process [44]. Its dimensions are listed in table 4.1. The electrode, the beam, and the underlying substrate are coated with a 400 nm gold layer.

A schematic model of the actuator, its surrounding, and the substrate is shown in Figure 4.2.The MEMS actuating capacitor, between the moving beam and the fixed electrode, is dubbed

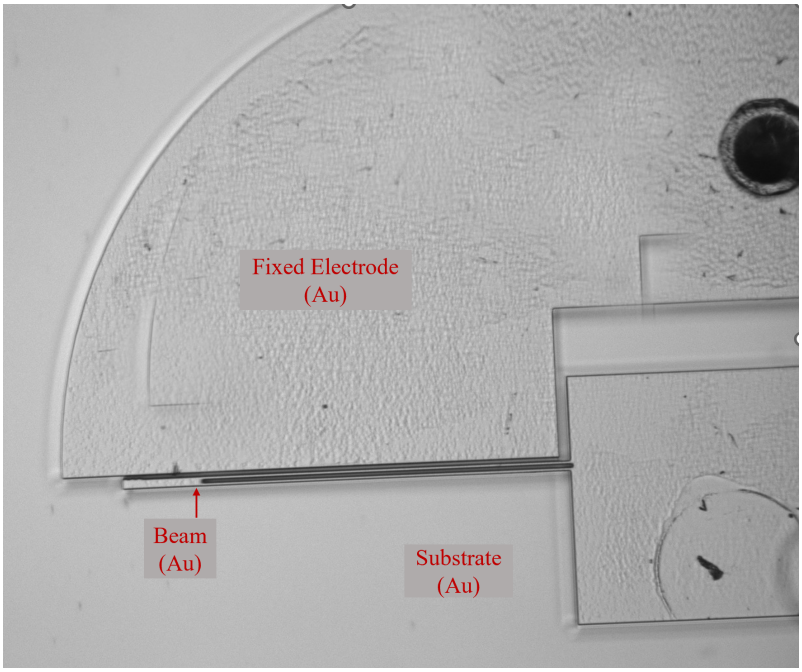



Figure 4.1: A microscopic image of the actuator.

$C_m$. The capacitors between the substrate and the beam and fixed electrode are denoted $C_{\mathrm{Sub1}}$ and $C_{\mathrm{Sub2}}$, respectively. The capacitors between these three elements and the surroundings, structures on the chip surface including other actuators and their wire bonding, are denoted $C_{\mathrm{Sr1}}$, $C_{\mathrm{Sr2}}$, and $C_{\mathrm{Sr3}}$. They represent capacitors between the surroundings and the beam, the fixed electrode, and the substrate, respectively. We assume that $C_{\mathrm{Sr3}}$ is negligible and set to $C_{\mathrm{Sr3}} = 0$. Note that we taking into account the parasitics along the measurement path or the wire bonding of the fixed electrode an the beam. Further, they can be modeled as a parallel capacitor to the MEMS in all the following measurement.

Four capacitance measurements were carried out on the actuator while keeping the surroundings floating (not grounded).

- In the first two cases, the substrate was also left floating.

Table 4.1: Actuator dimensions.

| Parameter | µm |
|---|---|
| beam length ($l$) | 450 |
| beam width ($b$) | 10 |
| beam thickness ($h$) | 30 |
| capacitive gap ($d$) | 3 |
| device-substrate gap ($d_s$) | 2 |

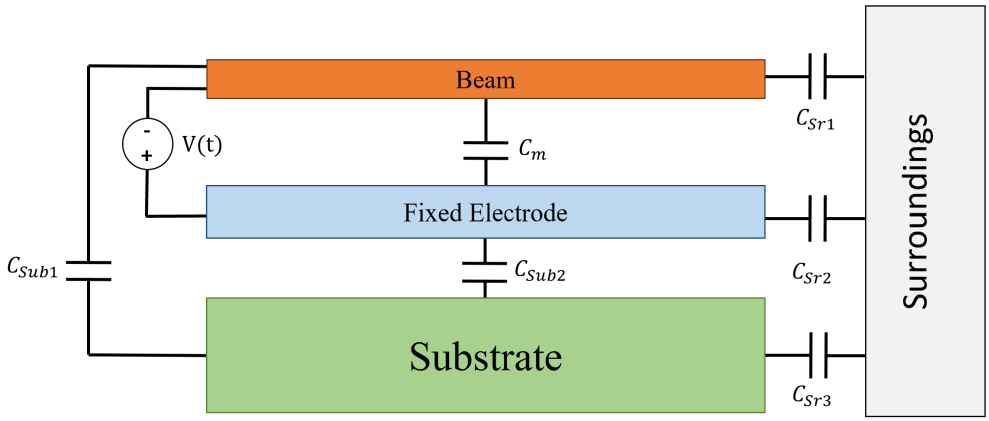



Figure 4.2: A schematic model of the actuator chip.

1) In the first configuration, we connected the high of the signal (+ve) to the beam and grounded the fixed electrode by connecting it to the signal low (-ve).

2) In the second configuration, we reversed the polarity, where the high of signal was connected to the fixed electrode while grounding the beam.

- In the next two cases the substrate was grounded.

3) In the third configuration, the high of the signal was connected to the beam while grounding the fixed electrode.

4) In the fourth configuration, the polarity was switched where the signal high was connected to the fixed electrode and the beam was grounded.

In the first two configuration, all the system capacitors, Figure 4.2, were connected in series, resulting in a reduction in the overall capacitance that can be expressed as

$$C_{1,2} = \frac{1}{\frac{1}{C_m} + \frac{1}{C_{\text{Sub1}}} + \frac{1}{C_{\text{Sub2}}} + \frac{1}{C_{\text{Sr1}}} + \frac{1}{C_{\text{Sr2}}}} \tag{4.1}$$

In the third configuration, grounding of the substrate and the fixed electrode eliminates the capacitor between them ($C_{\text{Sub2}} = 0$). Further, the capacitor between the beam and substrate will be in parallel with the MEMS capacitor ($C_{\text{Sub1}}||C_m$), giving an overall capacitance of

$$C_3 = \frac{1}{\frac{1}{C_m + C_{\text{Sub1}}} + \frac{1}{C_{\text{Sr1}}} + \frac{1}{C_{\text{Sr2}}}} \tag{4.2}$$

In the fourth configuration, grounding the beam and substrate eliminates the capacitor between them ($C_{\text{Sub1}} = 0$). Further, the capacitor between the fixed electrode and substrate will be in parallel with the MEMS capacitor ($C_{\text{Sub2}}||C_m$), giving an overall capacitance of

$$C_4 = \frac{1}{\frac{1}{C_m + C_{\text{Sub2}}} + \frac{1}{C_{\text{Sr1}}} + \frac{1}{C_{\text{Sr2}}}} \tag{4.3}$$

The experimental setup shown in Figure 4.3 was used to measure the capacitance between the high (+ve) and low (-ve) sides applied to the actuator. Capacitance was determined by measuring the $S_{11}$ parameter using a VNA (Keysight P5020A) which was then converted by the VNA into impedance, and the imaginary part of the impedance was extracted as the capacitance value. A calibration process was performed prior to measurements to minimize the effect of the parastics presented by cables and connectors in the measurement path. The power level of the VNA was

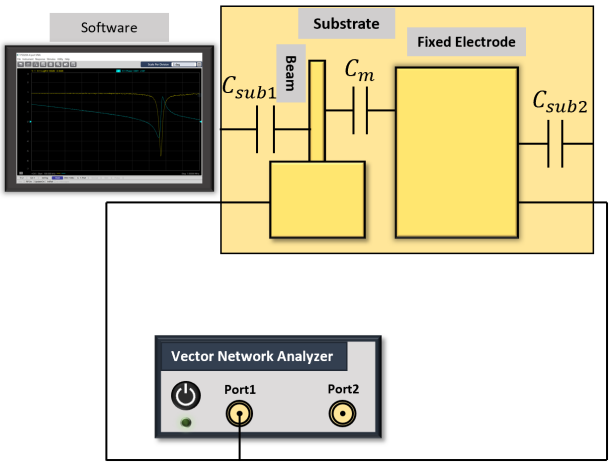



Figure 4.3: The experimental setup for capacitance measurement.

set to 0 dBm. The input signal frequency was swept in the range $f = [0.15 - 5]$ MHz, with a step frequency of 1 kHz and the IF-BW was set to 1 kHz.

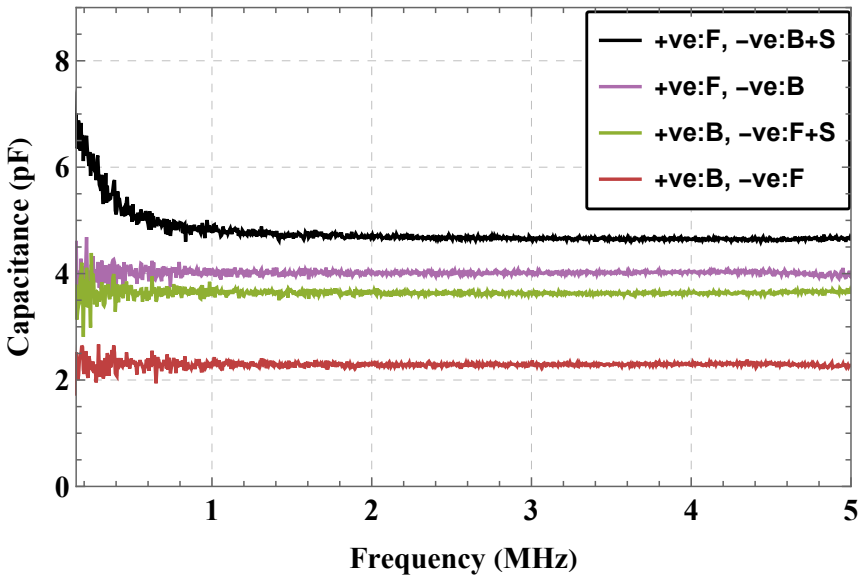



Figure 4.4: The VNA-measured overall capacitance for four actuator wiring configuration.

The measured capacitance for the four configurations are presented in Figure 4.4, where F,

B, and S denote the fixed electrode, beam and, substrate. To improve the signal-to-noise ratio (SNR) of capacitance measurement, it was averaged over the [1–5] MHZ frequency domain for each configuration and listed in Table 4.2. We note that the capacitance in the fourth case is the highest among the configurations tested. This is due to the presence of $C_{\mathrm{Sub2}}$ as a parallel capacitor to the MEMS. This capacitor exhibits a significant overlap area between the substrate and the fixed electrode, which contributes to its larger capacitance value.

Table 4.2: Average capacitance for four actuator wiring configuration.

| Configuration | Color | Capacitance (pF) |
|---|---|---|
| high on beam - floating substrate | red | $C_1 = 2.29099$ |
| high on fixed - floating substrate | purple | $C_2 = 4.01490$ |
| high on beam - grounded substrate | green | $C_3 = 3.63858$ |
| high on fixed - grounded substrate | black | $C_4 = 4.67962$ |

Note that the second case, in theory, should have the same capacitance as the first case. However, we have observed a deviation between the measured capacitance values. We hypothesize that this discrepancy might be caused by the accumulation of charges in the buried oxide layer between the fixed and substrate, which acts as a battery (voltage source) and potentially affects the power measurement of the VNA. Further investigation is required to thoroughly understand this case.

Based on our observations, we can conclude that grounding the substrate and/or the surroundings leads to an increase in the overall measured capacitance of the system, and a higher parasitic capacitance. This increase in capacitance is particularly significant where the motion induced current technique [45] is used to measure the actuator motions. At high frequencies, the current due to parastic capacitance undermines the dynamic range and limits the SNR of the

motional current. Additionally, the increased parasitic capacitance reduces the cutoff frequency of the actuator $f_{\text{cutoff}} = \frac{1}{2\pi RC}$, thereby attenuating the actuation signal.

## 4.2 Other Parasitics

In this section, we address other system parasitics encountered in MEMS, namely ESR of the inductors, parasitic resistance and inductance of the lines, and the loss tangent of the parasitic capacitors.

First, we address the ESR of the inductors. It was experimentally observed that the electrical quality factor $Q_e$ of the resonant circuits improves when larger inductors are used. For instance, when a $L = 2.2\,\text{mH}$ inductor was used, the VNA-measured quality factor was found to be $Q_e = 54.35$, Figure 3.9. On the other hand, when a 10 µH inductor was used, the measured electrical quality factor was found to be $Q_e = 32.58$, Figure 3.10(b). This shows that the ESR of the inductors is negligible compared to the circuit parasitic resistance, which leads to an overall improvement in the quality factor $Q_e$ using larger inductors as previously discussed in chapter 3.

Next, investigate effect of parasitic inductance on the MEMS response under unbiased resonance matching excitation with an external inductor of $L = 2.2\,\text{mH}$. The out-of-plane bending mode of actuator I was measured using the experimental setup shown in Figure 3.12(a). The frequency response of actuator I under a voltage amplitude of $V_{\text{AC}} = 10$,V is shown in Figure 4.5. The actuator initially exhibited a displacement of $w_{\text{RMS}} = 86.89\,\text{nm}$ (red curve). When an external wire was introduced into the electrical path, the displacement increased to $w_{\text{RMS}} = 189.364\,\text{nm}$ (black curve). The VNA-measured electrical resonance frequency was originally $f_e = 780\,\text{kHz}$ which is mismatched with the mechanical resonance at $f_m = 1.4781\,\text{MHz}$. When the external wire was added to the circuit, it acted as a series inductance. As a result, the electrical resonance frequency decreased to match $\frac{1}{2}f_m$.

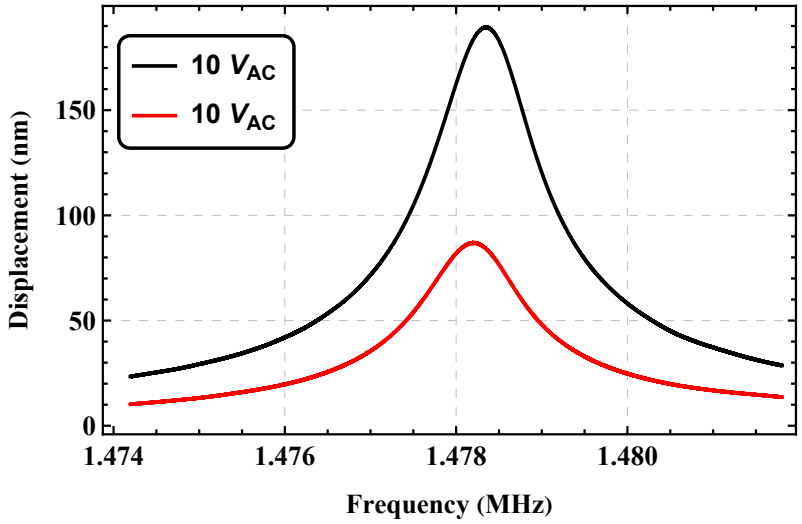



Figure 4.5: The frequency response-curves of actuator I connected in series with a 2.2 mH inductor under unbiased resonance matching excitation with the same voltage amplitude $V_{\mathrm{AC}}$.

The loss tangent of the parastic capacitors played an important role for low electrical resonance frequencies. This was observed in the minimal response of actuator I′ when it was driven by the electrostatic force of the frequency sum $(f_1 + f_2)$. We hypothesized that the reason for this minimal response is to the dominance of the loss tangent when $f_1$ was set to a low value ($< 1$ MHz).

The impact of handle layer parastic capacitor may have also been at the root of the anomalous behavior we observed in the response of Actuator II out-of-plane bending mode under conventional excitation as measured by the standard experimental setup in Figure 3.1. In this case, the signal frequency was swept-up in the vicinity of half of the mechanical resonance frequency $f = \frac{1}{2} f_m = [768 - 773]$ kHz.

The frequency-response curves shown in Figure 4.6 were obtained under four voltage amplitudes with the polarity switched between the fixed electrode and the beam in each case. The magnitude of the frequency response increased in all four cases when the signal high (+ve) was

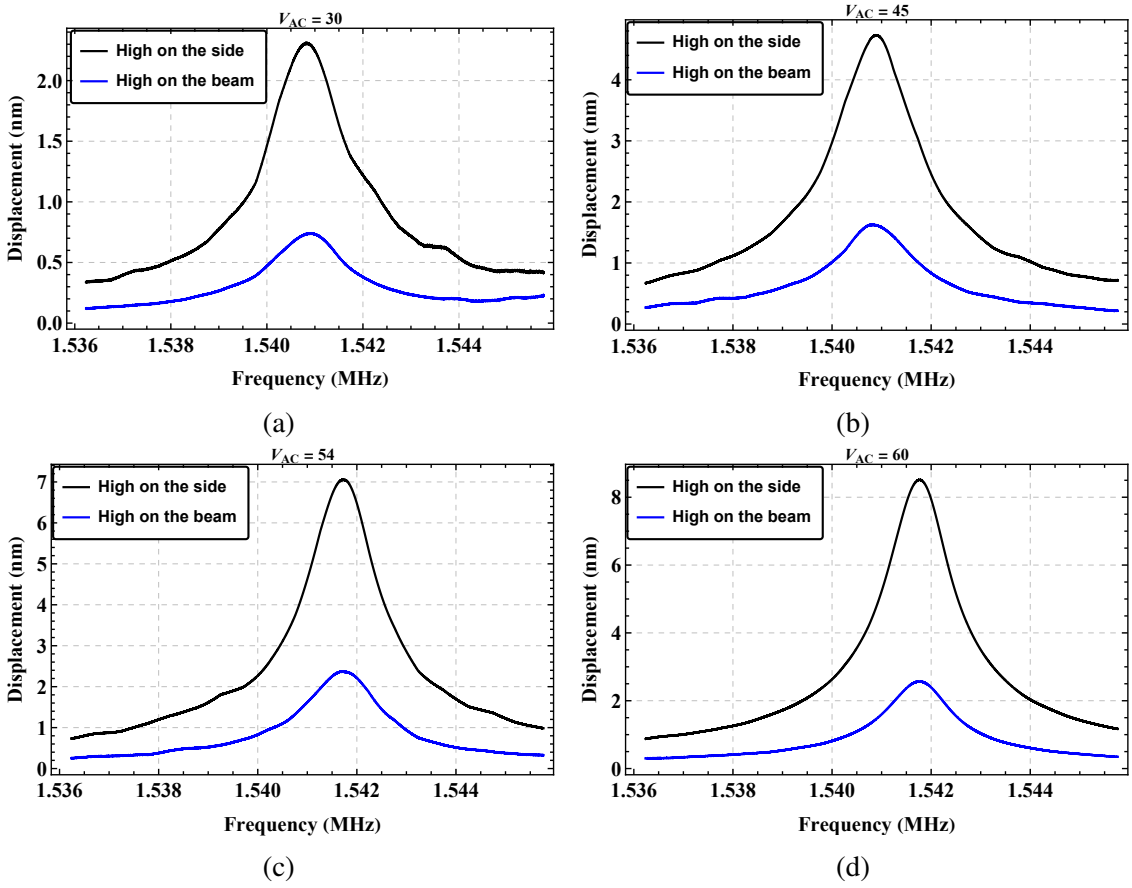



Figure 4.6: The experimental frequency-response curves of actuator II under conventional excitation with an amplitude of: (a) $V_{\mathrm{AC}} = 30$ V (b) $V_{\mathrm{AC}} = 45$ V (c) $V_{\mathrm{AC}} = 54$ V (d) $V_{\mathrm{AC}} = 60$ V.

connected to the side electrode. To assess the repeatability of this behavior, the measurements presented in Figures 4.6(c) and (d) were collected one month after collecting the measurements in Figures 4.6(a) and (b). The amplification in each case, calculated as the ratio between the two peak RMS displacements, is listed in Table 4.3. It was found that, on average, the amplitude of the response was three times higher when the signal high was applied to the side electrode compared to when it was applied to the beam.

We propose a possible explanations for this behavior that induced charges on the handle

Table 4.3: Realized amplification of actuator II response.

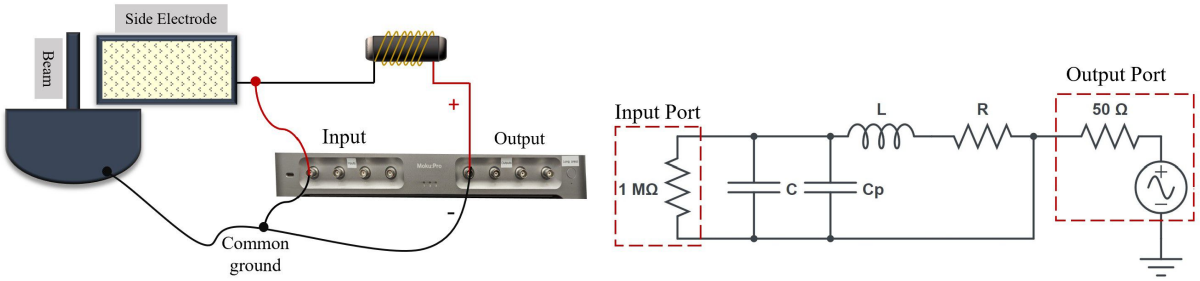
| $V_{\mathrm{AC}}$ (V) | Amplification | Avg. |
|---|---|---|
| 30 | 3.12356 | 3.08219 |
| 45 | 2.91194 | |
| 54 | 2.97698 | |
| 60 | 3.31627 | |

layer may be causing it to act as a capacitor, resulting in increased out-of-plane fringing field and displacements.

## 4.3 Equipment Loading

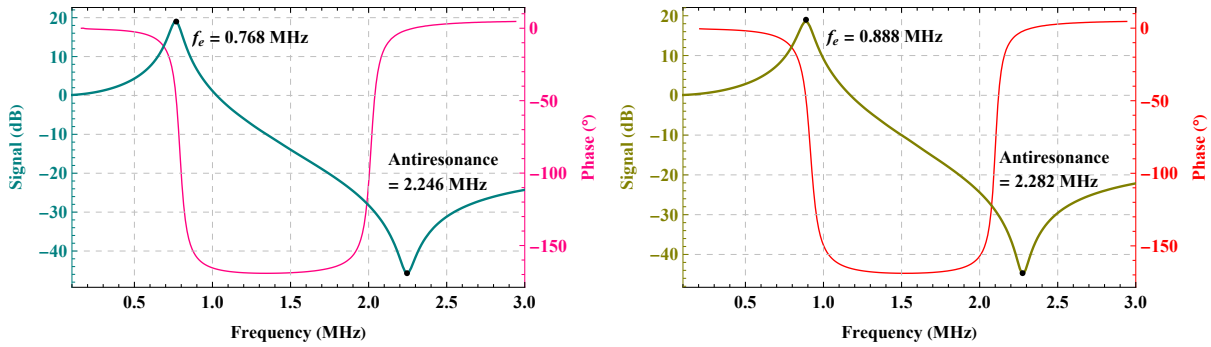
In this section, we present an artifact encountered in characterization of electrical natural frequency $f_e$ when the experimental setup shown in Figure 4.7(a) was used to measure the electrical natural frequency $f_e$ of series RLC circuits consisting of an external inductor $L$, the circuit parasitic resistance $R$, the capacitor $C_m$ formed by the actuator shown in Figure 2.1. The measurement were carried out using the Liquid Instruments' Moku:Pro [40] as a frequency analyzer.

To detect the electrical resonance, the high side of the frequency analyzer output signal was applied to the inductor, while the beam was grounded. The input to the frequency analyzer was connected across the MEMS capacitor to observe the voltage amplification which occurs at the electrical resonance $f_e$. The frequency analyzer measures the voltage amplification by normalizing the measured signal with respect to the applied signal. A lumped-element representation of the circuit is shown in Figure 4.7(b) where the 50 $\Omega$ and the 1 M$\Omega$ resistors represent the internal resistances of the output and input ports of the frequency analyzer, respectively.




(a) (b)

Figure 4.7: (a) The experimental setup for characterization of the RLC circuit and (b) a lumped element schematic of the circuit.




(a) (b)

Figure 4.8: The measured frequency response of an RLC circuit composed of a typical MEMS actuator and two external inductors: (a) $L = 950$ µH (b) $L = 675$ µH

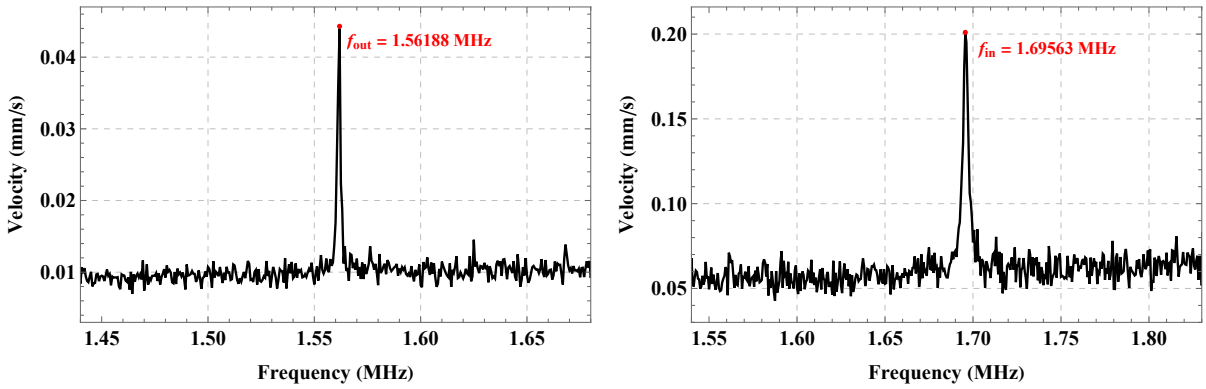
To characterize the RLC circuit, the output voltage level was set to 0.2 V while signal frequency was swept in the range of interest. The amplitude and phase of the frequency response of the RLC circuit are shown in Figure 4.8(a) when an external inductor $L = 950$ µH was connected in series with the actuator. The electrical resonance was found to be $f_e = 768$ kHz compared to a VNA-measured electrical resonance of $f_e = 1.405$ MHz, Figure 3.11(b), and to $f_e = 1.359$ MHz detected optically, Figure 3.17.

The amplitude and phase of the frequency response of the RLC circuit when an external inductor $L = 675$ µH are shown in Figure 4.8(b). The electrical resonance measured using this

setup was found to be $f_e = 888$ kHz compared to a VNA-measured electrical resonance of $f_e = 1.62$ MHz, Figure 3.11(c), and to $f_e = 1.56$ MHz detected optically, Figure 3.18. The significant drop observed in the electrical resonance frequency $f_e$ can be attributed to the presence of the frequency analyzer's probes connected across the capacitor, which represent a 1 MΩ resistor, Figure 4.7(b), as well as other circuit components inside the frequency analyzer.

## 4.4 Transients

In this section, we discuss experimental artifacts encountered in evaluating the frequency response that result in non-stationarity.




(a) (b)

Figure 4.9: FFT of the measured tip velocity for actuator III under pulse excitation showing the response of (a) the first out-of-plane and (b) the first in-plane bending modes.

The actuator under study, actuator III, shares the same design and dimensions as actuators I and II, Figure 2.1. It was characterized using the standard experimental setup in Figure 3.1. Its damped natural frequencies were obtained by applying a pulse train with a 0.01% duty cycle and a $f = 312.5$ Hz frequency to the fixed electrode. The first out-of-plane bending mode was observed at $f_{\text{out}} = 1.56188$ MHz under a voltage of 150 V. The first in-plane bending mode was

measured at $f_{\text{in}} = 1.69563$ MHz under a voltage amplitude of 160 V. The quality factors of the two modes were calculated using the half-power bandwidth method from the measured FFT as $Q_{\text{out}} = 1174.34$ and $Q_{\text{in}} = 586.721$ corresponding to settling times of $t_s = Q_{\text{out}} T_{\text{out}} = 0.75188$ ms and $t_s = Q_{\text{in}} T_{\text{in}} = 0.346021$ ms.

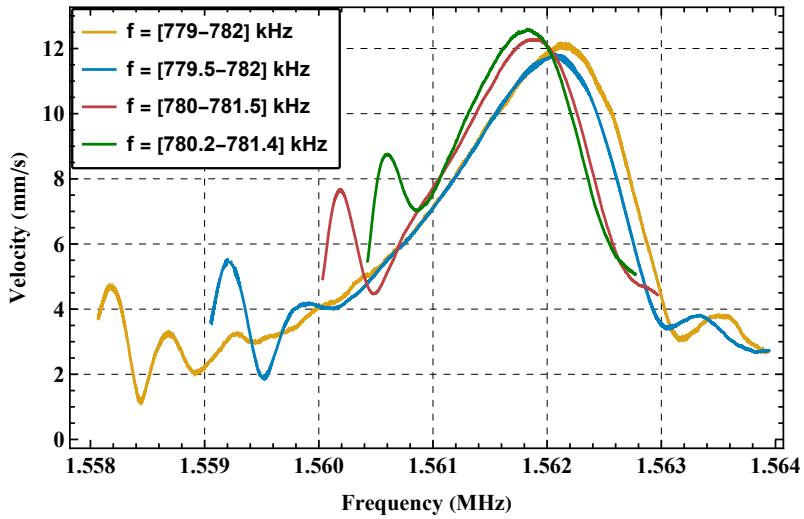



Figure 4.10: Non-stationary 'frequency-response' curves of actuator III beam tip velocity using four excessively fast slew rates.

To observe the response of the out-of-plane bending mode under unbiased voltage waveform, the signal frequency was swept in the vicinity of half of the actuator's resonant frequency $f = \frac{1}{2} f_m$ as described in section 3.2 using the experimental setup of Figure 3.12. The signal amplitude was set to $V_{\text{AC}} = 10$V and was amplified using the resonant matching technique with a $L = 675$ μH inductor connected in series with the actuator. The beam tip velocity was recorded using the LDV over a time window of 4 ms. The frequency-response curves shown in Figure 4.10 were obtained using four slew rates, 750 kHz/s, 625 kHz/s, 375 kHz/s, and 300 kHz/s, by post-processing the measured displacement to evaluate its RMS over a moving time window extending over 70 excitation periods.

In all four cases, the actuator exhibits transients in its response even at the lowest slew rate covering the smallest frequency range $f = [780.2 - 781.4]$ kHz. Evidence of those transients can be seen in the fluctuations observed at the outset (low end) of the up-sweeps as well as in the shift of the frequency-response curve to lower frequencies. Another evidence of the non-stationarity of those curves can be found in the variation of their peak values. This behavior can be contrasted against the stationary frequency response of Actuator I shown in Figure 3.13(b), which has a similar quality factor $(Q_m = 1211)$ but was captured using a digital oscilloscope in a much longer (4s) time window. Note that the smaller tip velocity of actuator III is due to mistuning between the electrical resonance $f_e$ and the mechanical resonance $f_m$.

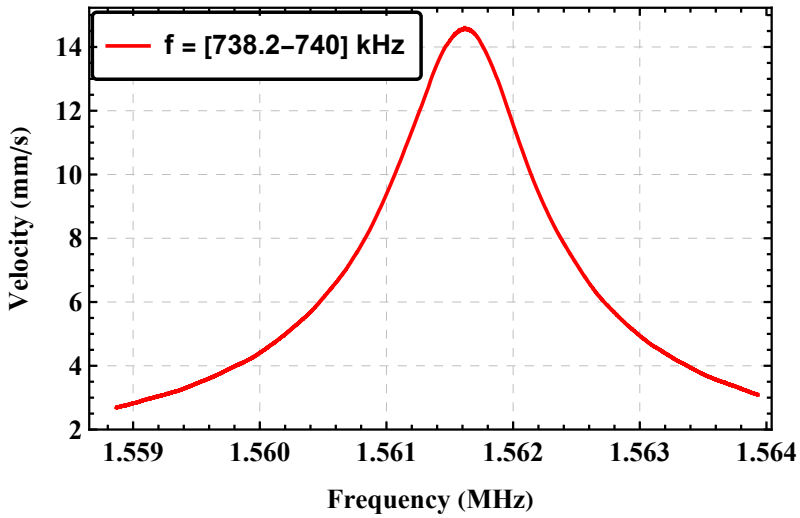



Figure 4.11: The stationary frequency-response curve of actuator III obtained using the stitching technique.

An alternative technique to obtain stationary frequency-response curves directly from the LDV, without recourse to the longer buffer of the digital oscilloscope, is to divide the overall time window into smaller sub-windows. For instance, to obtain the stationary frequency response of actuator III shown in Figure 4.11 under same signal and resonance matching circuit, the frequency sweep over the range $f = [738.2 - 740]$ kHz was performed over a total time win-

dow of 130 ms at a slew rate of 20 kHz/s. Partial frequency responses were obtained each 5 ms sub-window, which were then ‘stitched’ together to construct the overall frequency-response curve over the entire 130 ms time window.

# Chapter 5

# Conclusions and Future Work

## 5.1 Conclusions

The relative merits of three resonant drive methods have been investigated and compared with a view to reducing the high voltage requirements of electrostatic MEMS actuators. The three methods were compared with actuation using a function generator and voltage amplifier as a ground truth measure. Furthermore, a coupled electromechanical model was introduced to interpret the response of the actuator in conjunction with the resonant drive circuit.

We found that resonant circuits are more effective at amplifying the MEMS response than voltage amplifiers in the high frequency ($> 1$ MHz). In lower frequencies, voltage amplifiers are more flexible and stable whereas resonant circuits suffered larger losses due to the loss tangent of the associated parastic capacitance. Moreover, we found that mixed frequency and amplitude modulation techniques are more flexible and easier to adjust compared to resonance matching. However, resonance matching is more effective for unbiased (AC) excitation as it results in higher voltage amplification (proportional to $Q_e^2$) than the other two techniques as well as resonant

matching with biased signals where voltage amplification was only proportional to $Q_e$. We also conclude that using biased signals with any of the resonant drive techniques is ineffective for the purposes of amplification. While it can be used to tune the MEMS nonlinearity, it should be noted that it may also increase the dielectric charging.

The inefficiency of resonant circuits in low frequencies meant that actuation using the additive version of the multi-frequency excitation technique $(f_1 + f_2)$ proved ineffective in the case of the actuator under study. However, this version of the multi-frequency excitation technique should be practical for higher frequency actuators. For example, we employed it to locate the second out-of-plane bending mode of actuator I′ shown in Figure 5.1.

While we assumed in our comparison that the amplification of the RLC circuit is constant across the entire frequency response and equal to the electrical quality factor $Q_e$, this assumption holds only when the mechanical quality factor is much larger than the electrical quality factor $(Q_m >> Q_e)$ [47]. This was true in the actuators used in this comparison but not true in general. Where the the two quality factors are of the same order, they would continue to be decoupled under multi-frequency and amplitude modulation techniques but would become impractical under resonance matching technique.

Further, we found experimentally that the electrical quality factor $Q_e$ of the resonant circuits improves with larger inductors as the ESR of the inductors is negligible compared to the circuit parasitic resistance, which leads to an overall improvement in the quality factor.

Finally, we conclude that grounding the substrate and/or the surroundings increases in the overall capacitance of the MEMS as it leads to higher parasitic capacitance. To minimize it, we recommend leaving the substrate and surroundings floating. This would lead to their capacitance appearing in series with the MEMS capacitance, thereby minimizing their impact.

## 5.2 Future Work

1. Better Model: A better understanding and a better model of actuator and its electrostatic field, specifically its fringing field, see figure 2.4, is needed.

   The model presented in this work assumed a constant resonant frequency, however, it was observed that the frequency has a linear shift at higher displacement amplitudes. This linear hardening was observed in the response of actuators I and II , as discussed in section 3.4 subsection 3.3.3. The origins of this hardening may lie in the fringing electrostatic field rather than the mechanical potential.

   Further, it was also assumed that the electrical and mechanical subsystem are decoupled, however, we saw a limited skewness in the frequency response of actuator II under amplitude modulation excitation with $f_e = 13.1$ MHz, Figure 3.46, that appears to increase progressively with excitation amplitude. This indicates both the presence of electromechanical coupling and some level of hardening nonlinearity in the system.

   The quality factors estimated using the model in the multi-frequency excitation case were over estimated compared to the VNA-measured quality factors, see section 3.5. This again indicates a model deficiency that requires a remedy.

   Finally, we observed, section 4.2, that the response of actuator II increased by a factor of 3 when the polarity was switched. We proposed a possible explanations for this behavior that induced charges on the handle layer may be causing it to act as a capacitor, resulting in increased out-of-plane fringing field and displacements. However, further investigation is needed to validate and fully understand this phenomenon.

2. Investigation of the second in-plane and out-of-plane modes: We found indications of an interaction between one or both of these modes and a resonant circuit under the additive

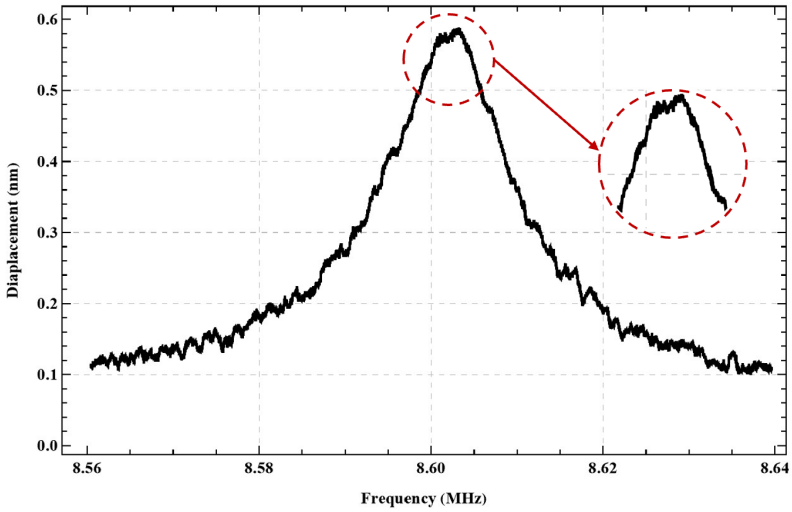



Figure 5.1: Frequency response of the second out-of-plane bending mode of actuator I′.

version of multi-frequency excitation with an external inductor $L = 130\,\mu$H, which set first signal frequency to $f_1 = f_e = 4.2$ MHz. The second signal frequency was swept across the frequency domain until the mode of interest was located when $f_2$ was in the range $f_2 = 4.36 - 4.44$ MHz. Consequently, the second out-of-plane bending mode was identified within the frequency range of $f_1 + f_2 = f_m = 8.56 - 8.64$ MHz. We observed that the frequency-response curve of actuator I′ has two peaks, suggesting the presence of two distinct modes. In Figure 3.19(b), it was shown that the electrostatic force has a frequency component present at $2f_e$. Therefore, we assume that one of the two peaks corresponds to the electrical frequency component at $2f_2 = 8.4$ MHz. Note that $2f_e$ could potentially result in resonance matching excitation as well. This requires further investigation.

3. Improved Resonant Circuit Design: The VNA-measured electrical quality factor of the RLC circuit with a 2.2 mH inductor was $Q_e = 54$. However, the model estimated quality factor for actuator I driven by this circuit was $Q_e = 18.75$. This significant drop suggests that the drive setup connecting the RLC circuit to the actuator has introduced substantial

losses. Improving the drive setup will reduce these losses and increase the realized amplification. This can be achieved by eliminating the wires and cables and replacing breadboards with a custom-designed PCBs.

4. Parasitic Capacitance Investigation: The loss tangent of the parasitic capacitors (increased losses) observed in additive multi-frequency excitation $(f_1 + f_2)$ requires further study.

   Additionally, further investigation is needed to understand the deviation the measured overall capacitance in section 4.2 when the polarity of the actuator was switched between the beam and the side electrode, while maintaining the substrate in a floating.

# Bibliography


[1] V. Kaajakari, *Practical MEMS*. Las Vegas, NV: Small Gear Publishing, 2009.

[2] M. Younis, *MEMS linear and nonlinear dynamics*. New York: Springer, 2011.

[3] J. W. Judy, "Microelectromechanical systems (MEMS): fabrication, design and applications," *Smart materials and Structures*, vol. 10, no. 6, p. 1115, 2001.

[4] P. F. Partnership, "An introduction to MEMS (Micro-electromechanical systems)," 2002.

[5] M. Gad-el-Hak, *MEMS Applications*. Boca Raton, FL: CRC Press, 2006.

[6] E. Pengwang, K. Rabenorosoa, M. Rakotondrabe, and N. Andreff, "Scanning Micromirror Platform Based on MEMS Technology for Medical Application," *Micromachines*, vol. 7, no. 2, p. 24, 2016.

[7] J. Pandiyan, S. Balachandar, S. Ramaswamy, M.Arumugam, and M.Umapathy, "Novel MEMS Electrothermal Actuators & Its Application," in *2005 Annual IEEE India Conference (INDICON)*, Chennai, India, 2005, pp. 123-126.

[8] A. S. Algamili et al., "A Review of Actuation and Sensing Mechanisms in MEMS-Based Sensor Devices," *Nanoscale Research Letters*, vol. 16, no. 16, 2021.

[9] B. Sviličić, G. S. Wood, E. Mastropaolo, and R. Cheung, "Thermal- and Piezo-Tunable Flexural-Mode Resonator With Piezoelectric Actuation and Sensing," *Journal of Microelectromechanical Systems*, vol. 26, no. 3, pp. 609-615, 2017.

[10] I.-J. Cho and E. Yoon, "A low-voltage three-axis electromagnetically actuated micromirror for fine alignment among optical devices," *Journal of Micromechanics and Microengineering*, vol. 19, no. 8, p. 085007, 2009.

[11] Y.Q. Fu, J.K. Luo, A.J. Flewitt, and W.I. Milne, "Smart microgrippers for bioMEMS applications," in *MEMS for Biomedical Applications*, S. Bhansali and A. Vasudev, Eds. Cambridge: Woodhead, 2012, ch. 11, p. 300.

[12] P. Zhang, "Sensors and Actuators," in *Advanced Industrial Control Technology*, 2010, ch. 3, pp. 112-113.

[13] J. Na, Q. Chen, X.i Ren, "Hysteresis Dynamics and Modeling," in *Adaptive Identification and Control of Uncertain Systems with Nonsmooth Dynamics*, 2018, ch. 16, p. 254.

[14] Z. Dong, L. Xu, and T. Yang,"Transient Response Characteristics Analysis of High-Power Piezoelectric Transducers," *Micromachines*, vol. 13, no. 10, p. 1638, 2022.

[15] W. Zhu, X.-T. Rui, "Hysteresis modeling and displacement control of piezoelectric actuators with the frequency-dependent behavior using a generalized Bouc–Wen model," *Precision Engineering*, vol. 43, pp. 299-307, 2016.

[16] W.-C. Chuang , H.-L. Lee, P.-Z. Chang, and Y.-C. Hu, "Review on the Modeling of Electrostatic MEMS," *Sensors*, vol. 10, no. 6, pp. 6149-6171, 2010.

[17] J. F. Rhoads, S. W. Shaw, and K. L. Turner, "Nonlinear Dynamics and Its Applications in Micro- and Nanoresonators," *Journal of Dynamic Systems, Measurement, and Control*, vol. 132, no. 3, p. 034001, 2010.

[18] Z. Yie, M. A. Zielke, C. B. Burgner, and K. L. Turner, "Comparison of parametric and linear mass detection in the presence of detection noise," *Journal of Micromechanics and Microengineering*, vol. 21, p. 025027, 2011.

[19] S. Krylov, B. R. Ilic, D. Schreiber, S. Seretensky, and H. Craighead, "The pull-in behavior of electrostatically actuated bistable microstructures," *Journal of Micromechanics and Microengineering*, vol. 18, p. 055026, 2008.

[20] W.-M. Zhang, G. Meng, and D. Chen, "Stability, Nonlinearity and Reliability of Electrostatically Actuated MEMS Devices," *Sensors*, vol. 7, no. 5, pp. 760–796, 2007.

[21] W.-M. Zhang, H. Yan, Z.-K. Peng, and G. Meng, 'Electrostatic pull-in instability in MEMS/NEMS: A review," *Sensors and Actuators A: Physical*, vol. 214, pp. 187–218, 2014.

[22] M. S. Al-Ghamdi, M. E. Khater, K. M. E. Stewart, A. Alneamy, E. M. Abdel-Rahman, and A. Penlidis, "Dynamic bifurcation MEMS gas sensors," *Journal of Micromechanics and Microengineering*, vol. 29, p. 015005, 2018.

[23] A. Kamel, S. Kocer, T. Das, L. Mukhangaliyeva, R. Saritas, P. Hajireza, M. Yavuz, and Eihab Abdel-Rahman, "Demonstration of Resonant Adaptive Mirror," in *2021 21st International Conference on Solid-State Sensors, Actuators and Microsystems (Transducers)*, Orlando, FL, 2021, pp. 1096-1099.

[24] A. M. Alneamy, M. E. Khater, A. K. Abdel-Aziz,, G. R. Heppler, and E. M. Abdel-Rahman, "Electrostatic arch micro-tweezers," *International Journal of Non-Linear Mechanics*, vol. 118, p. 103298, 2020.

[25] R. Sattler, F. Plötz, G. Fattinger , and G. Wachutka, "Modeling of an electrostatic torsional actuator: demonstrated with an RF MEMS switch," *Sensors and Actuators A: Physical*, vol. 97, pp. 337-346, 2002.

[26] Tabor Electronics Ltd., "40Vp-p Differential / Dual Channel Signal Amplifier," Model 9250 datasheet [Online]. Available: `www.taborelec.com/9250#Features`

[27] Falco Systems, "High speed high voltage amplifier," WMA-300 datasheet [Online]. Available: `www.falco-systems.com/High_voltage_amplifier_WMA-300.html`

[28] Acquitek, "4-quadrant voltage amplifier," A1230-01 datasheet [Online]. Available: `www.acquitek.com/product/a1230-02/`

[29] N. Jaber, A. Ramini, A. A. A. Carreno, and M. I. Younis, "Higher order modes excitation of electrostatically actuated clamped–clamped microbeam experimental and analytical investigation," *Journal of Micromechanics and Microengineering*, vol. 26, p. 025008, 2016.

[30] A. H. Nayfeh and M. I. Younis, "Dynamics of MEMS resonators under superharmonic and subharmonic excitations," *Journal of Micromechanics and Microengineering*, vol. 15, p. 1840, 2005.

[31] B. Cagdaser and B. E. Boser, "Resonant drive for stabilizing parallel-plate actuators beyond the pull-in point," in *The 13th International Conference on Solid-State Sensors, Actuators and Microsystems*, Seoul, Korea, 2005, pp. 688-692.

[32] M.H. Hasan, F.M. Alsaleem, N. Jaber, M.A.A. Hafiz and M.I. Younis, "Simultaneous electrical and mechanical resonance drive for large signal amplification of micro resonators," *AIP Advances*, vol. 8, no. 1, p. 015312, 2018.

[33] N. Jaber, M.A.A. Hafiz, S.N.R. Kazmi, M.H. Hasan, F. Alsaleem, S. Ilyas and M.I. Younis, ”Efficient Excitation of Micro/Nano Resonators and Their Higher Order Modes,” *Sci. Rep.*, vol. 9, no. 1, 2019.

[34] H.M. Ouakad, M.H. Hasan, N.R. Jaber, M.A.A. Hafiz, F. Alsaleem and M. Younis, ”On the double resonance activation of electrostatically actuated microbeam based resonators,” *Int. J. Non-Linear Mech.*, vol. 121, p. 103437, 2020.

[35] S.R. Chung, S. Park, E. M. Abdel-Rahman, J. T. Yeow and M. Khater, ”Architecture for MEMS-based analogue demodulation,”*Journal of Micromechanics and Microengineering*, vol. 23, p. 045013, 2013.

[36] A. Cowen, G. Hames, K. Glukh, and B. Hardy , *“PiezoMUMPs™ Design Handbook,”* MEMSCAP Inc., 2014.

[37] P. N. Kambali and A. K. Pandey, “Capacitance and Force Computation Due to Direct and Fringing Effects in MEMS/NEMS Arrays,” *IEEE Sensors Journal*, vol. 16, no. 2, pp. 375-382, 2016.

[38] W. D. Pilkey, *Formulas for stress, strain, and structural matrices*.John Wiley & Sons, Inc, 2004.

[39] Polytec Inc., “Ultra High Frequency Vibrometer,” UHF-120 datasheet [Online]. Available: `www.polytec.com`

[40] Liquid Instruments, “The Ultimate Test and Measurement Solution,” Moku:Pro datasheet [Online]. Available: `www.liquidinstruments.com`

[41] Tabor Electronics Ltd., “400Vp-p Four Channel Signal Amplifier,” Model 9400 datasheet [Online]. Available: `www.taborelec.com/9400`

[42] Polytec Inc., “Polytec Scanning Vibrometer,” Software Manual.

[43] Polytec Inc., “OFV-5000 Vibrometer Controller,” User Manual [Online]. Available: www.polytec.com

[44] M. Ou, Y. S. Shama, B. Mavani, M. Arabi, R. Saritas, R. Abdelrahman, S. Rahmanian, A. Elhady, R. Mansour, A. Penlidis, and E. M. Abdel-Rahman, “Static and Dynamic MEMS Inertial Gas Sensors,‘‘ accepted, *Transducers 2023*, Kyoto, Japan, June 2023.

[45] S. Park, M. Khater, D. Effa, E. Abdel-Rahman, and M.Yavuz, “Detection of cyclic-fold bifurcation in electrostatic MEMS transducers by motion-induced current,” *Journal of Micromechanics and Microengineering*, vol. 27, p. 085007, 2017.

[46] L. L. Li, E. L. Holthoff, L. A. Shaw, C. B. Burgner, and K. L. Turner “Noise Squeezing Controlled Parametric Bifurcation Tracking of MIP-Coated Microbeam MEMS Sensor for TNT Explosive Gas Sensing,” *Journal of Micromechanics and Microengineering*, vol. 23, no. 5, October, 2014.

[47] P. A. Truitt, J. B. Hertzberg, C. C. Huang, K. L. Ekinci, and K. C. Schwab, “Efficient and Sensitive Capacitive Readout of Nanomechanical Resonator Arrays,” *Nano Lett.*, vol. 7, pp. 120-126, 2007.